X-ray spectra of the accreting neutron star 4U 1907+09

Zulassungsarbeit
vorgelegt von
Stefanie Roth

Dr. Karl Remeis-Sternwarte
Astronomisches Institut
der Friedrich-Alexander-Universität
Erlangen-Nürnberg
2008

Erweiterte deutsch Zusammenfassung

Roth, Stefanie

Röntgenspektren des akkretierenden Neutronensterns 4U 1907+09

Die Faszination mit akkretierenden Röntgen Pulsaren hat über die Jahre seit ihrer Entdeckung (Giacconi et al., 1971) nicht abgenommen. Astrophysiker sind heute in der Lage, vieles zu beschreiben was in diesen akkretierenden Neutronensternen passiert, aber es gibt immer noch Dinge die nicht verstanden oder unzureichend erklärt sind. Akkretierende Röntgen Pulsare sind Doppelsterne die im Röntgenbereich emittieren. Diese Doppelsterne bestehen aus einem kompakten Objekt wie z.B. einem Neutronenstern und der andere ist oft ein Hauptreihenstern. Neutronensterne haben bemerkenswerte Eigenschaften wie ihre sehr hohen Dichten und ihre großen Magnetfelder trotz ihrer Größe von nur 10km Radius. Ihre Magnetfelder sind bis zu eine Million mal strker als alles was jemals auf der Erde produziert oder gemessen wurde (Bickenkov, 2006). Das vom Begleiter akkretierte Material koppelt an die Magnetfeldlinien des Neutronensterns und folgt ihnen auf die magnetischen Pole. Die zwei so genannten "hot spots" die an den magnetischen Polen entstehen sind von großem Interesse für viele Studien, da ihre exakte Geometrie noch nicht bestimmt ist. Eine möglicher Verkippung der magnetischen und der Rotationsachse kann Pulsationen entstehen lassen. Perioden von Pulsaren, schnell rotierenden Neutronensternen die Pulsationen zeigen, reichen von Millisekunden bis Sekunden.

Die Röntgenastronomie ist ein faszinierendes Feld für die Forschung, aber bringt auch viele Herausforderungen mit sich. Gute theoretische Schätzungen des Magnetfelds von Neutronensternen waren bereits für einige Zeit bekannt, aber erst in den späten 1970er Jahren waren Trümper et al. (1978) in der Lage den Beweis zu liefern. Sie beobachteten eine Zyklotronresonanzlinie (CRSF) in dem Spektrum von Hercules X-1. Zyklotronresonanzlinien werden als Absorptionslinien in den Spektren von hoch magnetisierten akkretierenden Neutronensternen in Doppelsternsystemen beobachtet (Heindl et al., 2004) und entstehen durch die Quantisierung der Bewegungsenergie der Elektronen in starken Magnetfeldern. Die Energie unter der eine CRSF beobachtet wird steht in direkter Beziehung zu der Magnetfeldstärke durch die 12-B-12 Regel, d.h. die Energie der Zyklotronlinie ist proportional zum Magnetfeld des Neutronensterns. Bis heute sind Untersuchungen der Zyklotronresonanzlinien die einzig direkte Methode, um das Magnetfeld von Neutronensternen zu messen.

In dieser Arbeit werden mit dem Satelliten Suzaku gemachte Beobachtungen des akkretierenden Neutronensterns 4U 1907+09 beschreiben. Suzaku ist Japans fünfter Röntgensatellit und wurde gemeinschaftlich mit der USA entwickelt. Um die Daten für diese Arbeit zu liefern, beobachtete Suzaku die Quelle 4U 1907+09 einmal im Jahr 2006 und ein zweites mal in 2007. 4U 1907+09 ist ein Windakkretierender Neutronenstern mit einem Begleiter mit großer Masse. Windakkredition ist nur eine von drei Möglichkeiten die genauer in Kapitel 3.2 beschrieben werden. Im letzten Kapitel der Arbeit werde ich die Ergebnisse präsentieren, die ich aus den beiden Beobachtungen gewonnen habe. Von Daten die andere Satelliten aufgenommen haben, ist es bekannt, dass die Lichtkurven

von 4U 1907+09 sowohl Abschwächung als auch Aufflackern zeigen. Kapitel 6.5 zeigt die phasengemittelten Spektren die simultan von 1–40keV modelliert wurden, dabei wurde für die Zyklotronenresonanzlinie ein Linienprofil benutzt, für das eine gaussförmige optische Tiefe angenommen wird. Die Energie der Zyklotronresonanzlinie von 4U 1907+09 war im Jahr 2006 $E_{\rm cyc} = 17.52$, was einer Magnetfeldstärke von $B = 1.52 \times 10^{12}\,{\rm G}$ enspricht. Im Jahr 2007 war die Energie höher und lag bei $E_{\rm cyc} = 20.28$ und damit war die Magnetfeldstärke $B = 1.75 \times 10^{12}\,{\rm G}$. In einem zweiten Modellansatz wurde dann ein einheitliches Modell für die Zyklotronlinienfrom, das auf Monte Carlo Simulationen (Schönherr et al., 2007) basiert, angenommen. Die mit diesem Modell bestimmten Magnetfeldstärken lagen höher, nämlich bei $B = 2.07 \times 10^{12}\,{\rm G}$ und $2.13 \times 10^{12}\,{\rm G}$ für die Daten aus 2006 und 2007. Es wird diskutiert wie sich die Pulsperiode in den letzten 30 Jahren entwickelt hat. Bis Anfang des Jahres 2004 wurde berichtet, dass die Pulse Periode kontinuierlich immer länger wird, von Daten aufgenommen mit dem Satellit INTEGRAL in den Jahren 2004 und 2005 fanden Fritz et al. (2006) dass die Quelle wieder kürzere Puls Perioden hat und mit $\dot{P}_{\rm pulse} = -0.158\,{\rm s\,yr^{-1}}$ schneller wird. Viele Neutronensterne die Zyklotronresonanzlinien zeigen haben eine Phasenabhängigkeit der Linienparameter, was ein Effekt des Blickwinkels auf das hohe Magnetfeld ist und der Geometrie der Akkreditionssäule. Deshalb haben wir die Spektren der 2007 Daten auch phasenaufgelöst modeliert um zu sehen, welchen Einfluss die Phase auf die Spektren und seine Eigenschaften hat. Die Zyklotronresonanzlinienenergie variiert über die sechs verschiedenen gewählten Bereiche der Phase von einem Minimum von $E_{\rm cyc} = 18.7\,{\rm keV}$ bis zu $E_{\rm cyc} = 21.9{\rm keV}$ und scheint correliert zu sein mit der Phase. Die Energie des "10keV feature" variiert auch, ist aber nicht correliert mit der Energie der Zyklotronlinie.

Abstract

Roth, Stefanie

X-ray spectra of the accreting neutron star 4U 1907+09

Since the first detection of accreting X-ray pulsars (Giacconi et al., 1971) the fascination never diminished over the years. Astrophysicists are now able to describe a lot of things that are happening in these accreting neutron stars, but there are still many things not understood or sufficiently explained. Accreting X-ray pulsars are binary systems emitting in the X-ray waveband. These binaries consist of a compact object like a neutron star for example and the other one is often a main sequence star. Neutron stars have remarkable properties such as their very high densities and their great magnetic fields despite their size of only 10 km of radius. Their magnetic fields are up to 1 million times stronger than anything ever produced or measured on earth (Bickenkov, 2006). Accreted matter couples to the magnetic field lines and follows them onto the magnetic poles. The two so called hot spots that arise at the magnetic poles are of high interest to a lot of studies as their exact geometry is still not determined. A possible misalignment of the magnetic and the rotational axis can give rise to pulsations. Periods of pulsars, fast rotating neutron stars that show pulsations, range from milliseconds to seconds.
X-ray astronomy is a fascinating field for research, but also one that holds many challenges. Good theoretical estimates of the magnetic field of neutron stars were already known for quite some time, but only in the 1970s Trümper et al. (1978) were able to give proof. They observed a cyclotron resonance scattering feature (CRSF) in the spectra of Hercules X-1. Cyclotron lines are observed as absorption lines in the spectra of highly magnetized accreting neutron stars in binary systems (Heindl et al., 2004). The energy at which a CRSF is observed is directly related to the magnetic field strength via the 12-B-12 rule, which means that the energy of the cyclotron line is proportional to the magnetic field strength of the neutron star. Until now studying cyclotron resonance scattering features is the only direct way to measure the magnetic field of neutron stars. This thesis will describe observations of the accreting neutron star 4U 1907+09 made with Suzaku. Suzaku is Japan's fifth X-ray satellite and was developed jointly with the US. Providing the data for this thesis, Suzaku observed 4U 1907+09 once in 2006 and a second time in 2007. 4U 1907+09 is a wind accreting high mass X-ray binary with a highly reddened supergiant companion. Wind accretion is only one possibility of three different accretion mechanism which will be explained in more detail in chapter 3.2. In the last part of the work the results that were gained from the two observations will be presented. From data taken with other satellites it is known that the light curves of 4U 1907+09 show dipping as well as flaring behavior. Section 6.5 shows the phase averaged spectra that were modeled simultaneously from 1-40 keV, using for the cyclotron resonance scattering feature a line profile for which a Gaussian optical depth was assumed. The energy of the cyclotron line of 4U 1907+09 was in the year 2006 $E_{\mathrm{cyc}} = 17.52$, which corresponds to a magnetic field strength of $B = 1.52 \times 10^{12}$G. In the year 2007, the energy was higher at $E_{\mathrm{cyc}} = 20.28$ and therefore the magnetic field strength was $B = 1.75 \times 10^{12}$ G. In a second approach the line was modeled

with a first self-consistent model based on Monte Carlo simulations (Schönherr et al., 2007). The magnetic field strengths derived with this model were higher, they were $B = 2.07 \times 10^{12}\,\mathrm{G}$ and $B = 2.13 \times 10^{12}\,\mathrm{G}$ for the years 2006 and 2007. It will be discussed how the pulse period has evolved during the last 30 years. Until the beginning of the year 2004 there were reports of a continuous spin down of the pulse period, from data taken in 2004 and 2005 with the satellite INTEGRAL Fritz et al. (2006) found the source to be spinning up again with $\dot{P}_{pulse} = -0.158\mathrm{s\,yr}^{-1}$. Many cyclotron sources show pulse phase dependence of line parameters, which is an effect of the viewing angle with respect to the high magnetic field and the geometry of the accretion column. Therefore the spectra of the 2007 observation were also modeled phase resolved to see what influence the phase has on the spectra and its features. The cyclotron line energy varies over the six chosen phase bins from a low of $E_{\mathrm{cyc}} = 18.7\,\mathrm{keV}$ up to $E_{\mathrm{cyc}} = 21.9\,\mathrm{keV}$ and seems to be correlated to the phase. The energy of the "10keV feature" varies also, but is not correlated to the energy of the cyclotron line.

Contents

List of Figures

List of Tables

Chapter 1

Introduction

1.1 X-ray astronomy

It is not the first time in history that a remarkable invention or discovery was made more or less by accident or unintentional. Wilhelm Conrad Röntgen did not try to find X-rays when he discovered them, Alexander Fleming did not search for a cure against bacterial infections when he discovered penicillin, Christopher Columbus never wanted to go to America. Just as Riccardo Giacconi tried in 1962 to observe X-rays from the moon's surface but was not able to do so because the X-ray emission was to small to be detectable. Instead he unintentionally observed them during a scan of the sky from the first found X-ray emitter outside the solar system. The sun was already known to be one, as rocket based observations of the sun were at that time already made for about 15 years, first detection in 1948 by Friedman et al. with a modified V2 rocket. This new emission source that Giacconi found was then later called Scorpius X-1, a luminous X-ray binary. X-ray astronomy was born and held many challenges for those who wanted to know more about it. One of the big problems that scientists were confronted with was the earth's atmosphere. The atmosphere is opaque for all types of electromagnetic radiation except for optical light and radio. The discovery of Scorpius X-1 was only possible because Riccardo Giacconi used a detector on board a rocket. Figure 1.1 shows graphically which frequencies are absorbed at what height above the earth's surface indicating the depth at which the initial intensity has decreased by a factor $1/e$. To observe X-rays it is therefore necessary to use a detector above the atmosphere. Since rockets had only a very limited time in space it was soon clear that a satellite had to be built to enable long term observations with a far better spatial resolution. UHURU, Swahili for "freedom", was the first satellite in 1970 to do X-ray astronomy (Giacconi et al., 1971). With each of the following new build satellites the possibilities grew, and more and more sources were revealed. Further information on past, active or upcoming missions is available at the NASA's High Energy Astrophysics Science Archive Research Center (HEASARC) [1]. As of fall 2007 about 550 000 X-ray sources were known, for a history of the discovery of them see HEASARC [2]. Suzaku is the name of the satellite that made this thesis possible by observing the X-ray binary

[1] `http://heasarc.gsfc.nasa.gov/docs/observatories.html`

[2] `http://heasarc.gsfc.nasa.gov/docs/heasarc/headates/how_many_xray.html`

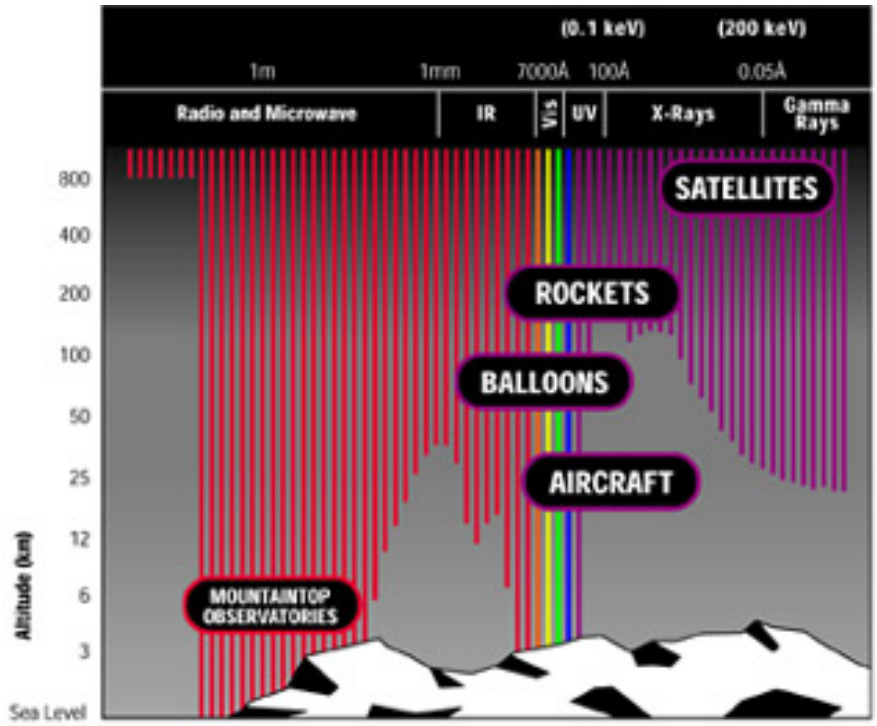

Figure 1.1: Absorption by the earth's atmosphere for different energy bands. (Image courtesy NASA: `http://chandra.harvard.edu/xray_astro/absorption.html`)

4U 1907+09 once in the year 2006 and a second time in 2007. Even though a lot of things are understood now, about 45 years after the first discovery, there are still questions with no answers and answers that don't fit any question.

1.2 Thesis outline

The purpose of this thesis is to analyze two observations of the X-ray spectra of the accreting neutron star 4U 1907+09. Chapter 2 is dedicated to X-ray binaries, giving an overview of the formation of compact objects and the evolution of binary systems. In chapter 3 the properties and characteristics of accreting X-ray pulsars will be explained, starting with X-ray binaries in general. Further this chapter will describe the accretion mechanism and the different types of accretion that are possible. The next chapter involves a discussion on the geometry of the accretion column where the continuum formation takes place and where the cyclotron resonance scattering features are formed. It also includes the theoretical discussion of the Monte Carlo Simulations that were used in the analysis to model the cyclotron lines. The 5th chapter is dedicated to the satellite Suzaku, its instruments, and the technical aspects of the observation. Chapter 6 will then introduce the focus of this paper, first a general overview over the neutron star 4U 1907+09, the data analysis and data reduction. Second the light curves, pulse periods and the fitted phase averaged and phase resolved spectra of the two observations, one in the year 2006 and the other one in 2007 are shown. The conclusion is given in the last chapter.

Chapter 2

X-ray Binaries

2.1 Compact Objects

A review of the birth and live of stars was already given numerous of times, as a thorough discussion of the stellar evolution is out of the scope of this work the focus will be led on the end of stellar evolution. For a detailed description of the evolution of stars see Unsöld & Baschek (2005) or Karttunen (1987). After a life of $10 \ldots 1000 \times 10^6$ years, stars end their lifes depending on their initial mass as one of three different compact objects. They can either evolve into a white dwarf, a neutron star, or a black hole (Pinkau, 1975). Since this thesis is about the neutron star 4U 1907+09, white dwarfs and black holes will only be discussed shortly.
The end of a stars life begins when the star has burned all of its nuclear fuel. That means for a star with a mass $M < 1.5M_{\odot}$, where $M_{\odot}$ refers to the mass of our sun, as soon as the Helium that powers the nuclear burning is almost used up. Stars are always in an equilibrium between radiation pressure and gravitational pressure. With no fuel the core burning stops, unable to produce radiation to balance the gravitational pressure of the star there is only one possibility: The core starts to collapse. At the end a white dwarf has formed (Iben, 1991). White dwarfs have densities of $\rho \approx 10^5 \ldots 10^6 \mathrm{gcm}^{-3}$. At this density the gravitational and the pressure from degenerated electrons are in equilibrium, preventing the core from collapsing further. Their radius is almost as big as the radius of our earth and their masses are always $M \leq 1.4M_{\odot}$, because of the Chandrasekhar-limit (Chandrasekhar, 1931). If the mass would exceed this limit the pressure from degenerated electrons would not be able to balance the gravitational pressure. Gravity will force the star to collapse further until a different force stops the collapse. Which force this is will be explained when described how a neutron star forms. With temperatures of $T = 10000K$ the dwarfs appear for us white, hinting at the origin of their name. The luminosity of such a white dwarf can be calculated assuming it radiates like a black body:

$$L = 4\pi R^2 \sigma_{SB} T^4 \tag{2.1}$$

where

$$\sigma_{\mathrm{SB}} = 5{,}67 \times 10^{-5} \mathrm{erg\,cm^{-2}\,K^{-4}\,s^{-1}}$$

For a white dwarf with a representative radius of $R \approx 6000km$ and a temperature of $T = 10000K$, their luminosity is $L = 2{,}6 \times 10^{30}\mathrm{erg\,s^{-1}} \approx 6{,}6 \times 10^{-4} L_\odot$. This means they are only observable out to $\approx$ 700pc with today's instruments.
Stars with larger masses end their lifes differently (Heger et al., 2003). The nuclear burning does not stop when the Helium is exhausted, other processes are ignited (Burbidge et al., 1957). But as everything also the possibilities to start new fusion finds an end. Silicium burning is the last, to burn the hereby produced iron energy would be required. Now the same thing happens as for a star with a mass smaller than $1{,}5M_\odot$. The fuel burning stops, and the star collapses. Because of the resulting temperature increase, all fuel in the outer shells ignites and the star explodes as a supernova. The remaining core collapses and depending on its mass forms a neutron star or a black whole. If the mass is lower than the Oppenheimer-Volkoff limit of $M \leq 3.2M_\odot$ the star becomes a neutron star, if it is higher a black whole. Oppenheimer & Volkoff (1939) were the first to suggest that the mass of a stable neutron star is the one for which the sound of speed is equal to the speed of light. The calculation of an accurate maximum neutron star mass strongly depends on the current knowledge of the equation of state of neutron matter up to it's very high densities. The equation of state means the relations between the density and temperature of the material on the one hand and its pressure and internal energy and specific heats on the other hand. For more details see, e.g., Galloway (2008).
Neutron stars have their name because their density of $\rho \approx 10^{13} \ldots 10^{16}\mathrm{g\,cm^{-3}}$ causes the inverse β-decay where a proton and a electron inside the core form a neutron and a neutrino. The reaction equation for this process is:

$$p^+ + e^- \rightarrow n + \nu_\mathrm{e}$$

The star is in an equilibrium between the pressure from degenerated neutrons and gravity, keeping the core from collapsing further. The neutron star then consists mainly of neutrons with a radius $r \approx$ 10km, a mass of $1.4M_\odot \leq M \leq 3.2M_\odot$ and a temperature of $T \approx 10^6$K. The lower mass limit is again the Chandrasekhar limit, as explained before stars with masses below this limit form a white dwarf. Neutron stars are, after black holes the smallest and densest stars known and through conservation of angular momentum during the collapse they acquire high angular velocities. Inserting these typical values in the same equation 2.1 as before for white dwarfs, their luminosity is estimated to be $L_\mathrm{NS} \approx 7 \times 10^{28}\mathrm{erg\,s^{-1}} \approx 2 \times 10^{-5} L_\odot$. If the mass of the collapsing star is larger than the Oppenheimer-Volkoff limit, the core collapses completely and a black hole forms.Their radius is the so called Schwarzschild-Radius:

$$R_\mathrm{s} = \frac{2\,G\,m}{c^2} = 3\mathrm{km}\frac{m}{M_\odot}$$

Neutron stars were first predicted in the 1930s by the Russian physicist Lev Landau and the Swiss astrophysicist Fritz Zwicky, but it took another 37 years until the first real discovery was made. For neutron stars the magnetic flux is, just as angular momentum, one of the conserved quantities, which is the reason for the neutron star's very strong B-field of up to $B \approx 10^{12}$G. Until now there is no direct way of measuring these unbelievable high magnetic fields. To estimate them thorough studies of the cyclotron

resonance scattering features have to be made. Hereafter when referring to the cyclotron resonance scattering features the abbreviation CRSFs or cyclotron lines will be used. Section 4.3 will explain where and how these lines are formed.

2.2 Binary systems

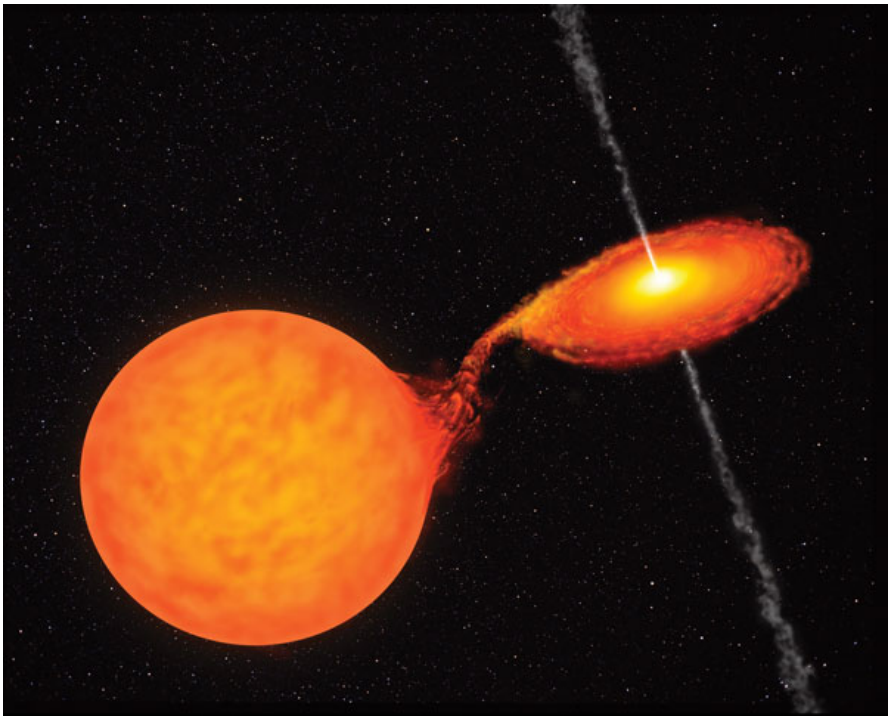

Figure 2.1: Computer illustration of an accreting X-ray binary system. (Image courtesy: nature: International weekly journal of science. `http://www.nature.com/nature/journal/v415/n6868/fig_tab/415128a_F1.html`

There are even more stars in binary systems than there are single stars (Abt, 1983). They are called binaries because its a pair of stars. These two stars move in bound orbits about their common center of mass. Often one of them is a main sequence star, and the other one is a compact object. The part X-ray in the name of X-ray binaries comes from their emission of X-rays. Their typical wavelength starts at about 12,4nm and goes to 2,48pm, these wavelengths correspond to an energy band of 0,1keV $\leq E \leq$ 500keV. X-ray pulsars have masses of $m \approx 1.4 M_{\odot}$, radii of $r \approx 10^6$cm and luminosities of $L = 10^{34} \ldots 10^{38} \mathrm{erg\,s^{-1}}$.
As mentioned above the evolution of single stars is understood quite well. The remaining question is how binaries come into existence. It is believed that the two stars have to be formed in the same interstellar gas cloud. At this point the size of the stars is too small to fill their Roche lobe. This means their forces have no influence on each other. Both follow the main steps of the evolution of single stars. But the more massive star evolves faster and leaves the main sequence and goes in the Hertzsprung-Russel diagram up into the region of blue supergiants earlier than the less massive star. The less massive

star is able to accrete material from the more massive star via the inner Lagrange-point. This happens when the more massive star expands due to it's evolution and as soon as the massive star has filled up its Roche-volume (Frank et al., 1992). For a more detailed description of accretion mechanism see chapter 3. The massive star will lose mass until he can't evolve further and becomes a helium star. When the helium and heavier elements are burned an iron core is formed, having a mass of $M \geq 1.4 M_{\odot}$. After the collapse a new binary is born while the remaining mass is expelled. The, at the start less massive star is now a massive star on the main sequence while the former massive star is now a compact object. That means the former donor star becomes the accreting star and the at the beginning accreting star is now the donor star.
In their paper "OBSERVATIONS OF ACCRETING PULSARS" Bildsten et al. (1997) give a table of known accretion-powered Pulsars as of February 1997. At that time more than 40 pulsars were known. The table includes four low-mass binaries, ten high mass binaries, twelve transient Be-binaries and eighteen systems with at that time undetermined companions. Today there are already more than 100 accreting X-ray pulsars known (Liu et al., 2005). The classification of these systems and their characteristics will be outlined in the next chapter.

Chapter 3

Accretion

Astronomy is one of the oldest professions in the world. Compared to that, though, studies of accretion mechanism are very young. Accretion processes started to gain attention in the early 1970s when X-ray binaries were discovered. Just at that time the efficiency of accretion onto compact objects was realized. Even though Zel'dovich (1964) and Salpeter (1964) suggested already in 1964 that accretion of material onto a massive star could be an important energy source. Accretion is the collection of matter onto an object under the influence of gravity. In binary systems it is the transfer of material from the main sequence star to the compact object. For a star of mass M and a radius R the gravitational potential energy release by the accretion of a mass m onto its surface is

$$\triangle E_{\mathrm{acc}} = \frac{GMm}{R}$$

Compared to the energy release from the conversion of hydrogen to helium this is about 20 times more efficient (Frank et al., 1992). 4U 1907+09 is a neutron star that accretes material from a blue super giant through wind accretion. The different kinds of accretion will be outlined in the following sections more accurately.

3.1 X-ray Binaries

The strong magnetic field of the neutron star is responsible for the coupling of matter to the magnetic field lines. At the Alfvén radius, where the magnetic field pressure equals the ram pressure the flow of material is disrupted (Basko & Sunyaev, 1976). The material follows the field lines onto the magnetic poles. During the free-fall of matter onto the poles velocities of $v \approx 0{,}65c$, where $v = (2GM)^{0.5}R^{-0.5}$ can be reached. This material is stopped on or at least very close to the surface of the neutron star, releasing all of its kinetic energy. The best way to lose energy is to radiate as a black body at temperature T. That means for neutron stars and their high temperatures of $T \approx 10^6$ K that they emit most of their energy at X-ray wavelengths. In this physical effect lies the origin of the name X-ray binaries.
X-ray binaries are very luminous objects, exceeding our sun by 10^5 times its luminosity. The reason is accretion. Sir Arthur Stanley Eddington calculated in 1920 the so called Eddington-limit, the critical luminosity at which there is equilibrium between the outgoing radiation and the gravitational pressure of the infalling gas. The

radiation pressure force is provided by Thomson scattering of the radiation by the electrons in the plasma. Assuming Thomson scattering, the smallest cross-section for the processes is adopted, which impedes the loss of radiation from the system. The gravitational force $F_g = GMm_p r^{-2}$ must be greater than the outgoing radiation force $F_{\mathrm{rad}} = \sigma_T S c^{-1}$,where the energy flux is $S = L(4\pi r^2)^{-1}$ and σ_T the Thomson cross-section equals $\sigma_T = 6.653 \times 10^{-29}\mathrm{m}^2$. Only if this is true accretion is possible, otherwise the radiation pressure blows away the infalling matter. But he had two make some assumptions to be able to get the following equation: Eddington assumed a spherically symmetric accretion of fully ionized pure hydrogen gas and derived with these approximations this equation:

$$L < L_{\mathrm{edd}} = \frac{4\pi G M m_{\mathrm{p}} c}{\sigma_{\mathrm{T}}} \approx 1{,}3 \times 10^{38} \frac{M}{M_\odot} \frac{\mathrm{erg}}{\mathrm{s}}$$

In this equation M is the mass of the accreting object and m_{p} refers to the mass of the accreted proton or electron. If the accretion only occurs over a fraction f of the surface, the corresponding limit is fL_{edd}. One might think this is the case for highly magnetized neutron stars, as they only accrete material onto the poles. But as these poles only take a very limited part of the surface of the neutron star, the energy does not necessarily have to be radiated in the direction of the infalling gas. It is possible that energy is radiated sideways without interacting with the incoming material. The Eddington-Limit is also an upper limit for the accretion rate $\dot{M}_{\mathrm{acc}}$:

$$L = \frac{GM\dot{M}_{\mathrm{acc}}}{R}$$

R is the radius of the accreting object in this equation. But this limit of luminosity only holds true for steady-state situations, it can be exceeded by a non-steady-state situation such as a supernova explosion by a large margin. Supernovas can reach absolute magnitudes of up to $m = -19.3\,\mathrm{mag}$, which is about 5 billion times brighter than our sun.

3.2 Accretion mechanism

The compact object is able to accrete matter either through Roche Lobe Overflow, from the stellar wind of the companion star, or through the Be-mechanism. For some binary systems it is also possible that more than one type of mass transfer takes place. The spin frequency gives a hint at which mechanism is observed. A persistent trend in the spin frequency indicates the presence of an accretion disk, while short term changes with no persistent trend are usually indicative of a wind-fed system (Bildsten et al., 1997). Jocelyn Bell Burnell was the first to discover pulsars in the 1967 as radio sources. With the satellite Uhuru the first detections of pulsations from neutron stars in the X-ray waveband were observed. Schreier et al. (1972) found 4.8 s pulsations from the source Centaurus X-3, identifying Cen X-3 as an X-ray pulsar. These authors additionally recognized drops in the countrate that occurred on a timescale of 2.08 days, which could be due to eclipses by a star that orbits Cen X-3. The source Hercules X-1 was also observed with UHURU and identified as a X-ray pulsar showing pulsations of 1.24 s

and drops in the countrate on a timescale of 1.7 d (Tananbaum et al., 1972). The X-ray pulsars are their own class of astronomical objects and are recognized to be highly magnetized rotating neutron stars. When these neutron stars are part of a X-ray binary that accretes from its companion they are referred to as accretion powered pulsars as opposed to rotation powered pulsars for example. The X-rays emitted from an accreting neutron star at the magnetic poles move along the magnetic axis at the speed of light. If the rotational and the magnetic axis of the rotating star are misaligned, the so called "lighthouse effect" makes it possible to observe pulsations from the source. To date observed periods of pulsars have a wide range from milliseconds to seconds.

3.2.1 Roche lobe overflow

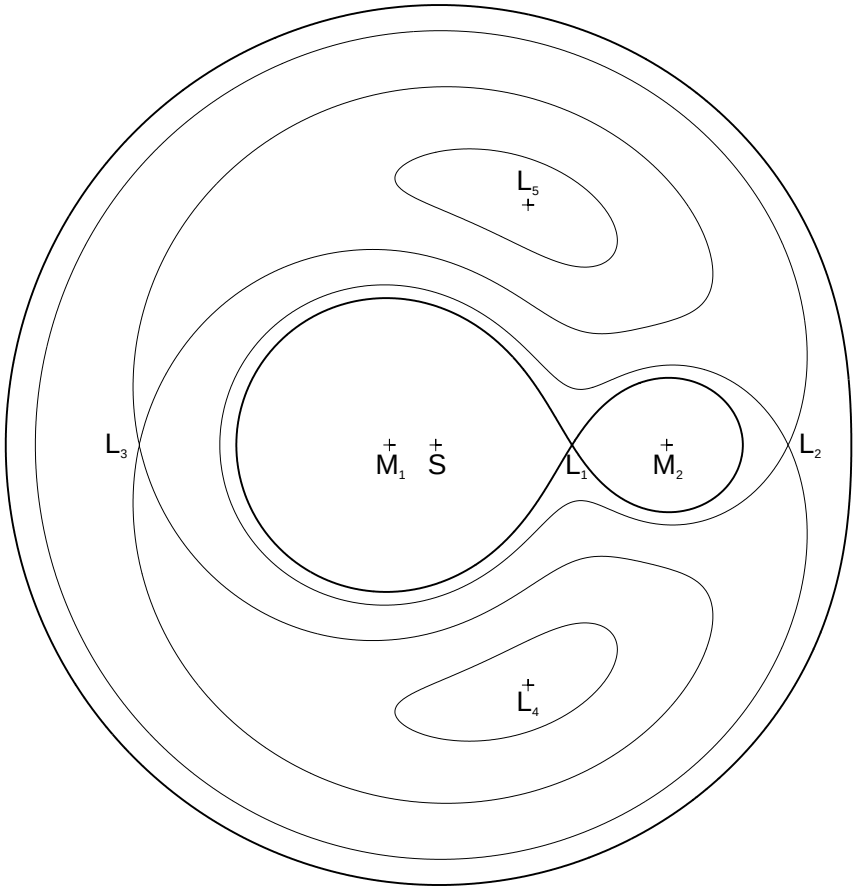

Figure 3.1: Equipotential surfaces of the Roche potential with a mass ratio $M_1 : M_2 = 5$ where M_1,M_2 are the masses of the two stars. L_1 to L_5 are the Lagrange points and S is the center of mass of the binary system. (Image courtesy Kretschmar 1996)

Roche lobe overflow is the best understood of the accretion mechanism. Explaining the evolution of binary systems section 2.2 already mentioned how this accretion mechanism works. During the evolution of stars there are certain stages in which the star expands. The star can then fill its Roche Lobe. Matter from the donor star is able to stream to the compact object through the inner Lagrange point of the effective gravi-

tational potential, the so called Roche potential. The Roche potential is named after Euard Albert Roche who first conceived this potential in 1849. The inner Lagrange point is where the lobes join, a saddle point of the potential. This transfer of material happens as it seeks a lower gravitational potential. The stream is accelerated by the gravitational attraction of the accreting star within its Roche lobe, the gas becomes supersonic (Savonije, 1978). Equation 3.1 shows the Roche potential of a binary system assuming two point masses in the corotating frame and circular orbits, which is for binaries a very good approximation (Frank et al., 1992):

$$F_{Roche}(\vec{r}) = -G\frac{M_1}{|\vec{r}-\vec{r_1}|} - G\frac{M_2}{|\vec{r}-\vec{r_2}|} - \frac{1}{2}(\vec{\Omega}\times\vec{r})^2 \tag{3.1}$$

where $M_1, M_2, \vec{r_1}$, and $\vec{r_2}$ are the masses and positions of the two stars and $\vec{\Omega} = (GM/a^3)^{1/2}\hat{e}$ is the angular velocity. The shape of the equipotential is mainly due to the mass ratio of the two stars, while the overall scale is given by the binary separation. This mechanism is only present in close binary systems, therefor also called a semi-detached system. Because of the angular momentum of the material, gained from the rotation of the donor star, the matter cannot be accreted directly. It first has to rid itself of most of its angular momentum which leads to the formation of an accretion disk. The accretion disk will be circular as the gas in the stream will tend to the orbit of lowest energy for a given angular momentum. In the formed accretion disk the material is kept before it falls onto the magnetic poles. Inside the disk matter interacts, viscous forces exert torques and angular momentum is transfered (Anzer & Börner, 1980). The material with increased angular momentum is able to leave the accretion disk at a certain point. If the angular momentum has decreased the material can move on the disk closer to the compact object, it spirals into the neutron star. Radial acceleration due to pressure is negligible compared to gravitational acceleration in the disk. The gas in the disk has very high temperatures of $T = 10^7 K$ due to friction. The best understood case for accretion disks is that of thin disks, that means that the vertical thickness is much smaller than the radius R, but that also requires that the Eddington-limit for luminosity is not reached to be able to neglect the radiation pressure. The gas pressure supports the disk vertically against gravitation.

3.2.2 Be mechanism

The second possibility to accrete matter is a form of non steady accretion. This accretion mechanism is called Be because the donor star in this case is a very rapidly rotating Be star. The evolution of this binary is the reason for the compact object's eccentric orbit around the donor star. This orbit makes it impossible for the neutron star to accrete material through Roche Lobe overflow constantly as described in Section 3.2.1 because they are not close enough. The Be star forms a decretion torus, a disk-like stellar wind at the equator, around itself. Directly at periastron, as well as shortly before and after the stars are close enough. Now the compact object is able to accrete matter from the Be star's decretion torus. During that time an accretion disk forms around the neutron star and it emits X-rays. After it has left periastron and is again too far away from the donor star, no accretion takes place. These so called outbursts happen periodically

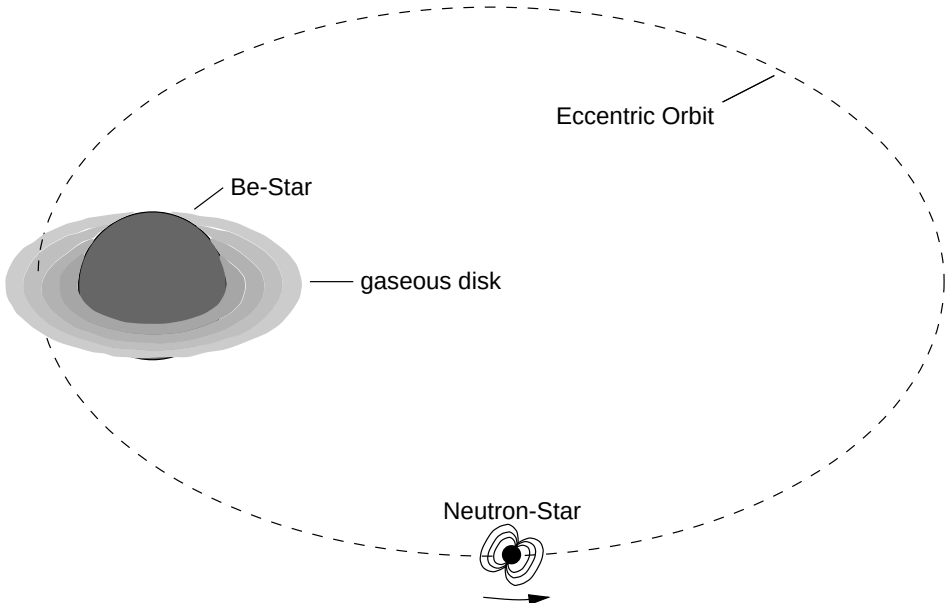

Figure 3.2: A neutron star in an eccentric orbit around a Be star. If the neutron star comes during periastron near the Be star's circumstellar disk, accretion is possible and a X-ray outburst is observed. The source is otherwise in quiescence or too dim to be detectable. (Image courtesy Kretschmar 1996)

every time the compact object is at and near to periastron. Some compact objects are so dim when they are not accreting that they can't be observed during that time. These sources are called transients.

3.2.3 Wind accretion

Just as our sun all stars emit matter in the form of quasi-spherical stellar winds, driven by radiation pressure in absorption lines. For an early type O- or B-star with mass $M \geq 10M_{\odot}$ these winds can be very strong. They are able to carry up to $10^{-10}M_{\odot}yr^{-}1 \ldots 10^{-6}M_{\odot}\,\mathrm{yr}^{-1}$ of material away from the donor star. The temperature of this wind is $T \approx 10^4 K$. Another very important value for stellar winds is their velocity. The wind velocity is approximately the escape velocity from the surface of the star (Frank et al., 1992).

$$v_{\mathrm{wind}} \approx \sqrt{\frac{2GM_{\mathrm{star}}}{R_{\mathrm{star}}}}$$

M_{star} and R_{star} are the mass and the radius of the donor star. For typical parameters the velocity is approximately a few $1000\,\mathrm{km\,s^{-1}}$, which is a lot faster than the speed of sound in the gas. If the binary separation is not too large the compact object will accrete material from this stellar wind. It will accrete from a cylindrical region with radius r_{acc}, where the gravitational pull of the neutron star overcomes the kinetic energy of the wind particles that are close enough to the neutron star (Davidson & Ostriker, 1973).

$$r_{\mathrm{acc}} \approx \frac{2GM_{\mathrm{NS}}}{v_{\mathrm{wind}}^2 + v_{\mathrm{NS}}^2 + c_{\mathrm{s}}^2} \tag{3.2}$$

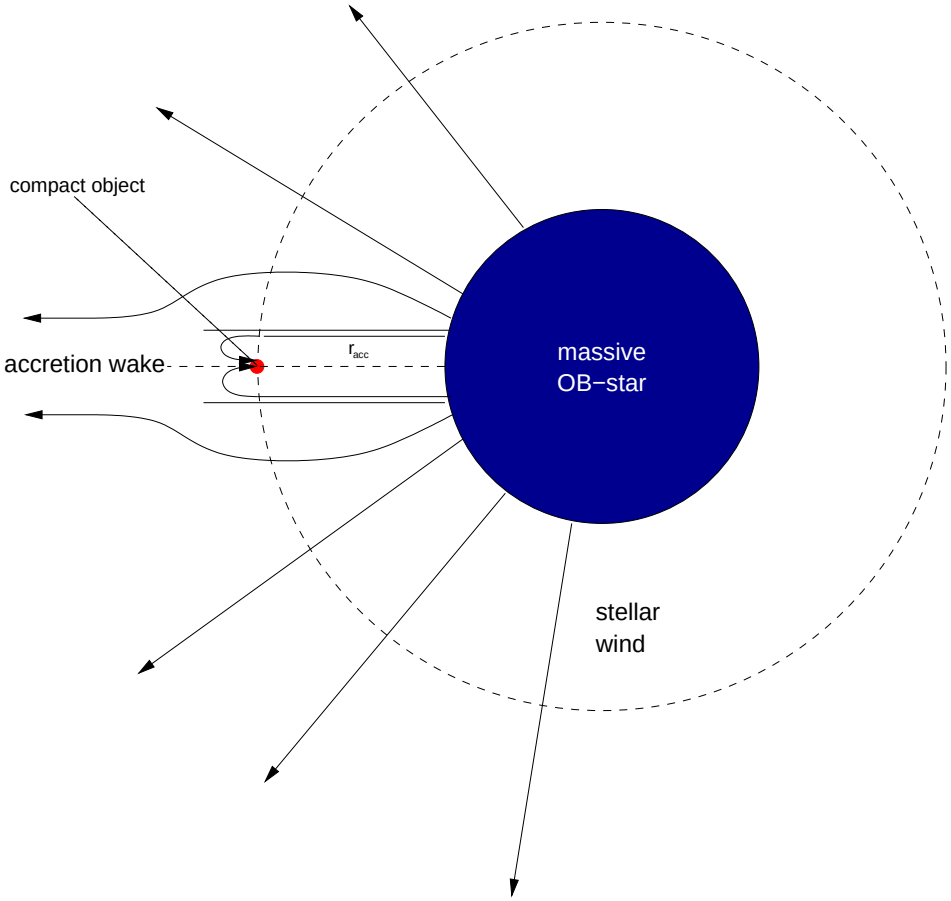

Figure 3.3: Not to scale schematic drawing of accretion from a stellar wind onto a neutron star according to Bondi & Hoyle (1944). All material within the accretion radius r_{acc} will be accreted, leaving an accretion wake behind. (Image courtesy Kreykenbohm 2004)

NS is the abbreviation for the neutron star. Usually the speed of sound through the medium, c_{s}, is neglected as it is much smaller than the speed of the wind or the neutron star's orbital velocity. Figure 3.3 shows that an accretion wake is trailing behind the X-ray source, where material is overdense. This accretion wake is due to ionization of the wind by the released X-rays and the focusing of the compact object of a significant fraction of the stellar wind. Not every particle in the stellar wind will be accreted, it is therefore of special interest how much of the actual wind can be accreted onto the compact object. Another interesting question is if it is enough matter to form an accretion disk as for the Roche lobe Overflow that was discussed above. For the next equation the velocity v_{NS} of the neutron star will be neglected, because it is much smaller than the velocity of the wind v_{wind}. The fraction f of the stellar wind that is accreted by the compact object is given by (Frank et al., 1992)

$$f \approx \frac{1}{4}\left(\frac{M_{\mathrm{NS}}}{M_{\mathrm{star}}}\right)^2\left(\frac{R_{\mathrm{star}}}{a}\right)^2$$

where a is the binary separation. For typical X-ray binaries this means accretion of $10^{-4} - 10^{-3}$ of the mass loss rate of the donating star. To estimate the net amount of gas captured equation 3.2 is combined with Kepler's third law and the continuity equation. Assumed is a spherically symmetric and steady mass loss by the donor star. The mass accretion rate is then:

$$\dot{M} = \frac{(GM)^2}{a^2(v_{\text{wind}}^2 + v_{\text{NS}}^2)^2}\dot{M}_{\text{wind}} \tag{3.3}$$

Inserting common values in this equation the Eddington-limit for the mass accretion rate is reached. For a neutron star accreting from a stellar wind the luminosity can therefor be approximated as follows with $L = (GM_{\text{NS}}f\dot{M}_{\text{wind}})/(R_{\text{star}})$:

$$L_{\text{acc}} \sim 10^{37}\left(\frac{\dot{M}}{10^{-4}\dot{M}_{\text{wind}}}\right)\left(\frac{\dot{M}_{\text{wind}}}{10^{-5}M_{\odot}\text{yr}^{-1}}\right)\text{erg s}^{-1} \tag{3.4}$$

The accreted material has always some angular momentum, because the stars move, this is why also in this case an accretion disk forms, but only a small one.

3.3 High and low mass X-ray binaries

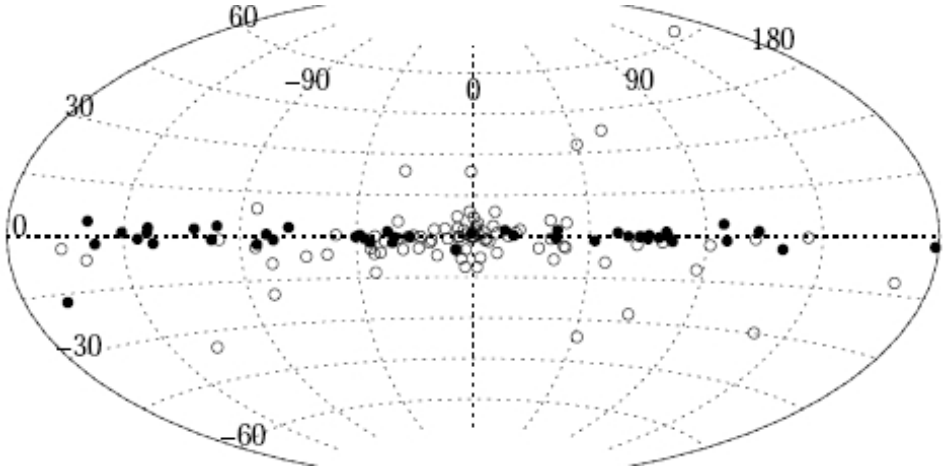

Figure 3.4: Distribution of LMXBs (open circles) and HMXBs (filled circles) in the Galaxy. In total 86 LMXBs and 52 HMXBs are shown. Note the significant concentration of HMXBs towards the Galactic Plane and the clustering of LMXBs in the Galactic Bulge. (Image courtesy Grimm et al. 2003)

.

There is an differentiation between High-Mass X-ray Binaries, which will in the following be abbreviated by HMXB and Low-Mass X-ray Binaries abbreviated with LMXB. HMXB's have a donor star that has an early spectral type O or B and a mass of $M \geq 6M_{\odot}$. As explained above these stars have strong stellar winds. The accreting star is a young neutron star with a high magnetic field of $B \approx 10^{12}G$. Their distribution in space is near the galactic plane. All three accretion mechanism, wind accretion, Roche

lobe overflow or Be accretion are possible. For most HMXBs donating matter through wind it is thought that the star is close to filling its Roche lobe (Conti, 1978). This means that the shape of the star will be extended in the general direction of the inner Lagrange point. Wind loss rates can be greater, because the wind will start further from the center and will have to overcome a smaller gravitational potential. The periods of the neutron stars of HMXBs are closely related to the observed accretion mechanism. Neutron stars that accrete via Roche-lobe Overflow have short spin periods of less than 10 seconds and short orbital periods of mostly 4 days. They have luminosities of about $L \geq 10^{37}\text{ergs}^{-1}$ and show almost steady torques on large timescales, which means longer than their orbital period. Wind-fed systems have longer orbital periods, to avoid roche-lobe overflow and are not as luminous($L \approx 10^{35} - 10^{37}\text{erg s}^{-1}$). The torques are variable on times shorter than the orbital period. Be-systems show a clear relation between the orbital period and the spin period of the neutron star. It is believed that Be-systems with longer orbital periods are further away from the companion which means lower mass accretion rates and longer periods of equilibrium (Bildsten et al., 1997). Since the discovery of Scorpius X-1 more than 100 high mass X-ray binaries have been detected (Liu et al., 2005).
The donor star of LMXBs has an late spectral type of F or later and a mass of $M < 1.2M_{\odot}$. They are also referred to as Galactic-bulge sources because they lie in the general direction of the Galactic center. These systems have lower B-fields $B \approx 10^{8}G$ and therefor for the majority no pulsations were observed. The LMXBs are classified either as Atoll-sources or Z-sources. The classification is determined through their behavior in the color-color-diagram. A X-ray color is defined as the countrate of an upper energy band divided by the countrate of a lower energy band. Atoll-sources have typical luminosities of $0.01 - 0.2L_{\text{edd}}$. The color-color-diagram looks like an island divided into the banana state with high luminosities and an island state with lower luminosities. Z-sources are LMXBs with luminosities close to the Eddington-limit. Their color-color-diagram looks like a Z with a Horizontal Branch which shows strong variability and quasi-periodic oscillations. The diagonal normal branch has much weaker variability and the flaring branch, whose spectra is mostly thermal.

Chapter 4

Accretion column

It was already mentioned several times in this thesis that neutron stars have very high magnetic fields of the order of 10^{12}G. Simplified models always assume a dipolar magnetic field, a lot of hints were given to the fact that this might be an assumption that is too simple. Until now there is no consensus of the structure of the magnetic field. Accretion is strongly influenced by the magnetic field as it is the reason for nonspherical accretion. So far it was not explained were these magnetic fields have their origin. Section 2.1 mentioned that the neutron stars consist mainly of neutrons which means that there are also other particles present except neutrons. The neutrons are the product of the inverse β-decay, if the protons and electrons are energetic enough, which most of them are inside the neutron star. But they are also able to decay again into protons and electrons. In vacuum neutrons have a half-life of approximately 15 minutes. In the very dense matter inside the star this is prohibited by the Pauli exclusion principle, only high energetic neutrons are able to decay. Gravity makes it impossible for neutrons and protons to escape from the neutron star and the electrons are kept inside by the electrostatic potential of the protons (see, e.g., Reisenegger, 2007). But neutrinos and antineutrinos are able to escape and contribute to the cooling of the star (see, e.g., Yakovlev et al., 2001). The chemical potential of the particles will balance the direct and inverse β-decay, which forces the coexistence of a small fraction of charged particles. Charged particles play an important role as they can generate electrical currents.

The two possibilities that are thought to be able to produce fields of this strength are the fossil field hypothesis, also called flux conservation, and fields generated by a dynamo process at some stage in the evolution of the progenitor star (Spruit, 2007). Flux conversation is the most popular hypothesis and states that the magnetic fields of neutron stars are remnants of the main sequence star before the core collapse. This implies that the main sequence star must have a magnetic field, which is believed to be true for all stars and in every step of their evolution. The magnetic flux of this star is given by $\Phi = BR^2\pi$. The collapsed neutron star is expected to have an increased B-field as $B \propto R^2$. Through conservation of magnetic flux it is possible to generate magnetic fields of 10^{14}G, which is for pulsars sufficient. But another type of stars, not discussed so far are magnetars. Neutron stars with magnetic fields of up to 10^{15}G, which would mean stronger than what could be achieved by magnetic flux conservation. There is still the possibility that two different mechanism produce these magnetic fields but why

would a process that produces the fields of magnetars not be able to work for pulsars as well. The magnetic fields of neutron stars and white dwarfs are both found to be larger than magnetic fields of normal stars, supporting the thought that they are due to flux conservation. This common origin hints at the magnetic field of the progenitor star before the core collapse.

The second hypothesis is the one of field generation by a dynamo process. It is thought to occur immediately after the formation of the proto-neutron star through the combination of vigorous convection and differential rotation. OB stars have a convective core and convection is inevitable due to entropy gradients, which form during the phase of rapid neutrino cooling. Holding this statement as an argument against fossil field theories, as the fluid motions would change significantly the lower moments of the field. But it is not clear that a field that was generated by a convective zone would leave a permanent field behind. These two theories are not necessarily exclusive. It is possible, that the neutron star inherits a B-field which is then amplified or modified by convection. Now it was discussed where the magnetic fields have their origin, but how do they evolve with time? Without an influence from outside these magnetic fields do not decay with time. But accretion in binary systems is able to force the star to spin down, which can lead to a lower magnetic field. Accretion also heats the neutron star which can have an influence on the conductivity and therefore the magnetic field strength. This shows again how important it is to understand the accretion mechanism. Because of this reason this chapter will discuss the geometry of the accretion column, the formation of the spectral continuum and the cyclotron resonance scattering features. For a more in depth description on the physics of strongly magnetized neutron stars see, e.g., Harding & Lai (2006).

4.1 Accretion geometry

Discussing the different accretion mechanism in chapter 3 it is now clear were the accreted material comes from. Now the actual accretion onto the surface of the neutron star will be explained giving first an overview about what happens when the matter approaches the neutron star. The strong magnetic field of the neutron star dominates the accretion near the neutron stars surface. The B-field decreases with the distance r from the surface as $B \sim \mu/r^3$, where μ is the magnetic moment, if one assumes dipole geometry. This relation shows that the magnetic field at twice the distance is already 8 times smaller, hinting at the fact that only close to the surface the magnetic field is able to dominate the accretion stream. At the Alfvén radius, where the magnetic field pressure, which is given by

$$P_{mag} = \mu^2/(8\pi r^6) \tag{4.1}$$

(Frank et al., 1992) equals the ram pressure the flow of material is disrupted.

$$\frac{\mu^2}{8\pi r^6} = (2GM)^{1/2}\dot{M}4\pi r_M^{5/2} \tag{4.2}$$

The Alfvén radius is also referred to as magnetospheric radius. Equation 4.1 for the magnetic field pressure shows clearly how strongly the pressure increases when the

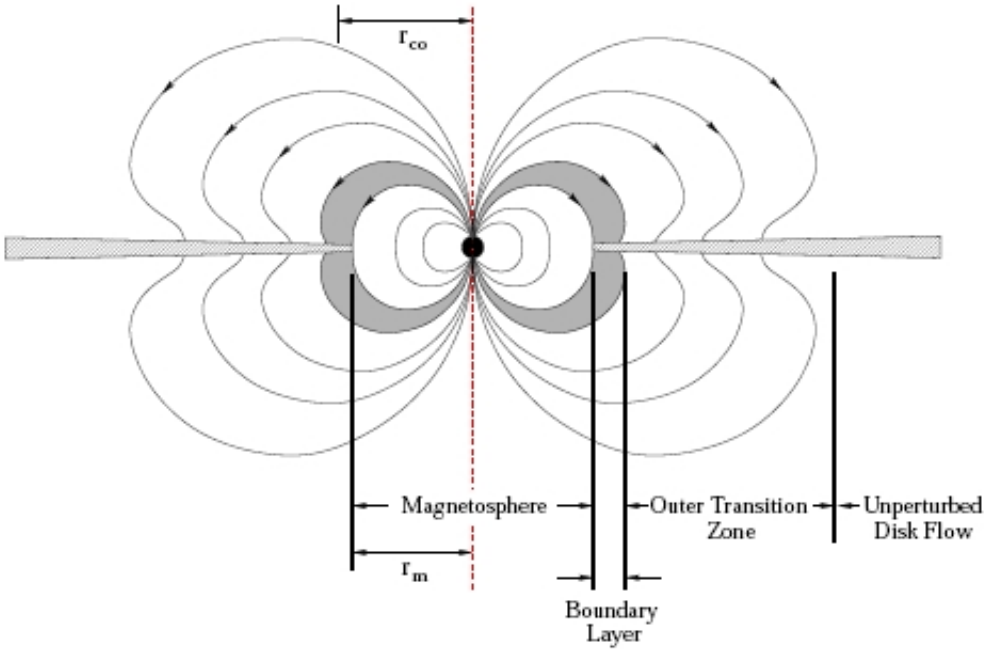

Figure 4.1: Schematic of the accretion from an accretion disk onto a strongly magnetized neutron star (Ghosh & Lamb, 1978) At the boundary layer the magnetic field is able to dominate the accretion, the material couples to the magnetic field lines. (Image courtesy Kuster 2003)

.

distance of the matter to the stars surface becomes smaller. At half the distance the pressure is 64 times stronger. For a neutron star the Alfvén radius is given by

$$r_M = 2.9 \times 10^8 M_1^{1/7} R_6^{-2/7} L_{37}^{-2/7} \mu_{30}^{4/7} \mathrm{cm} \tag{4.3}$$

After the plasma couples to the magnetic field lines, it is channeled to the magnetic polar caps, here it releases its gravitational energy as X-and Gamma-radiation. These rotating so called hot spots are the sources of the pulsed emission. The area of the accreting hot spot is for a assumed dipolar B-field:

$$\pi r_0^2 = \pi R^2 \left(\frac{R}{r_{mag}} \right) \leq 1 km^2 \tag{4.4}$$

Figure 4.2 shows on the left side a model consisting of a solid accretion column as opposed to the right side where the matter is constrained to a hollow cylinder. The walls of this cylinder are small compared to its radius. Another possibility is that the accretion column is "spaghetti like" with more than one filled pipe inside the column. Until now the details of the coupling of the accretion disk to the B-field is not really understood, which has an great influence on the geometry of the accretion column and therefore there is no consense on the internal shape of the column. In chapter 3.1 the limiting X-ray luminosity, the so called Eddington limit was discussed. One assumption that is made to receive this equation is spherical symmetric accretion. It was already

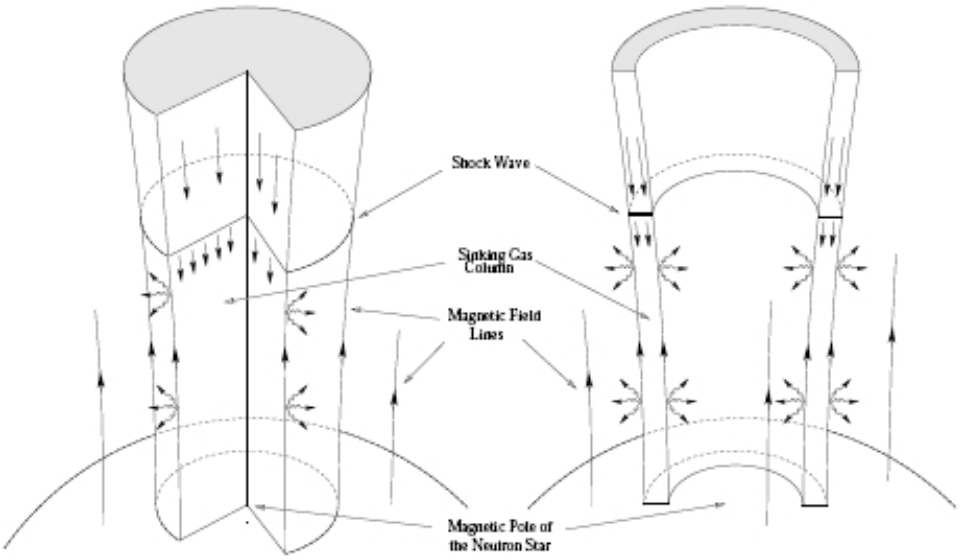

Figure 4.2: Schematic drawing of two geometries of the accretion column above the polar caps of the neutron star, as proposed by Basko & Sunyaev (1976) (Image courtesy Kuster 2003)

mentioned that the luminosity, if the star only accretes on part of the surface of the star, is smaller by the fraction of the surface on which the accretion actually occurs. This doesn't hold true anymore if the star accretes only on a very limited part of the surface. This is the case for neutron stars, as a neutron star only accretes on the magnetic poles. The energy can be emitted sideways and sideways radiated energy won't interact with the incoming matter. This makes it possible to exceed the Eddington limit for luminosity and therefore also the limiting mass accretion rate. Hence the luminosity depends on the geometry of the accretion column.

The luminosity also plays an important role as one looks closer to the neutron stars surface, where the actual accretion takes place and the matter falls onto the poles. If the accretion rate $\dot{M}$ and hence also the luminosity is above a certain limit, the radiation is emitted differently. Basko & Sunyaev (1976) were the first to calculate this critical luminosity to be:

$$L_{\text{crit}} = 2.72 \times 10^{37} \left(\frac{\sigma_T}{\sqrt{\sigma_{\parallel}\sigma_{\perp}}} \right) \left(\frac{r_0}{R} \right) \left(\frac{M}{M_{\odot}} \right) \text{ergs}^{-1} \tag{4.5}$$

In this equation r_0 corresponds to the polar cap radius, σ_T to the Thomson scattering cross section, $\sigma_{\parallel}$ and $\sigma_{\perp}$ are the cross sections for the scattering of photons which propagate parallel or perpendicular to the magnetic field direction (Becker, 1998). For accretion rates with luminosities smaller than the critical luminosity, the photons can escape without interacting with the infalling plasma. The infalling plasma falls directly at the poles where X-rays are produced by thermal bremsstrahlung and Compton cooling. This emission parallel to the B-field is shown schematically in Figure 4.3 on the right side and has the name *pencil beam* as the emission has one clear direction. If

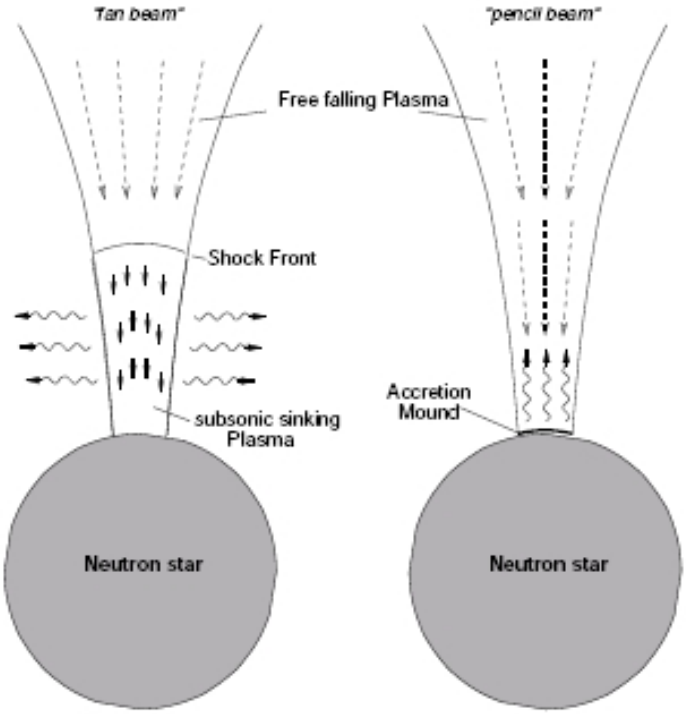

Figure 4.3: Fan beam und Pencil beam. Depending on the mas accretion rate either a shock front forms which forces the emitted photons to escape vertical to the B-field, or the matter falls directly onto the poles without interacting with the emergent photons that are emitted parallel to the B-field. (Kretschmar 1996, Dissertation AIT, Abb.2.9 after Harding (1994))

the accretion rate however is larger and the luminosities higher than L_{crit} the infalling material interacts with the emergent photons. The flow becomes super Eddington and the radiation pressure much greater than the gas pressure, hence a radiation dominated shock front develops at some distance from the neutron star surface, which does not permit the upscattered photons to escape vertically from the accretion column. The incoming plasma is decelerated and sinks to the surface of the neutron star. Figure 4.3 shows this scenario at the left side, the formed emission pattern is called *fan beam*.
Most of the photons emitted from the accretion column are produced in the dense "thermal mound" located inside the column, just above the stellar surface Becker & Wolff (2005).X-rays escape from the column as the gas decelerates through a radiative shock before settling onto the stellar surface.

4.2 Continuum Formation

Most phenomenological models that are used to fit X-ray spectra are modified power-laws with quasi-exponential cutoffs at $E \sim 20 - 30$keV (White et al., 1983). This exponential cutoff is an additional exponential factor required as the power-law alone cannot describe the steep decay of the spectra as one moves to higher energies. The

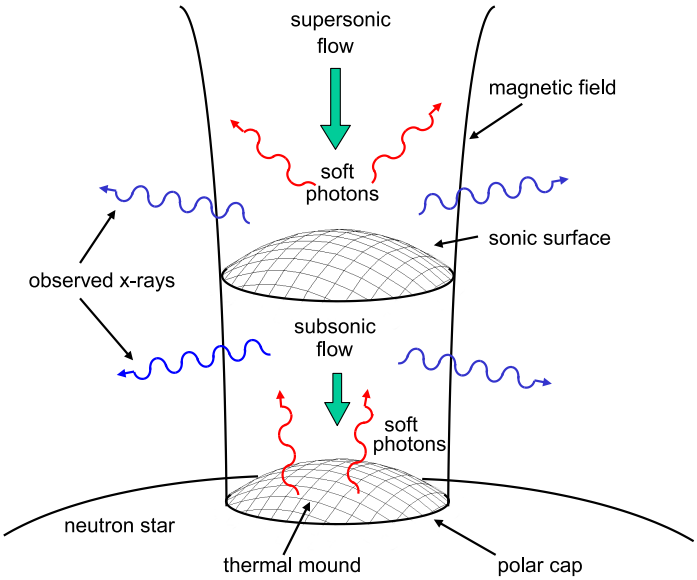

Figure 4.4: Schematic drawing of the photon production in the accretion column. (Image courtesy Becker & Wolff (2007))

corresponding model to a powerlaw with a high energy cutoff is the following:

$$C(E) = A \times E^{-\alpha} \begin{cases} 1 & \text{for } E < E_{cut} \\ \exp(\frac{E_{cut}-E}{E_{Fold}}) & \text{for } E \geq E_{cut} \end{cases} \tag{4.6}$$

The parameters that are modeled are A, the power-law normalization, α, the photon index, E_{cut}, the cutoff energy and E_{Fold}, the folding energy. This is only one example of a used model. Other examples are a powerlaw with a Fermi-Dirac cutoff or the *npex* model (Mihara et al., 1995). The model with the Fermi-Dirac cutoff would be:

$$C(E) = A \times E^{-\alpha} \left[\exp\left(\frac{E - E_{\text{cut}}}{E_{\text{Fold}}} \right) + 1 \right]^{-1} \tag{4.7}$$

Which model is used depends on the source. Some sources are best described with the high energy cutoff, as others with a different one. One has to remained oneself that these are phenomenological models and no general model could be established to date as the physics are highly complex and there is no clear understanding until now of the basic spectral formation mechanism (Coburn et al., 2002). For the case of sources with high luminosities where a shock front forms, Becker & Wolff (2007) present a new model. The authors approached the problem of understanding the continua formation from physical radiation processes and found their model to be in agreement with phase

averaged spectra from different sources. Coming now back to the other components present in an X-ray spectra. At lower energies of less than a few keV the spectrum gets absorbed by the interstellar medium. Common are also absorption features that can be due to metals, one line that is often observed in accreting neutron stars is the Fe K_α line at 6.4–6.8keV. Some sources also show cyclotron resonance scattering features which will be described in the next section more deeply.

4.3 Cyclotron lines

This section will now give an overview over cyclotron resonance scattering features (CRSF), how they form and what we are able to learn from them. The first CRSF was discovered by Trümper et al. (1978) as an absorption line in the spectrum of Her X-1. The reason for these features is the high magnetic field of accreting neutron stars. When the accreted matter couples to the magnetic field lines quantum mechanical treatment of the electrons becomes necessary. Electrons move along the magnetic field lines on a "screw" trajectory. The quantum effects become important as the B-field of the neutron star gets close to the critical field strength of

$$B_{\mathrm{crit}} = \frac{m\,c}{e\,\hbar} = 44.14 \times 10^{12}\,\mathrm{G} \tag{4.8}$$

Approaching this field strength the *de Broglie* wavelength $\lambda_{\mathrm{deBroglie}} = \hbar/(m\,v)$ of the electron becomes comparable to its Larmor radius $r_{\mathrm{larmor}} = (m\,v_\perp)/(e\,B)$. This results in a quantization of the electrons' momenta of the motion perpendicular to the magnetic field lines (Lai, 2001). The discrete energy levels revealed through the quantization are the *Landau levels*

$$E_n = m_e c^2 \sqrt{1 + \left(\frac{p_\parallel}{m_e c}\right)^2 + 2n\frac{B}{B_{\mathrm{crit}}}} \tag{4.9}$$

where $n \in \mathbb{N}$ is the quantum number, m_e is the electron rest mass, $p_\parallel$ the momentum of the electrons parallel to the magnetic field. The fundamental Landau level is given by the 12-B-12 rule and relates the line energy E_{cyc} of the fundamental CRSF to the magnetic field strength of the neutron star. The 12-B-12 rule is the following:

$$E_{\mathrm{cyc}} = \frac{\hbar e B}{m_e c} \approx 11.56 keV \times B12$$

where B12 is the magnetic field in units of 10^{12} Gauss (Canuto und Ventura 1977). In the non relativistic regime the Landau levels are equally spaced, that means that the higher harmonics have n times the energy of the fundamental CRSF. To date studying CRSF is the only direct way to measure the magnetic field of an accreting neutron star (Harding & Lai, 2006,Orlandini & Fiume, 2001). The magnetic field of a neutron star is an important variable to know to be able to understand accretion and the observed continuum.

4.3.1 Formation

Cyclotron lines are observed as absorption lines in the spectra of accreting neutron stars (Heindl et al., 2004) but they are not due to absorption. They are rather formed because

of scattering processes which will be described further in this chapter. As described before photons are emitted from the accretion column. These photons are able to interact with the incoming material in the relativistic plasma and undergo scattering processes. The scattering cross section is resonant at energies that correspond to the separation of the Landau energies, which are the energies of the incoming electrons due to the high magnetic field. If the photon has an energy E = $h\nu$ equal to the fundamental Landau level and is absorbed by an electron, the electron is excited and moves into the next higher Landau level. An electron in an excited level does not stay there for long, it de-excites emitting a photon with the energy of the fundamental Landau level. Because of the high decay rate from the excited state this is more a scattering process than an absorption (Latal, 1986) and almost all electrons will be in an de-excited state. The first, second, third etc. harmonics are due to de-excitement from a higher level, the electron emits either more than one photon with the same energy or one with n-times the energy of the fundamental. The free mean path of the photons is small (Herold & Ruder, 1979) which means that as soon, as a photon is emitted from an excited electron it almost instantly gets absorbed again. Photons with the cyclotron line can therefore not leave the line forming region. To be able to describe the cyclotron lines of a spectrum one has to take relativistic effects for the photon-electron scattering into account (Harding & Daugherty, 1991) which lead to a slightly anharmonic spacing of the resonant photon energies. The anharmonic spacing also prohibits photons with energies near the Landau level to escape. Inelastic scattering is necessary to change the photon energy to leave the line-forming region. These processes happen close to the surface of the neutron star and because of this the gravitational redshift, z, plays an important role. The observed line energy in a spectrum is shifted by a factor of $\frac{1}{1+z}$ with respect to E_{cyc}. For a non-rotating, spherically symmetric uncharged mass the gravitational redshift, z, at the neutron star surface is given by

$$z = \frac{1}{\sqrt{1 - \frac{2GM}{Rc^2}}} - 1 \tag{4.10}$$

Inserting typical values in this equation like the radius of $R = 10\,\mathrm{km}$ (assuming that the line forming region is located just above the surface) and a mass of $1.4\,M_{\odot}$ this gives $z \sim 0.3$. CRSFs depend strongly on the viewing geometry, and therefore on the pulse phase as the neutron star rotates. Additionally the angle between the magnetic field and the path of the photon plays a role for determining the energy. Taking all that into account the CRSFs are observed at

$$E_n = m_e c^2 \frac{\sqrt{1 + 2n(B/B_{\mathrm{crit}})\sin^2\Theta} - 1}{sin^2\Theta} \frac{1}{1+z} \tag{4.11}$$

where Θ is the angle between the photon direction and the magnetic field vector.

4.3.2 Monte Carlo Simulations

Monte Carlo Simulations are a very well established technique of computational science. It is not one particular method but instead a name of a special technique or approach to solve for a problem. Keeping it very general, Monte Carlo simulations are used to model

all kinds of different processes. In this thesis we will use a Monte Carlo simulation made for modeling the cyclotron resonance scattering feature of accreting neutron stars. This model was implemented by (Schönherr et al., 2007) as a local model for the spectral analysis software package XSPEC (Arnaud, 1996). As start the authors used a code which was originally developed by Araya & Harding (1996), which they revised and generalized. The continuum model that is used should not have any influence on the modeling of the CRSF, that is why the new model was constructed to be independent from the assumed continuum. This was achieved using a Green's function approach. But there were still some assumptions for the line forming region necessary to be able to simulate the formation of a cyclotron resonance scattering feature. The magnetic field is thought to be homogeneous on the size of the line-forming region and simulated between 1×10^{12}G and 7×10^{12}G. As no accreting pulsar today is found to have a lower or higher B-field this covers all possibilities so far. Further considerations are a low-density thermal plasma which means negelction of collisional interactions and photon polarization. The electrons are considered to be in their fundamental Landau state which is justified because they have a comparatively very high cyclotron radiative decay rate but a much smaller collisional excitation rate. That means practically every excited electron decays immediately. Also simulated is the Thomson optical depth which corresponds to the electron column densities through $N_e = \tau_T/\sigma_T$.

Chapter 5

Suzaku

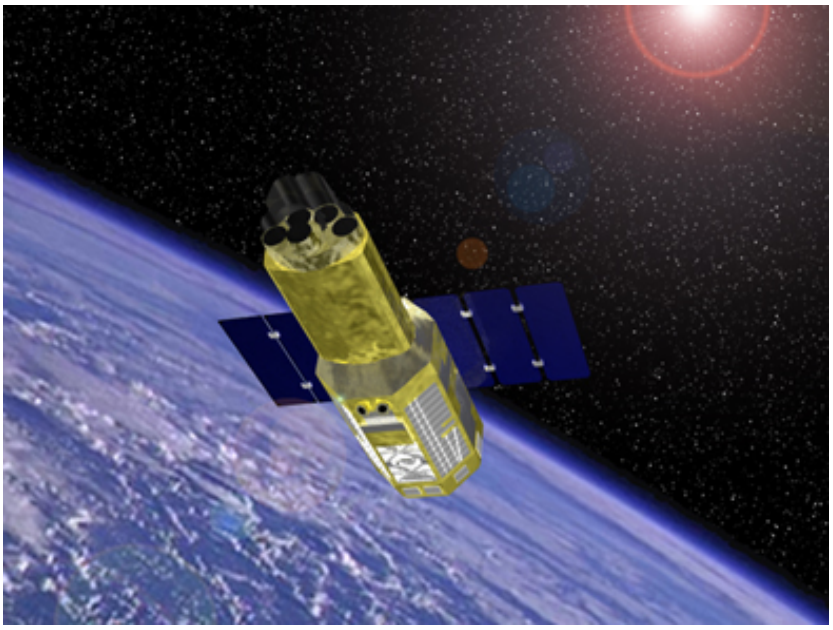

Figure 5.1: The satellite Suzaku. (Image courtesy Takahashi Group: `http://www.astro.isas.jaxa.jp/~takahasi/index-e.html`)

This chapter will give an overview about the satellite Suzaku, its instruments and the technical aspects keeping close to the Suzaku technical description at the Suzaku Guest Observer Facility provided by the NASA's Goddard Space Flight Center [1].

5.1 Spacecraft

On the 10th of February 2000, ASTRO-E, the 5th Japanese X-ray satellite, was launched. But the three staged M-V-rocket was not able to place the spacecraft in its orbit (Inoue, 2003). Five years later the replacement satellite ASTRO-E2 was ready to launch. The

[1] `http://suzaku.gsfc.nasa.gov/docs/astroe/prop_tools/`

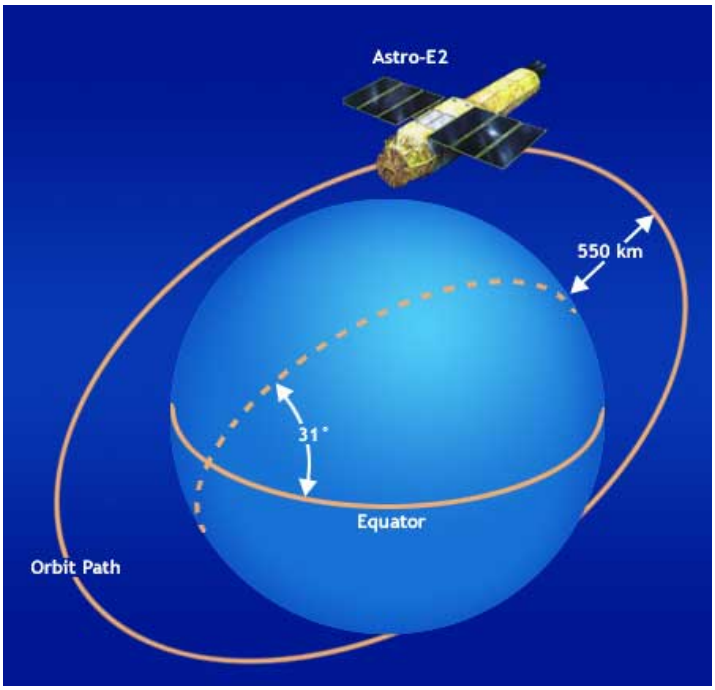

Figure 5.2: A schematic drawing of Suzaku's orbit. (Image courtesy NASA: `http://suzaku.gsfc.nasa.gov/docs/suzaku/prop_tools/suzaku_td/node6.html`

satellite, having a total mass of 1706 kg at launch, rode, again on a three staged M-V-rocket from JAXA Uchinoura Space Center(USC) on the 10th of July 2005 at 3:30 GMT into space and successfully reached its orbit. USC is also the station for up- and downlinks for ASTRO-E2. After deployment of the extensible optical bench the spacecraft has a length of 6.5m along the telescope axis. Developed at the Institute of Space and Astronautical Science of Japan Aerospace Exploration Agency (ISAS/JAXA) in collaboration with U.S.(NASA/GSFC,MIT) and Japanese institutions. After the launch ASTRO-E2 was renamed, as it is common to do so in Japan, to Suzaku. It is the name of a Chinese red phoenix, a bird of the Asian mythology, one of the four guardian animals, protecting the southern skies. The Japanese rocket placed the spacecraft in an almost circular low earth orbit. The apogee of the orbit is 570 km, it has an inclination of 31 degrees and an orbital period of about 96 minutes. The spacecraft has a maximum rate of change for the pointing direction of 6 degrees/min. The pointing direction is limited, observable is only that part of the sky where the sun angle is between 65 degrees and 115 degrees, due to the power constraints of the solar paddle. Despite that, it is at least twice a year possible to observe any part of the sky. Using the star trackers, the settlement to the final attitude takes about 10 minutes (Mitsuda et al., 2007). The normal mode of operations is the satellite pointing in a single direction for at least 1/4 day. With this constraint, most targets, except those near the orbital poles will be occulted by the Earth for about one third of each orbit. Suzaku's pointing accuracy is approximately $0'.24$ with a stability of better than $0'.022$ per 4s. The observing efficiency of the satellite is about 45%, considering additionally that Suzaku cannot observe during passages of the South Atlantic Anomaly.
Suzaku carries three different instruments, the X-ray Imaging Spectrometer (XIS), the

hard x-ray detector(HXD), and an X-ray micro-calorimeter(XRS). It was noticed on the 8th of August 2005 that the X-ray micro-calorimeter lost all its cryogen due to a thermal short between the helium and neon tanks. The cryogen was supposed to cool the instrument to a temperature of -273,09 ℃ and because of this the XRS is not able to do the planned observations. For more details on this instrument see Cottam et al. (2005). The XIS and the HXD are independent from this instrument and therefor able to work even though the XRS is not. Suzaku has a very good X-ray sensitivity covering a broad-band energy range of 0.2 to 600keV. More details about these two instruments will be given in the next two sections. Figure 5.1 gives at the end of this chapter an overview over the capabilities of the spacecraft and its instruments. But despite all that Suzaku is not able to make good observations in every possible way. Appropriate observations to be made with Suzaku are: Studies of diffuse soft X-ray sources with low surface brightness, observations requiring sensitivity above and below 10keV and rapid variability studies on 10ms time scales. If one wants to do observations requiring primarily high spatial and spectral resolution another satellite like Chandra is better qualified.

5.2 X-ray Imaging Spectrometer

Figure 5.3: One of the four XIS detectors. (Image courtesy NASA: `http://heasarc.gsfc.nasa.gov/docs/suzaku/gallery/instruments/xis.html`)

Figure 5.3 shows one of the four XIS detectors on board Suzaku. Each of these four

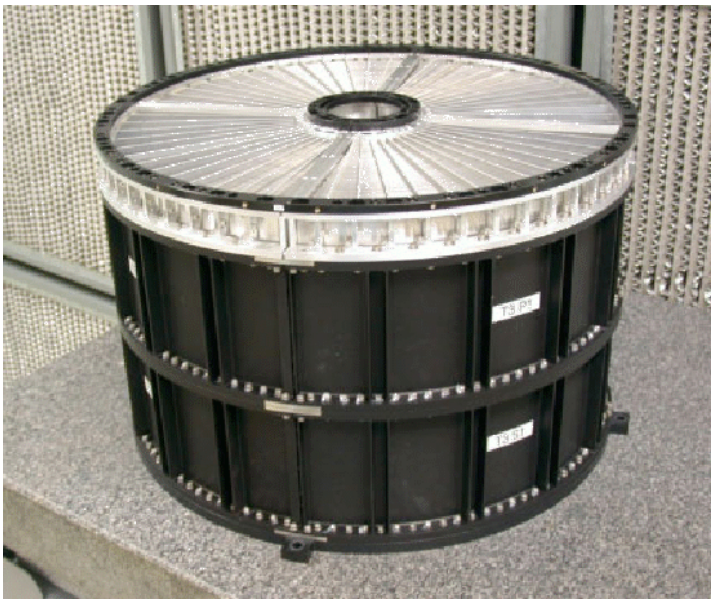

Figure 5.4: One of the five X-ray telescopes. (Image courtesy NASA: `http://heasarc.gsfc.nasa.gov/docs/suzaku/prop_tools/suzaku_td/node9.html`)

sensors is placed at the focal plane of a X-ray telescope (XRT). Figure 5.4 shows one of the XRTs. There are five X-ray telescopes (XRT) that are installed on the top plate of the extensible optical bench (EOB). The so called XRT-S was adapted to the now inoperable XRS and has a focal length of 4,5 m and a diameter of 40 cm. The other four modules have a focal length of 4,75 m and also a diameter of 40 cm, each one dedicated to one of the four XISs, designated as XRT-I0,I1,I2,I3 (Serlemitsos et al., 2007). The telescopes have a cylindrical structure and are light weight, each unit weighing less than 20 kg. They consist of closely nested thin-foil reflectors, reflecting X-rays at small grazing angles, and Wolter-I optics (for more information on these optics see Weisskopf et al. (2002). The angular resolution ranges from $1.8'$ to $2.3'$ and their effective area and field of view are 440cm^2 and $17'$ at 1.5 keV and $250\,\text{cm}^2$ and $13'$ at 8keV. The housing is made of aluminum and an epoxy layer that couples the reflecting gold surface, being as big as 1 million cm^2, to the substrate. Each XRT has a thermal shield integrated on top of the pre-collimator stage to keep them at a temperature between 13 ℃ and 27 ℃. The pre-collimators are mounted on metal rings and are used to eliminate stray light (Mori et al., 2005), which would otherwise be detected at a larger angle than intended. The foils do not have reflecting surfaces. Beneath that are the two stages for X-ray reflection and there is a base ring at the bottom to maintain structural integrity and interface with the EOB of Suzaku. Except for the base ring everything is constructed in 90 segments. For further and more detailed information on the XRTs see Serlemitsos et al. (2007). Together with the XRT the XISs cover an energy range of $0.2-12$keV with a resolution of 130eV at 5.9keV (Nakajima et al., 2004). The XIS's big advantage is their high energy resolution, their large effective area and their low and stable background (see Mitsuda et al. 2007 and Yamaguchi et al. 2006). Figure 5.5 shows graphically the effective area of the XIS, the difference between the FI and the BI will be given later in this section. The seen features in this graphic are due to the elemental composition of

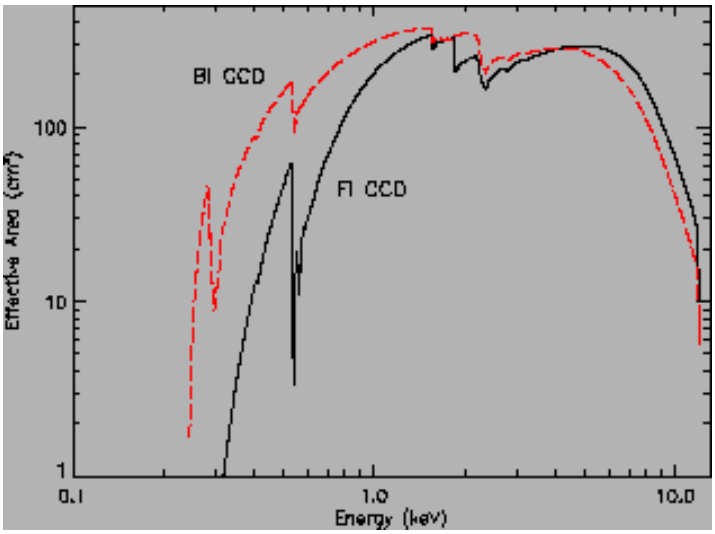

Figure 5.5: XIS effective area of one XRT and XIS system, for both the FI and BI chips. (Image courtesy NASA: `http://heasarc.gsfc.nasa.gov/docs/suzaku/prop_tools/suzaku_td/node6.html`)

the XIS and XRT. One can see K-shell absorption edges from oxygen at 0.54keV and aluminum at 1.56keV present in the blocking filters and weak M-shell features between 2–3 keV from the gold in the XRT.
The combination of clocking and editing modes available for observations allow great flexibility in the data collection. In front of each XIS is a Optical Blocking Filter(OBF) made of 1000$\mathring{A}$ thick polymide coated with aluminum. The OBFs reduce contamination of the X-ray signal by optical light and UV light. Each detector has a X-ray sensitive silicon charge-coupled device (CCD) with a size of 25 mm $\times$ 25 mm. A Thermo-Electric Cooler controlled by Thermal Controller Electronics keeps the temperature of the CCD chip at -90 °C, to minimize thermal noise. The imaging area has 1024×1024 pixels, each pixel being as small as 24 μm $\times$ 24 μm. The CCDs are operated in a photon-counting mode covering, in combination with the XRT a field of view of $18' \times 18'$ (Koyama et al., 2007). In general, X-ray CCDs operate by converting an incident X-ray photon into a electric charge, which in turn produces a voltage. The voltage, often referred to as pulse height, is proportional to the energy of the absorbed X-ray. The true pulse-heights are calculated by subtraction of Dark Levels and possible optical light Leaks. Hot pixels are registered on board and excluded from the event detection process. The chip has four readout nodes, dividing the chip into four segments called A, B, C and D. Each one of these nodes reads the signal from an equal amount of columns and sends it to the RAM. Here each pixel is given RAWX and RAWY coordinates for each segment in the order of the readout. These pixels are named Active pixels. The real coordinates are calculated during ground processing as the readout time depends on the readout node. One detector, the XIS1, uses a back-side illuminated CCD (BI CCD), while the other three use front-side illuminated CCDs (FI CCD). Suzaku's good low energy response of the back illuminated CCD is an important feature. That means XIS1 has a high detection efficiency and a Gaussian-like good energy spread function. The difference between the back and the front illuminated CCD is that the FI CCDs detect the X-rays

that pass through the gate structure, which is placed on the front of the CCD. The disadvantage of them is the photo electric absorption at the gate structure, limiting the low-energy quantum detection efficiency (QDE). The BI CCD is a new technology that collects photons from the back, the side without the gate structure. With an additional thin layer to enhance the efficiency the BI CCD has a high QDE even below 1keV but a lower one for the high energy band (Yamaguchi et al., 2006). The XIS has been partially developed at MIT (CCD sensors, analog electronics, thermo-electric coolers, and temperature control electronics), while the digital electronics and a part of the sensor housing were developed in Japan, jointly by Kyoto University, Osaka University, Rikkyo University, Ehime University, and ISAS. Today only three of the XISs are working. After about 2/3 of the image of XIS2 was flooded with a large amount of leaked charge on the 9th of November 2006 at 1 : 30 UT, XIS2 was stopped to use for observations. One possible explanation for this might be the hit of a micrometeorite. Until now there is no successful solution to this problem and XIS2 remains inoperable.

5.3 Hard X-ray Detector

Figure 5.6: The hard X-ray detector. (Image courtesy NASA: `http://heasarc.gsfc.nasa.gov/docs/suzaku/gallery/instruments/hxd.html`)

The Hard X-ray Detector (HXD)(see figure 5.6) is a non-imaging and collimated hard X-ray scintillation instrument. It has been developed jointly by the University of Tokyo, Aoyama Gakuin University, Hiroshima University, ISAS/JAXA, Kanazawa

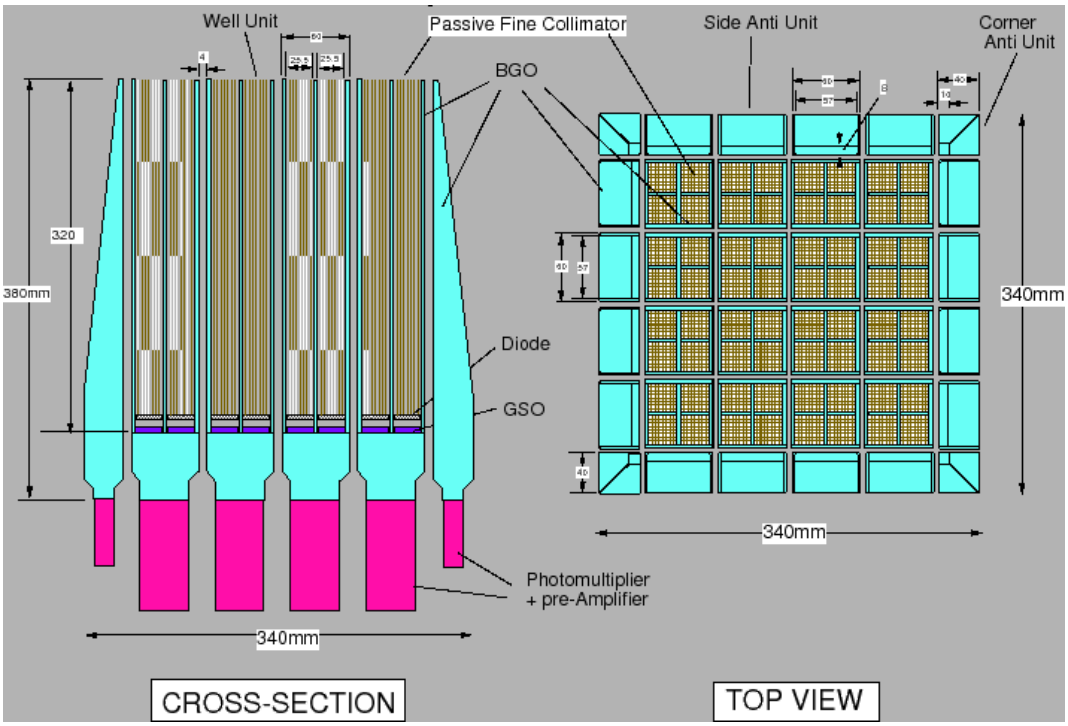

Figure 5.7: Schematic drawing of the hard X-ray detector. (Image courtesy NASA: `http://heasarc.gsfc.nasa.gov/docs/suzaku/prop_tools/suzaku_td/node11.html`)

University, Osaka University, Saitama University, SLAC, and RIKEN. Its main purpose is to extend the bandpass of the Suzaku observatory to the highest feasible energies, thus allowing broad-band studies of celestial objects. It is not the first mission that carries an instrument sensitive in the $\sim$ 10 keV to $\sim$ 600 keV band. But observations in this band are very difficult because of the background being sometimes higher than the actual signal from the source and the inclined low-earth orbit also causes problems in terms of fluctuations of the background. For further information on the background see Kawaharada et al. (2004). Two techniques are combined to keep the background as low as possible, the compound-eye configuration and the well-type active shield. The compound-eye detector consists of 16 main detectors arranged as a square. For active shielding they are surrounded by 20 crystal scintillators. All these instruments are located inside the well. The HXD has an effective area of $\sim 160\,\mathrm{cm}^2$ at 20keV and $\sim 260\,\mathrm{cm}^2$ at 100 keV. The detector has a time resolution of only 61μs, for more details on timing see Terada et al. (2007). Each detector is a combination of two different detectors, a GSO/BGO phoswich counter and 2mm-thick PIN silicon diodes. The PIN diodes are sensitive below 60keV with an energy resolution of approximately 4keV, providing the low energy response of the HXD. The effective area of the PIN is limited to $\sim 16.5 \times 16.5\,\mathrm{mm}^2$ by a guarding ring structure although the actual area is $21.5 \times 21.5\,\mathrm{mm}^2$. The temperature of the PIN diodes are controlled to $-15 \pm 3\,^{\circ}\mathrm{C}$ to suppress electrical noises caused by the leakage current, and almost fully depleted by giving a bias voltage of $\sim$ 500V. The PIN diodes absorb X-rays with energies below $\sim$ 70keV, but for higher energies they are becoming gradually transparent. The harder

X-rays are detected by the GSO detectors, that are located under the silicon diodes. These detectors are made of Gadolinium Silicate crystal. Each unit forms a 2×2 matrix with four 5mm thick GSO crystals. They have a size of $24\,\mathrm{mm} \times 24\,\mathrm{mm}$. The GSO/BGO phoswich counter(scintillator) is sensitive above 40keV and has an energy resolution of $7.6/\sqrt{\mathrm{E}}$ where E is energy in MeV. BGO is an abbreviation for the material Bismuth Germanate. The scintillator signals are read out by photomultiplier tubes(PMTs). The PMTs are able to discriminate in which of the two detectors the event may have been occurred, making it possible to disregard any particles that were registered by both scintillators. The X-rays are photoelectrically absorbed in the PIN diodes, and the signal is amplified, converted to a digital form, and read out by the associated electronics. The PIN diodes are of course also actively shielded from particle events by the BGO shields, as they are placed inside the deep BGO wells. The BGO shields are made of $\sim$ 4cm thick Bismuth Germanate crystals. In addition, to reduce the contamination by the cosmic X-ray background, passive shields called "fine collimators" are inserted in the well-type BGO collimator above the PIN diodes. The fine collimator is made of 50 μm thick phosphor bronze sheet, arranged to form a 8×8 square meshes of 3 mm wide and 300 mm long each. The BGO scintillators actively collimate the field of view to $4.5^\circ \times 4.5^\circ$. At energies below $\approx$ 100keV, an additional passive collimation further reduces the field of view to $34' \times 34'$. Even though the HXD is meant for faint stars, it can also tolerate very bright sources up to $\approx$ 10Crab. The HXD performs also as an all sky monitor called Wide-band All-sky Monitor (WAM). The four anti coincidence counters (BGO) that are meant for tight active shielding, one on every side of the HXD sensor, are used to record a pulse height histogram. The energy coverage ranges from $\sim$ 50keV to $\sim$ 5 MeV, the effective area is $\sim$ 800cm^2 at 100keV and $\sim$ 400cm^2 at 1MeV. The time resolution of WAM is one second but if a energy burst is detected, for example from a transient, the time resolution will be 31.25ms.

S/C	Orbit Apogee	568 km
	Orbital Period	96 minutes
	Observing Efficiency	$\sim 45\%$
XRT	Focal length	4.75 m
	Field of View	$17'$ at 1.5 keV
		$13'$ at 8 keV
	Plate scale	0.724 arcmin/mm
	Effective Area	440 cm^2 at 1.5 keV
		250 cm^2 at 8 keV
	Angular Resolution	$2'$ (HPD)
XIS	Field of View	$17.8' \times 17.8'$
	Bandpass	0.2–12 keV
	Pixel grid	1024×1024
	Pixel size	24 μm$\times$ 24 μm
	Energy Resolution	~ 130 eV at 6 keV
	Effective Area	340 cm^2 (FI), 390 cm^2 (BI) at 1.5 keV
	(incl XRT-I)	150 cm^2 (FI), 100 cm^2 (BI) at 8 keV
	Time Resolution	8 s (Normal mode), 7.8 ms (P-Sum mode)
HXD	Field of View	$4.5° \times 4.5°$ ($\gtrsim 100$ keV)
	Field of View	$34' \times 34'$ ($\lesssim 100$ keV)
	Bandpass	10 – 600 keV
	– PIN	10 – 70 keV
	– GSO	40 – 600 keV
	Energy Resolution (PIN)	~ 4.0 keV (FWHM)
	Energy Resolution (GSO)	$7.6/\sqrt{E_{MeV}}$ % (FWHM)
	Effective area	$\sim 160\,cm^2$ at 20 keV, $\sim 260\,cm^2$ at 100 keV
	Time Resolution	61 μs
HXD-WAM	Field of View	2π (non-pointing)
	Bandpass	50 keV – 5 MeV
	Effective Area	800 cm^2 at 100 keV / 400 cm^2 at 1 MeV
	Time Resolution	31.25 ms for GRB, 1 s for All-Sky-Monitor

Table 5.1: Overview of Suzaku's capabilities. (Image courtesy NASA: `http://suzaku.gsfc.nasa.gov/docs/suzaku/prop_tools/suzaku_td/node6.html`)

Chapter 6

Suzaku Observation

This chapter will at first give a historical overview over the neutron star 4U 1907+09 showing which interesting results were gained from which observation since its discovery. After that it will be described what software was used and how the data was reduced to be able to analyze it afterwards. The next sections are then dedicated to the analysis and the results that were found from lightcurves, pulse profiles and phase averaged and resolved spectra.

6.1 The neutron star 4U 1907+09

The neutron star 4U 1907+09 is a wind accreting HMXB pulsar with a highly reddened ($E_{B-V} = 3.45$mag) O8–O9 Ia supergiant companion, referred to as 4U 1907+097. The companion has a magnitude of $m = 16{,}37$ mag, an effective temperature of 30 500 K, a radius of $r = 26R_{\odot}$, a luminosity of $L = 5 \times 10^5 L_{\odot}$ and a mass loss rate of $\dot{M} = 7 \times 10^{-6} M_{\odot}\mathrm{yr}^{-1}$ (Cox et al., 2005b). 4U 1907+097 shows broad H_{α} emission (Schwartz et al., 1980), identifying the system as a high mass X-ray binary. The 4U in the name of this source stands for the fourth UHURU catalogue, where it was listed for the first time and discovered as an X-ray source by Giacconi et al. (1971). Giving every star a special name would have been impossible, that's why the numbers after the 4U simply stand for its right ascension and its declination.
Suzaku observed the source 4U 1907+09 twice, the first time for $\approx$ 44,0ksec on 2006 May 2–3 and the second time for $\approx$ 69,5ksec on 2007 April 19–21. Suzaku is only one of the many satellites that provided data of this source for studies. *Ariel V, Tenma, EXOSAT* and *Ginga* for example are other satellites that observed 4U 1907+09 earlier. Marshall & Ricketts (1980) first determined the orbital period of the binary to 8.38 days by analyzing data taken between 1974 and 1980 with *Ariel V* resulting in an amount of data equivalent to about 6 months of continuous observation. They also reported a luminous outburst in the data taken in 1980 January. This outburst was simultaneously observed by the *Hakucho* satellite (Marshall et al., 1980a). This flare was recognized to occur twice per orbital period with a larger primary and a smaller secondary flare at orbital phase ~ 0.45 and ~ 0.90. This result was later found to be consistent with other observations (see, e.g., Makishima et al., 1984 or Cook & Page 1987). At that time 4U 1907+09 was not yet recognized as a pulsar. Another 4 years later Makishima et al.

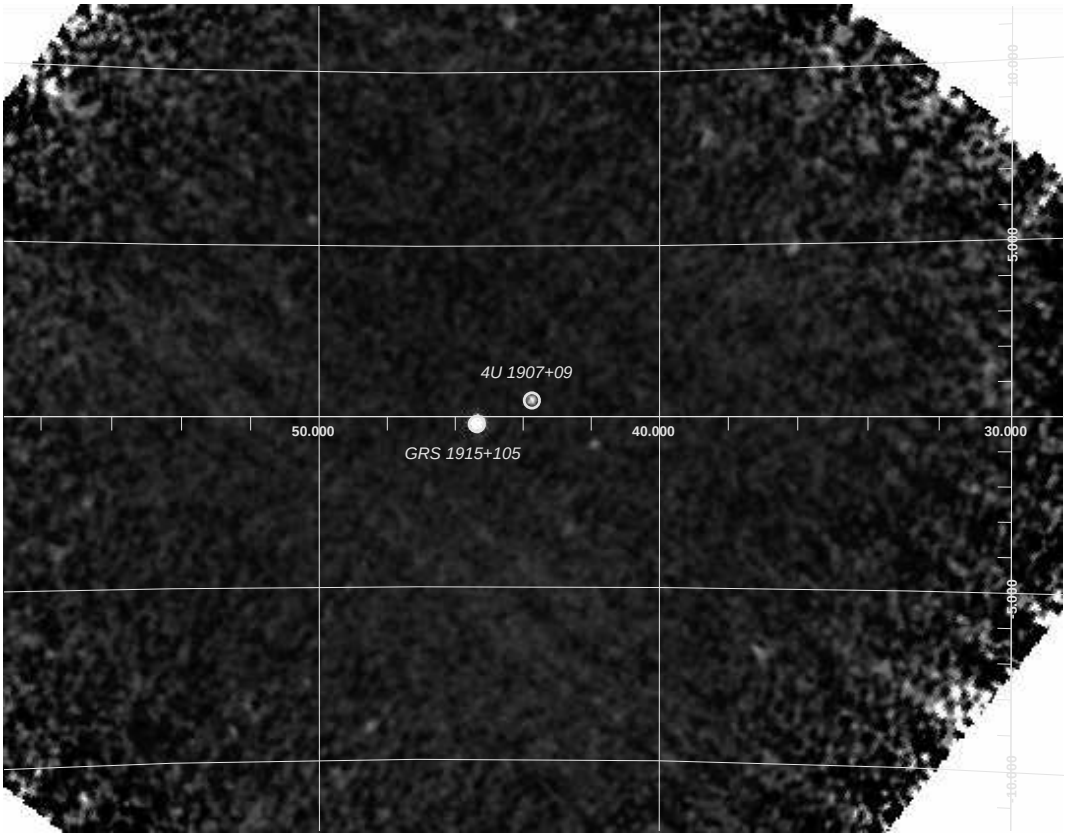

Figure 6.1: ISGRI Image of the 4U 1907+09 region in the 20-40 keV band, exposure time about 100ks. Image courtesy Fritz et al. (2006)

(1984) were the first to discover 4U 1907+09 as pulsar with a pulse period of 437.5s by analyzing data that was taken in 1983 with the satellite Tenma. Sadeh & Livio (1982) noticed in data taken in October 1977 by the HEAO satellite that during that time the source showed 15ms oscillations which lasted for about 10 seconds. Cook & Page (1987) combining Tenma and EXOSAT data, determined a moderate eccentricity of $0.16^{+0.14}_{-0.11}$, they found a pulse period of 437.656 ± 0.012s which was not consistent with the one found from Tenma data before. Between the 270 days of the observations 4U 1907+09 showed a mean spin-down rate of $\sim 0.23 \pm 0.02\,\mathrm{s\,yr^{-1}}$. in't Zand et al. (1998) used data from the Rossi X-ray Timing Explorer(RXTE) taken in February 1996 to identify the eccentricity to be $e = 0.28^{+0.10}_{-0.14}$. These authors found a mean X-ray luminosity of 4U 1907+09 is $L = 8 \times 10^{34} d^2_{kpc} erg\, s^{-1}$ showing complete dips with durations of minutes to 1.5hr . The distance between the neutron star and its massive companion was found to be $2.4 - 5.9$kpc by van Kerkwijk et al. (1989).
Makishima & Mihara (1992) were the first to report a cyclotron feature at 21 keV found in an observation with Ginga in 1990. The binary separation of the two stars is $a = 54 R_\odot$ and the Roche lobe is $R_L = 43 R_\odot$ (in't Zand et al., 1998). The neutron star has a magnetic field of $B = 2.1 - 2.5 \times 10^{12}\,G$ (Makishima & Mihara 1992, Cusumano et al. 1998). For a long time there was a debate if 4U 1907+09 is really a wind accreter or if the companion is a Be star. Flaring, which can be seen twice per neutron star orbit (Marshall et al., 1980b) would suggest that the companion might be a Be star. But this

would imply that the distance is < 1.5kpc, which is in contradiction to the distance that was found by van Kerkwijk et al. (1989) or Cox et al. (2005a) who determined the distance to be 5kpc. The second reason why 4U 1907+09 and its companion is not a Be-system is the orbital period, which for Be-systems is approximately 30–200 days and for binary systems with a supergiant companion around 1–10 days. This classifies the companion of 4U 1907+09 as a supergiant with its orbital period of $P_{\rm orb}$ = 8.3753 days (Cox et al., 2005b). An analysis of a flare observed with the Indian X-Ray Astronomy Experiment (IXAE) during August 1996 showed the presence of transient 14.4s oscillations, which may be quasi-periodic during the flaring activity but have a different period than the reported oscillations of 18.2 s as detected by RXTE in February 1996 (Mukerjee et al., 2001).

Table 6.1: Binary Orbit and pulse period from 1983 Tenma and 1996 RXTE-PCA measurements, for the twelve years between the Tenma and the RXTE observation there was no change in the orbital Period, the longitude of periastron or the inclination. (Adopted from in't Zand et al. 1998)

Parameter	Symbol	Value	$1/\sigma$ error
Orbital period	$P_{\rm orb}$	8.3753 days	0.0001
Eccentricity	e	0.28	0.04
Orbital epoch	$T_{\pi/2}$	MJD 50134.76	0.06
Longitude of periastron	ω	330	7
Projected semimajor axis length	$a_x \sin$ i/c	83 lt-s	2

6.2 Data analysis and reduction

6.2.1 Introduction

All Suzaku specific software needed to analyze and reduce the data is written by the instrument teams of Suzaku. This software is released as part of the HEAsoft package (also called FTOOLS) and available at HEASARCs Guest Observer Facility of Suzaku[1]. HEAsoft is a multimission collection of programs and scripts. Part of it is for example XSPEC for spectral analysis or XSelect for extraction of data into spectra, images and lightcurves. Calibration information are also provided, by the HEASARC "Calibration Database"(CALDB). For the analysis and reduction of the two observations event files from v2.6.1.3. processing and software version 6.0 (CALDB 2007-01-31) was used. For the data reduction we kept close to the *Data Reduction guide* (also known as *ABC guide*) which is also available at the Suzaku Guest Observer Facility.
All Suzaku data files are in FITS format and include the following folders and files: One folder called **auxil** containing spacecraft associated files like attitude, orbit or filter files. Another folder, the **log**, contains files from the data processing. And there is a folder for each instrument, the **HXD** and the **XIS** containing: unfiltered event files, cleaned event files that have gone through the standard cuts, housekeeping files specific to the

[1] `http://heasarc.gsfc.nasa.gov/docs/suzaku/`

instrument and product files from the pipeline such as images and lightcurves. The product files are only for quick look purposes, it is not recommended to use them for actual data analysis. How the images and lightcurves were gained from the raw data will be explained in this section.
Both instruments are energy sensitive, each event has therefore a measured "Pulse Height Amplitude"(PHA). The PHA depends on the instrument and may for this reason be position and or time varying. Applying instrumental calibration and gain drift a PHA Invariant(PI) is calculated and available in the data received. The PI column in the event files is the one used to extract energy spectra an light curves. The PI column of XIS takes values from 0 to 4095. The HXD PI column to be used is the PI_PIN that takes values from 0 to 255. The corresponding time column gives the elapsed time in seconds from the beginning of the year 2000 in UTC.

6.2.2 XIS reduction

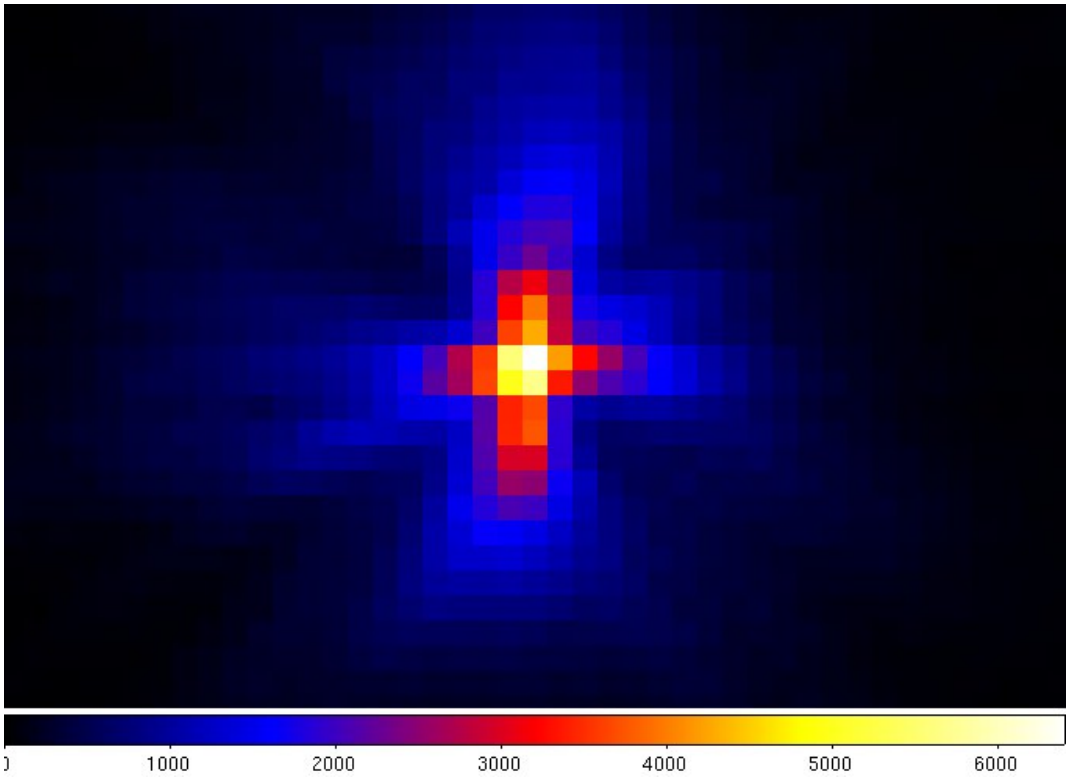

Figure 6.2: Image of 4U 1907+09.

There are three observational editing modes usable, the observation analyzed in this work was made in the 3×3 mode and the 5×5 mode. The 5×5 mode sends all the pulse heights of the 25 pixels centered at the event center to the telemetry. The 3×3 mode only sends pulse heights of the 9 pixels centered at the event center to the telemetry. But in addition, in this mode a 16 bit pixel pattern is output which indicates if pulse heights of the outer 16 pixels exceeded the split thresholds or not. Sums of the outer pixel pulse heights lower than the split threshold are also output.

In a first step of the analysis, the photon arrival times were bary-centered to the solar system. For the extraction of the spectra we used xselect and read both event files. Select mkf is a command that is set automatically by xselect on read events and one that creates a time filter of good times. Select mkf uses the filter files that are located in the auxil directory to delete unusable data. With this command we excluded data that was taken during (SAA=0) and 436 seconds (T_SAA $>$ 436) after passage of the South Atlantic Anomaly (SAA). The radiation in this part of the sky is greater than anywhere else because the Earth's inner van Allen radiation belt is at that point closest to our earth. The instruments cannot know what radiation came from the source and what from the SAA, so this part of the observation is disregarded completely. We also filtered events when the pointing direction was less than 10 degrees above earth (ELV $>$ 10) to eliminate particles that did not come from the source but were scattered from the atmosphere, that is opaque for X-rays. Additionally, for our analysis we did not take into account data taken while the pointing direction was 20 degrees below the sunlit limb of Earth (DYE_ELV $>$ 20) to exclude solar X-rays scattered from the sunlit Earth. To improve the particle background rate affected through geomagnetic cut-off rigidity we applied the criteria COR greater 6GV which can reduce the effective exposure time somewhat but may improve the signal-to-noise ratio. We used *Detector coordinates*, these are the physical positions of pixels within each sensor. Misalignments between the sensors are not taken into account, but the *Det images* will give correct sky images of the object as opposed to mirrored ones. X-ray images focused by the mirrors and detected by the focal plane instruments will be the mirror images, which have to be flipped to be the actual images of celestial objects. Thus, the original look-down images are flipped (and rotated if necessary) so that the satellite +Y-axis direction will be the DETY direction. Other possibilities would have been to use *sky coordinates* giving sky positions relative to a celestial reference point, the "x" and "y" columns are computed using attitude information from the attitude file. Or *Focal plane coordinates* giving the event location on the focal plane; or *Actual pixel locations* on the chip or pixel locations on each segment.
Using ds9 an extraction region was selected. As the observation was made of a point source a circular region centered at the source with a radius which encircles most of the point flux was made. The region was used as filter to extract the events into spectra and lightcurves.
The *Redistribution Matrix File*, from now an abbreviated with response file, was generated using xisrmfgen, which is part of the HEAsoft package and takes into account the time variation on the energy response. The above created imagefile was used as input. Xisrmfgen needs the spectral file to be in detector coordinates, they were chosen before as described above. Before the next step the event files were combined with XSelect. Xissimarfgen was used to generate ancillary response files(ARFs). This script uses Monte-Carlo simulations to estimate the number of events expected to be detected in the defined extraction region. It describes the XRT response and the amount of built-up contamination on the XIS optical blocking filter. For more information on this software see Ishisaki et al. (2007). The filters used to extract the images were the same as before and applied again. The program xissimarfgen needs for its simulation information about the source, these were for 4U 1907+09:

Instrument name: (XIS0,1,2,3)
right ascension of the source: 287.41526
declination of the source: 9.82738
detreg (Detector region, particular region within a single detector)
before selected regionfile
the number of photons to be used for the simulation: 400000
(they need to be this high to limit statistical errors)
the eventfile (for example xis0.evt for the XIS0 detector)
the attitude file from the auxil directory
the before generated response file
energy step file: default, which will give a sufficient energy resolution
Screened XIS event data still include particle and X-ray background events. This background can be estimated from the part of the CCD chip, that is off-source. If the source is extended this is not possible and it can be estimated during the observations of the same target from the night Earth data. These were collected and are also available through the CALDB. The XIS background depends strongly on the cut-off-rigidity in orbit (Koyama et al., 2007). Provided is also the software to make COR weighted background spectra to take this dependency into account. The software is ./mk-corsorted-spec-v1.0.pl and mk-corweighted-bgd-v1.0.pl.

6.2.3 PIN reduction

For the XIS data it is not always possible to gain a background from the data, for the PIN it is never possible to estimate the background from the observation data themselves as the PIN is a collimated instrument. For this reason, the HXD team has developed and run a model of the time-variable particle background, the hereby gained results are made public. The background model is calibrated using day and night Earth data, which will limit the absolute accuracy depending on the amount of data available. The current uncertainty is estimated to be about 3.2 percent in the 15-40keV range. The background files only model the particle background. The cosmic X-ray background must be evaluated separately. PIN non X-ray background (NXB) files are available at `ftp://legacy.gsfc.nasa.gov/suzaku/data/background/pinnxb_ver2.0/`. For the analysis and to be able to apply further filter we merged the good time interval (GTI) extension from the background event files and the GTI from our filtering criteria. The extraction of the spectrum and the internal background was made by applying the GTI file as generated above with Xselect. Further we did a deadtime correction, which is necessary to correct for the dead time of the observed spectrum to be able to apply the background file correctly. This correction was only applied to the event files, for the background files this is not necessary. The dead time correction tool is hxddtcor included in the Heasoft package. This program updates the EXPOSURE keyword of the spectral file, by comparing the number of pseudo events injected by the analog electronics on-board with that found in the telemetry. The event rate in the PIN background event file is 10 times higher than the real background to suppress the Poisson errors. We corrected for this feature by increasing the exposure time of the derived background spectra and light curves by a factor of 10. The background event file does not include the cosmic X-ray background (CXB). Since the CXB flux is about 5 percent

of the background for the PIN, this is something that has to be taken into account after subtracting the non X-ray background. We used a method which estimates the CXB level by using the PIN response for the flat emission distribution. This response is provided and is appropriate for large extended sources. It assumes that the uniform emission is from the region of 2×2 pixels. The CXB contribution to the PIN background is simulated with xspec using a typical CXB spectrum based on the HEAO-2 results (Boldt, 1987) and accounting for the 4square degree field of view. As soon as this has been done with xspec we used the fakeit command using the pinflat response matrix. We had XIS nominal position. The NXB background file and the simulated CXB PHA file can be added making sure that the EXPOSURE keyword should be the common value.

6.3 Lightcurves

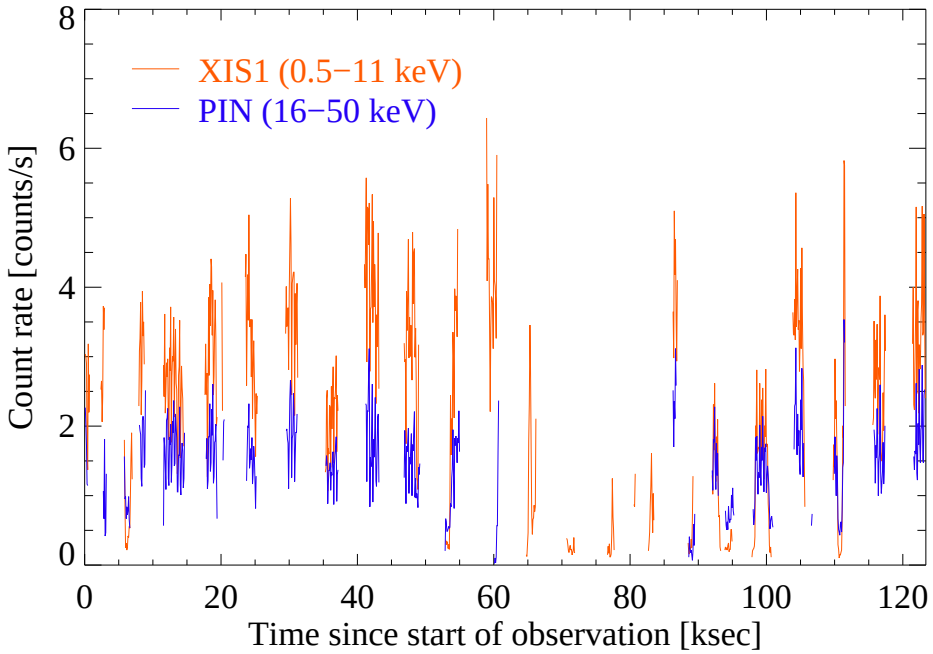

Figure 6.3: Lightcurve of 2006 data

For the lightcurves, the raw count rate over time, we chose the back illuminated XIS1 and the PIN. Figure 6.3 shows the barycenter corrected XIS1 raw count rate over time in the energy band of 0.5–11 keV (displayed in red) and the raw count rate over time of the PIN in the energy band from 16–50 keV (displayed in blue) for the 2006 data. The lightcurves were binned to a time resolution of 100s. Both light curves are not background subtracted, since they are source dominated. Figure 6.4 shows the count rates of the same two detectors in the same energy bands for the data taken in 2007, binned to 100s and not background subtracted. Suzaku has an orbital period of $\sim$ 96 min, which means that observed sources will be occulted by the earth for about one third of each orbit. The occultations by the earth are the reason for the

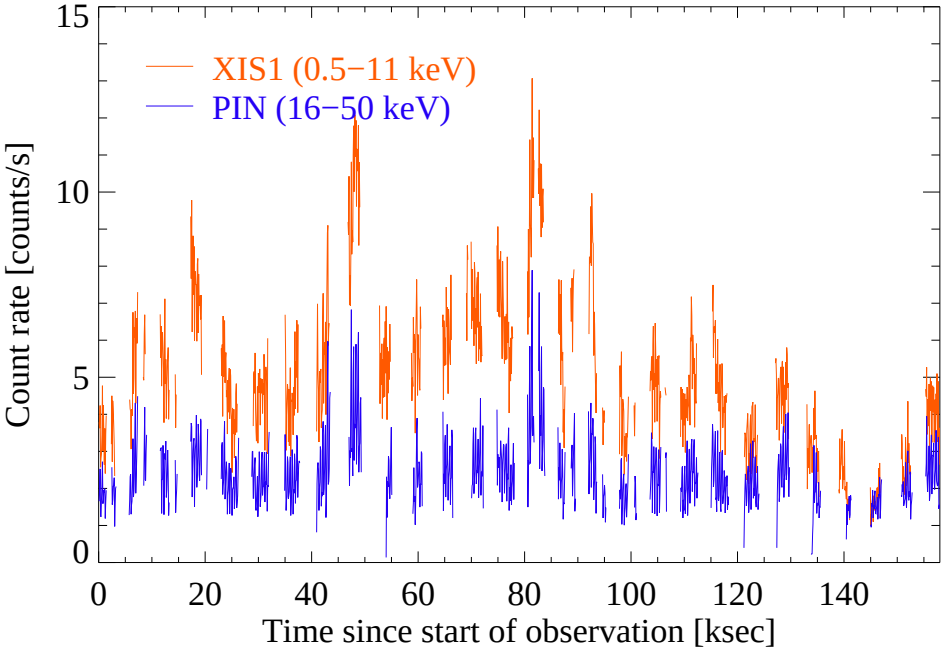

Figure 6.4: Lightcurve of 2007 data

gaps in the lightcurve. Additionally the gaps are also due to passages through the South Atlantic Anomaly. In 2007 the source was about a factor of 2 brighter than in 2006. The mean countrate for the data taken in 2006 is 2.38 cts/s for the XIS1, in the lower energy band and 1.04 cts/s for the PIN in the higher energy band. For the observation in 2007 the mean countrate is 5.24 cts/s for the XIS1 and 2.28 cts/s for the PIN. The X-ray lightcurves show a clearly pulsed signal, for the data taken in 2007 we took a closer look at part of the lightcurve beginning 21 ksec after the start of the observation and for 19 ksec to emphasize on the pulsed signal (figure 6.5). The period of the pulse is approximately ~ 441 s (for more details on the pulse period see section 6.4). The variable count rate reflects the orbital phase dependent variability. 4U 1907+09 is known to exhibit flares on a timescale of hours (Makishima et al., 1984). In a RXTE observation in 1996 the net intensity rose by an order of magnitude to about 0.1 Crab, this is twice the intensity that was recognized during a flare from a Tenma observation in 1984. Something interesting found in the RXTE data by in't Zand et al. (1998) was that looking at the orbital phase the flare occurred near apastron of the binary. During flares, in't Zand et al. (1998) and Mukerjee et al. (2001) also reported the detection of transient 18.2 s and 14.4 s quasi-periodic oscillations. The typical flaring behavior can be seen in our observation from 2007 (figure 6.4) when the source showed several flares with durations of 1–2 hours. The flares observed with INTEGRAL in the 20–40 keV band (Fritz et al., 2006) are similar to the ones we observed with Suzaku. In 2006 the observation is dominated by equally typical, non-absorption-related dipping behavior. The correlated dipping activity is clearly visible in the soft and hard energy bands (figure 6.3), confirming earlier results by in 't Zand et al. (1997) that the dips are not due to absorption. Figure 6.6 shows the hardness ratio for the observation taken in 2006 with hard being the energy band from 16–50keV and soft the energy band from

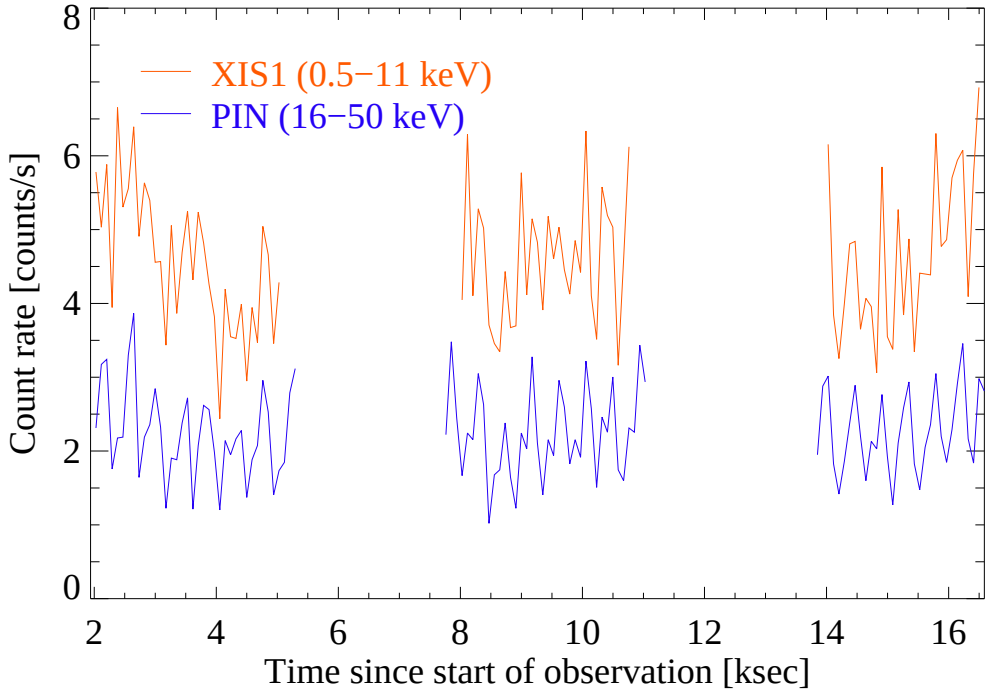

Figure 6.5: Part of the lightcurve of 2007 data

1–10keV. Since 4U 1907+09 can become bright during flares, the 2006 observation was performed in 1/4 window mode. A slightly different strategy was used for the 2007 observation, the goal was to obtain maximum sensitivity for the cyclotron line. This strategy led to the full window mode in this case. With total source rates of < 10cps per XIS module, pile-up turned out not to be a problem in the 2006 observation, while maximum flares rates of ≤ 15cps in 2007 might have a moderate effect.

6.4 Pulse periods and profiles

Makishima et al. (1984) were the first to discover pulsations from the neutron star 4U 1907+09. The authors found the source to be slowly rotating with a pulse period of 437.5 s. Further observations showed that the pulse period is not constant, but is continuously becoming greater. This means that the neutron star shows a steady spin down. The pulse period increased from being 437.5s in 1983 to 440.76s in 1997 (in't Zand et al., 1998) with an average of $\dot{P}_{\rm Pulse} = +0.225\,{\rm s\,yr^{-1}}$. This increase is the longest continuous spin down in history for an accretion powered pulsar (Fritz et al., 2006). This spin down behavior changed in the year 2002, when Baykal et al. (2006) reported, from an analysis of data taken with RXTE, that the source showed a decrease in $\dot{P}_{\rm Pulse}$. The authors found a spin-down rate of $\dot{P}_{\rm Pulse} = 0.115\,{\rm s\,yr^{-1}}$ which is about ~ 0.5 times the long term value and the the rate obtained between 1996 and 1997 (Baykal et al., 2001). Fritz et al. (2006) then reported the first torque reversal of the neutron star 4U 1907+09 since its discovery. From observations taken with INTEGRAL through 2003 to 2005 they confirmed the slowing down of the spin-down rate and showed that the trend has changed from MJD53131 onwards to a spin up trend with $\dot{P}_{\rm Pulse} = -0.158 \pm 0.007{\rm s\,yr^{-1}}$.

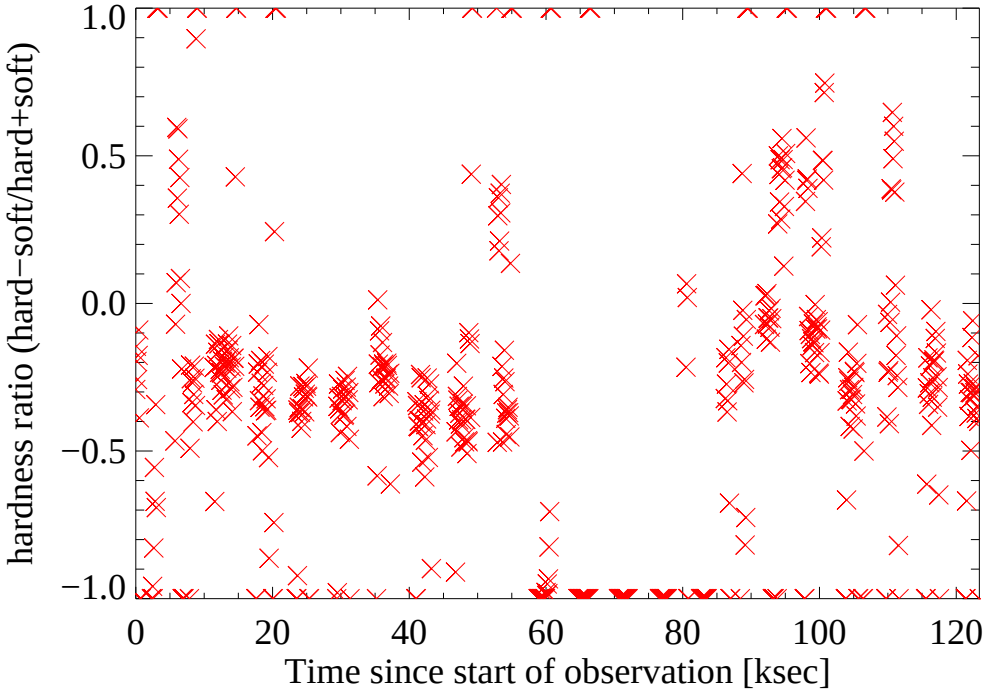

Figure 6.6: Hardness ratio for the 2006 observation with the hard energy band from 16–50keV and the soft from 1–10keV

The pulse profile of the neutron star 4U 1907+09 is highly variable as recognized before by in 't Zand et al. (1997). There are pulse to pulse variations as well as changes within one pulse. But the profile has not changed noticeably since the RXTE observation analyzed by in't Zand et al. (1998): the pulse profile shows two peaks with a deep and shallow minimum. The minima are approximately a half pulse phase apart. Also unchanged is the energy dependency which is similar to that observed in Cen X-3 with Ginga (Nagase et al., 1992). Looking at figures 6.7 and 6.8, one can see that the first pulse seems to disappear as we move to higher energies, while the second pulse changes its shape. The profile of the 2006 data shows a stronger pulse than the one of the 2007 data.

To obtain the pulse periods of the two Suzaku measurements we barycentered the data and took the binary motion of the neutron star into account. For each of the observations, we then performed a period search using epoch folding (Leahy et al., 1983). Because of the high-resolution of the PIN with $61\mu s$ (Terada et al., 2007) we used the PIN light curves to determine the updated pulse periods. The epoch folding of the 2007 observation is shown in figure 6.9 and shows clearly that the pulse period has to be approximately 441 s. For the data taken in 2006 we derived a pulse period of $P_{\mathrm{Pulse}} = 441.27 \pm 0.05\,\mathrm{s}$ and for 2007 of $P_{\mathrm{Pulse}} = 441.09 \pm 0.05\,\mathrm{s}$. Figure 6.10 shows the period evolution of 4U 1907+09 for almost 25 years, the two latest measurements, marked with blue triangles, correspond to the Suzaku observations discussed in this thesis. The turn in the trend from spin-down to spin-up is obvious. Comparing the pulse periods from the Suzaku observations in 2006 and 2007 we find the source to be spinning up. But looking at the pulse periods from earlier data a continued spin up

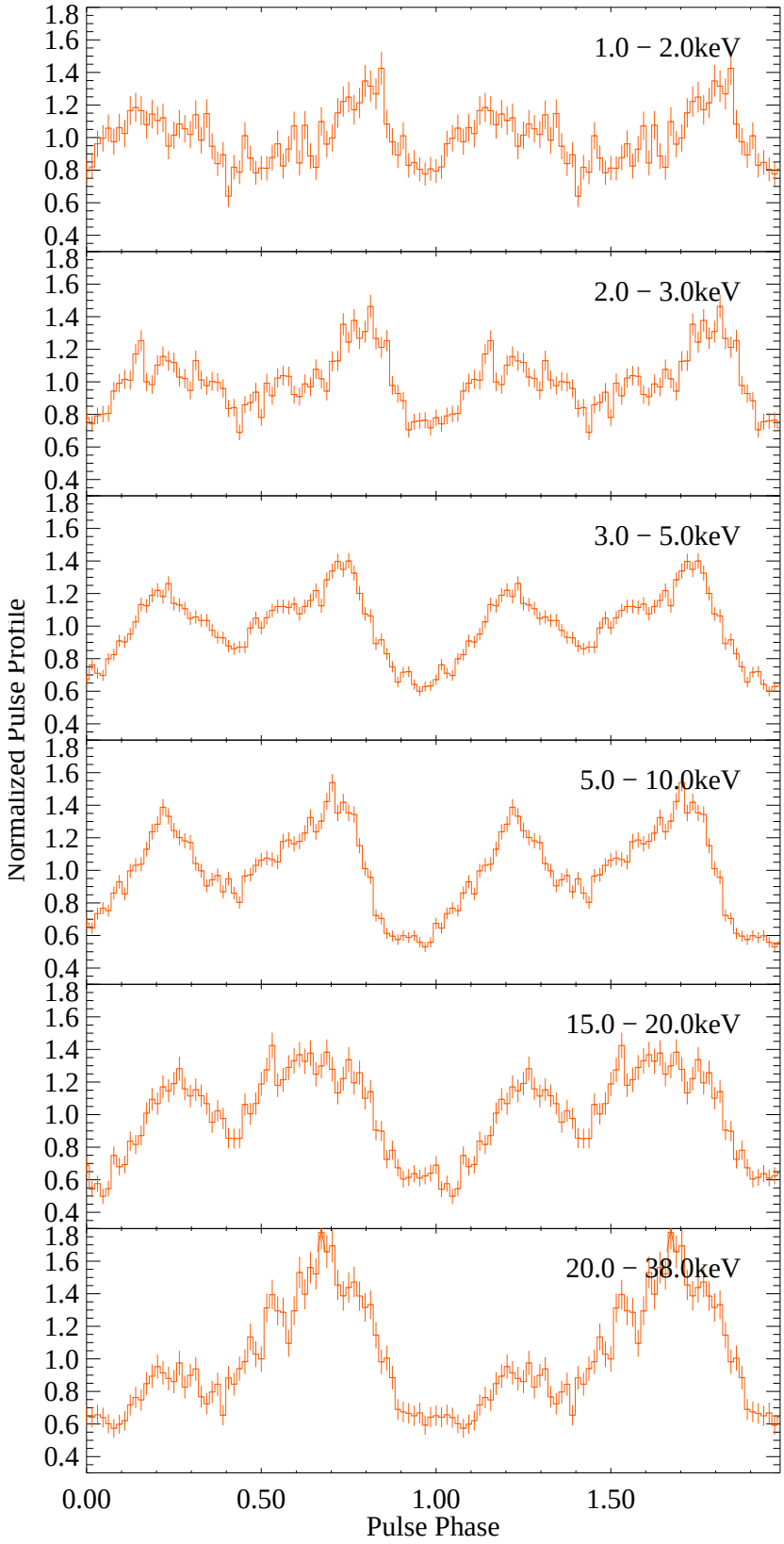

Figure 6.7: The energy resolved pulse profile of the 2006 observation normalized to the mean countrate.

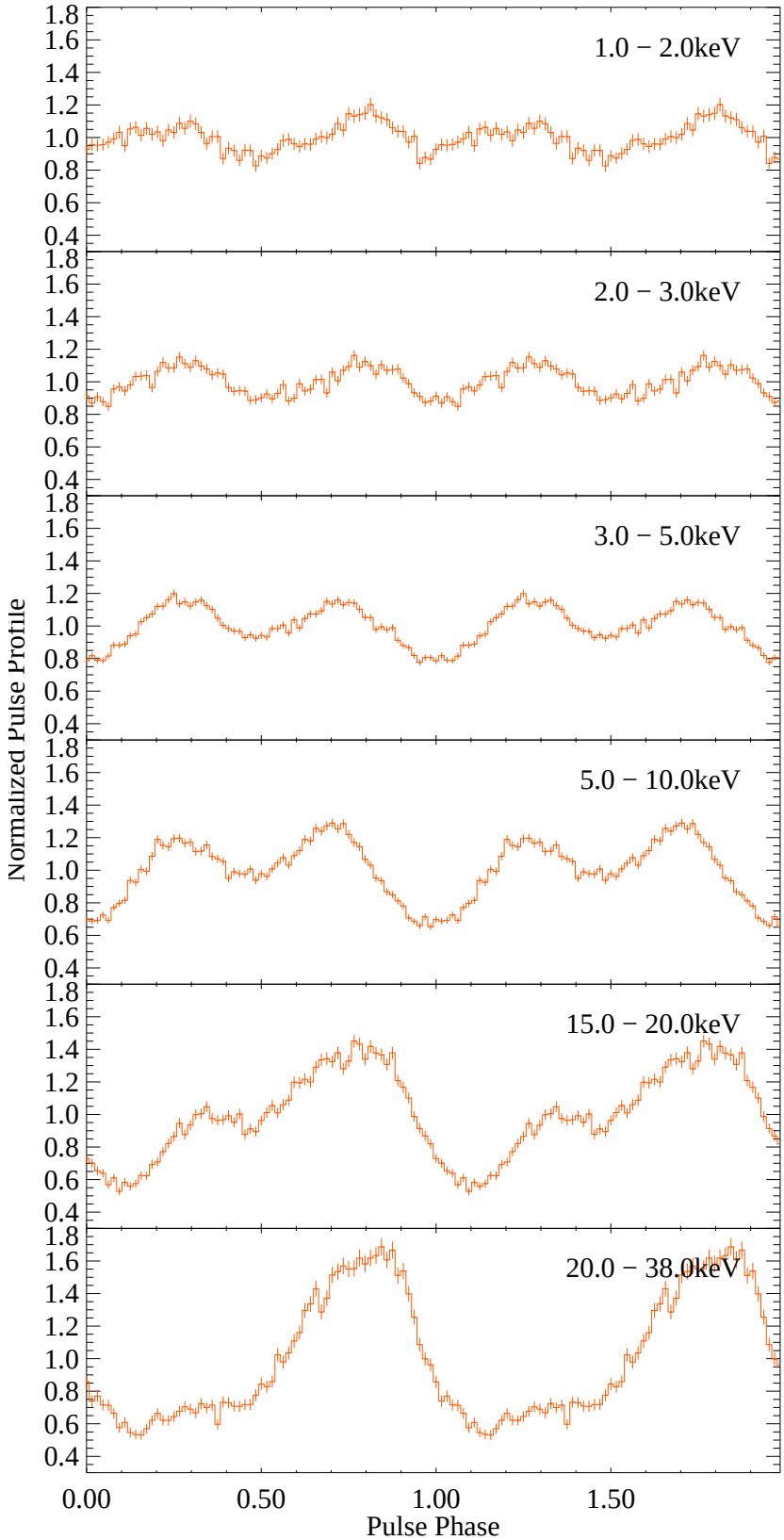

Figure 6.8: The energy resolved pulse profile of the 2007 observation normalized to the mean countrate.

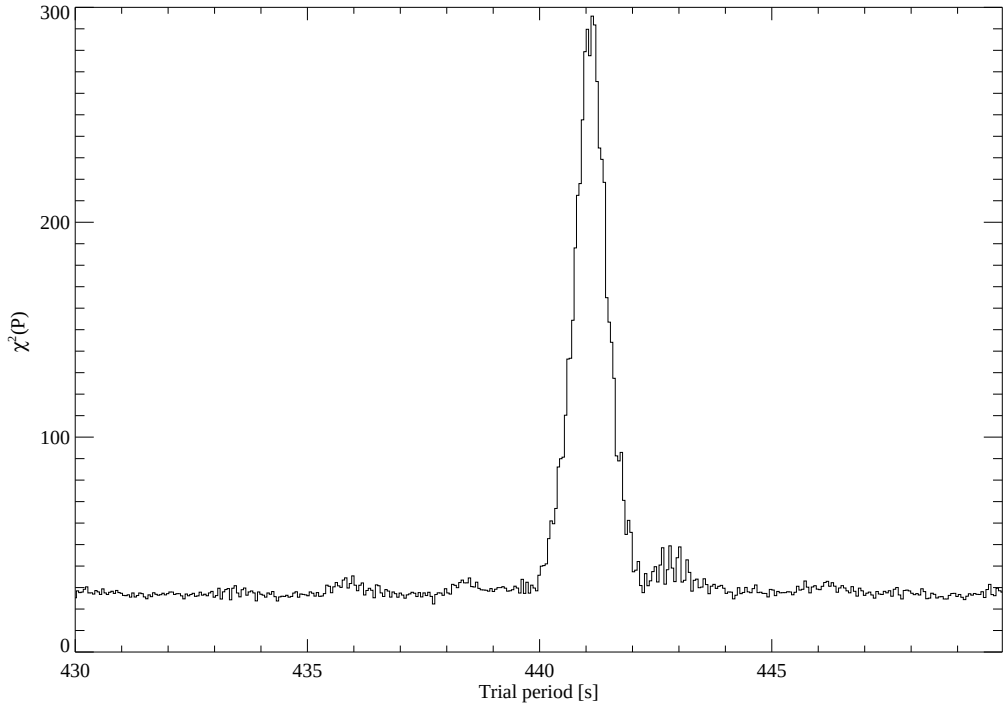

Figure 6.9: Result of epoch folding of the 2007 observation. For the analysis the high resolution PIN lightcurves were used after barycenterization.

since the change in trend can not be confirmed or dismissed. To be able to do so further observations are necessary.
The neutron star 4U 1907+09 is not the only known X-ray pulsar that showed a long term spin-down. Bildsten et al. (1997) found also the sources GX1+4, 4U 1626−67 and Vela X-1 to be spinning down on long timescales. Hercules X-1 or Centaurus X-3 on the other hand exhibit virtually continuous spin up behavior. A general explanation for the spin down behavior lies in low accretion rates that bring the magnetospheric radius R_m close to the corotation radius R_c (Ghosh & Lamb, 1979). The matter to be accreted is flung away carrying part of the rotational energy extracted from the neutron star, which slows the neutron star down. This process is the so called propeller effect. For 4U 1907+09 this is an unlikely explanation, because the magnetospheric radius is small compared to the large corotation radius. Bringing those radii close together would require a B-field of the order of 10^{14}G, which is unlikely. Or the distance has to be ~ 0.5kpc which is at least 5 times lower than studies of the optical counterpart suggest (in't Zand et al., 1998). One possible explanation for the change in trend of the pulse period is an oblique rotator Perna et al. (2006). The model of these authors is based on a purely material torque and takes into account that part of the material flung away through the propeller effect does not receive enough energy to completely unbind, which means that it would fall back into the disk. This makes it possible to be not only in one state at a given mass accretion rate. This explanation could be applied to 4U 1907+09 as this source shows similarities to 4U 1626−67 and would predict a continued spin up. For a more in depth description on the suggestion that the idea of Perna et al. (2006)

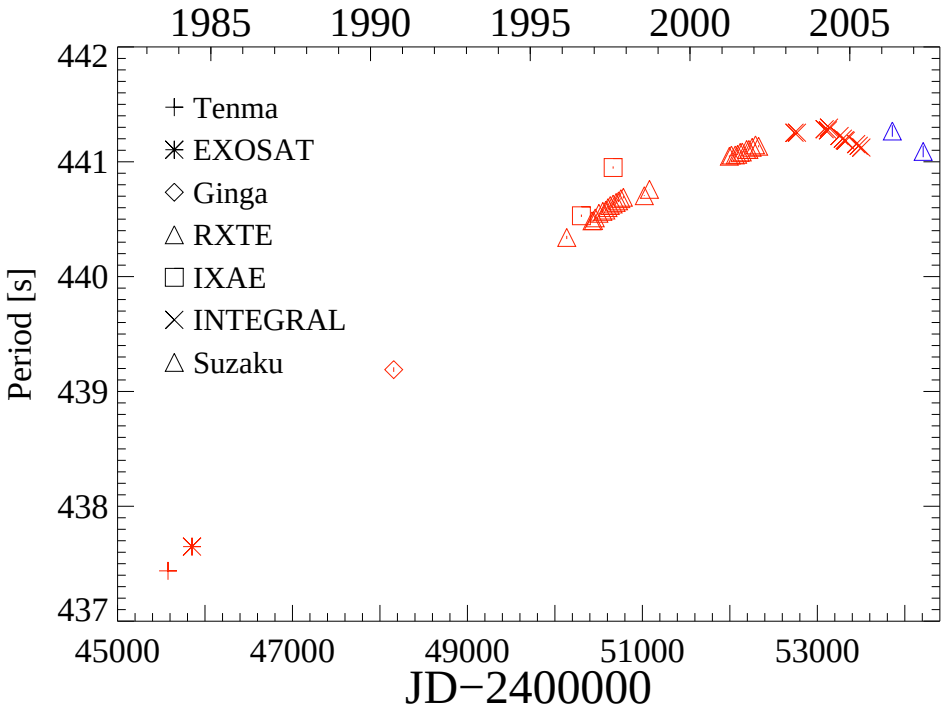

Figure 6.10: Evolution of the pulse period from 1983 to 2007. The blue triangles refer to this thesis while the other symbols show the measured pulse periods done by Makishima et al. (1984), Cook & Page (1987), Mihara (1995), in't Zand et al. (1998), Baykal et al. (2001), Baykal et al. (2006) and Fritz et al. (2006).

is applicable on 4U 1907+09 see, Fritz et al. (2006). Figure 6.11 shows the result of Perna et al. (2006) for the neutron star 4U 1626-67 when applying their model. For that source, the observation window is much smaller than the timescale for torque reversal, therefore the authors conclude that other torque inversions are not expected in the near future, unless induced by external perturbations.

As already mentioned in the last section, during flares 4U 1907+09 shows transient quasi-periodic oscillations. Quasi-periodic oscillations (QPO) are not persistent but are confined to an approximately 1000s interval centered near the peak of the flare (in't Zand et al., 1998). One possible explanation for these oscillations is the presence of a transient accretion disk during the flare. Almost all current models of QPO give the existence of an accretion disk as the site of the production. QPO have been observed from other sources with frequencies between 10–200mHz. In the two observations of 4U 1907+09 made with Suzaku, no QPO stood out.

6.5 Phase averaged results

The XIS spectra were rebinned by a factor 5 and were modeled simultaneously with the PIN spectra in the energy range from 1-40keV. The X-ray broad band continuum of 4U 1907+09 was in both observations best described by an absorbed power-law modified by an exponential cutoff at higher energies with **highecut** in **XSPEC**. We also tried

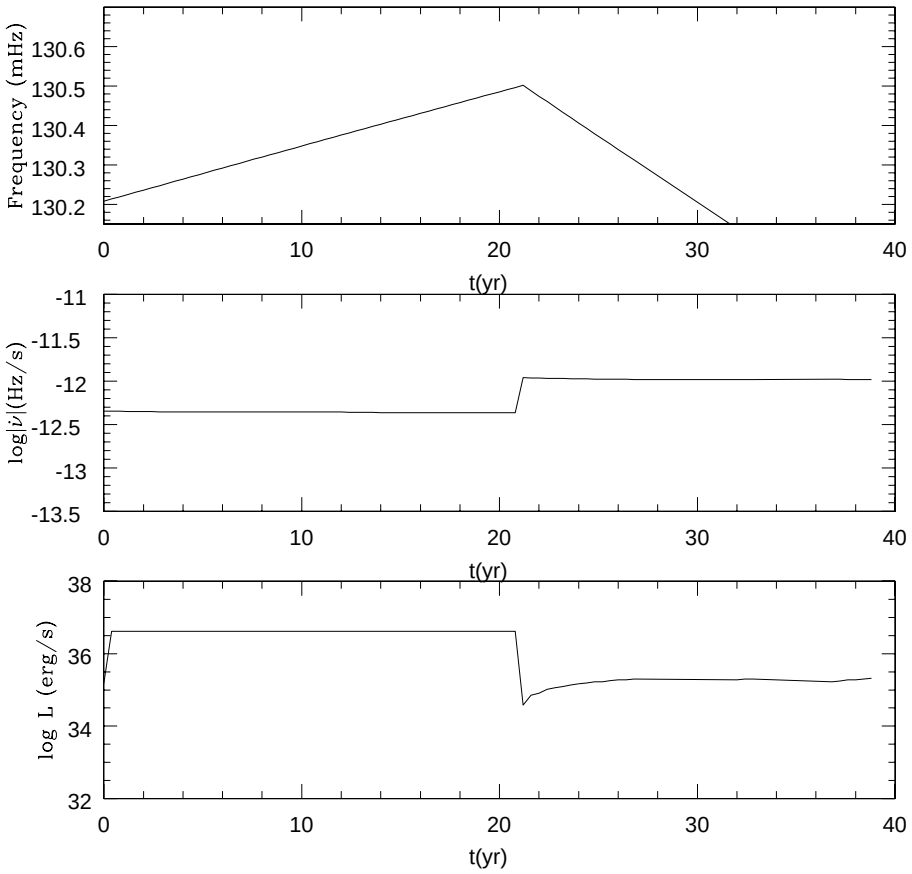

Figure 6.11: Oblique neutron star rotator with magnetic field $B = 2.5 \times 10^{12}$ G is able to reproduce the main spin-up/spin-down characteristics of 4U 1626-67. Image courtesy Perna et al. (2006)

similar continuum shapes like a power-law with a Fermi-dirac cutoff, but these were not able to improve the fits. The exact equations for the power-law modified by an exponential and by a Fermi-dirac cutoff can be found in section 4.2, equations 4.6 and 4.7. The spectra also show an uncommonly weak Fe K_α line at 6.4–6.7keV. We determined the parameters of the weak iron line from an additional Gaussian with unprecedented sensitivity, leading to a width of ~ 70 eV in the 2007 data. The line can also clearly be seen in the 2006 observation, we therefore fixed the line parameter to a width of 50eV. The fundamental cyclotron resonant scattering feature (CRSF) at $\sim$ 19keV is obvious in the residuals (top and middle residuals), it can be modeled assuming a Gaussian optical depth profile (gauabs, bottom residuals). The first harmonic of this cyclotron line at $\sim$39keV (Cusumano et al., 2000) is not includable as we were only able to model up to 40keV. The cyclotron line and its first harmonic are at comparatively low energies. A typical broad residual structure around 10keV, often observed in spectra of cyclotron line sources (e.g., Suchy et al. 2007) but which is not yet understood, is present and can be well modeled with an additional Gaussian component. With an equivalent width of 1.5keV this "10keV bump" is unusually strong in the 2007 exposure

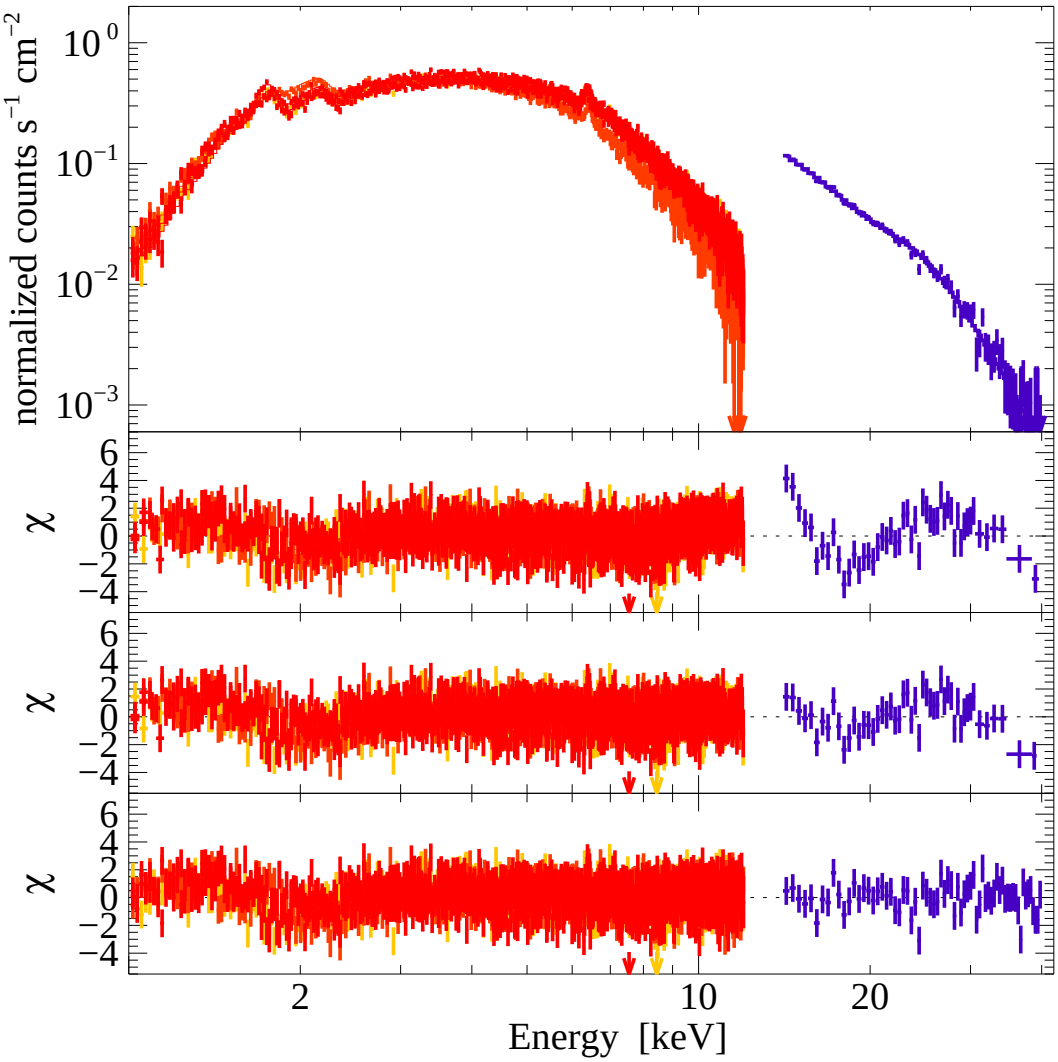

Figure 6.12: 2006: Top: XIS and PIN counts spectra and best fit model. Top residuals: Residuals without the inclusion of the gauabs component for the cyclotron line and without additional Gauss to model the 10keV feature. middle residuals: residuals without inclusion of gauabs component for the cyclotron line. Bottom residuals: Best fit residuals with all components

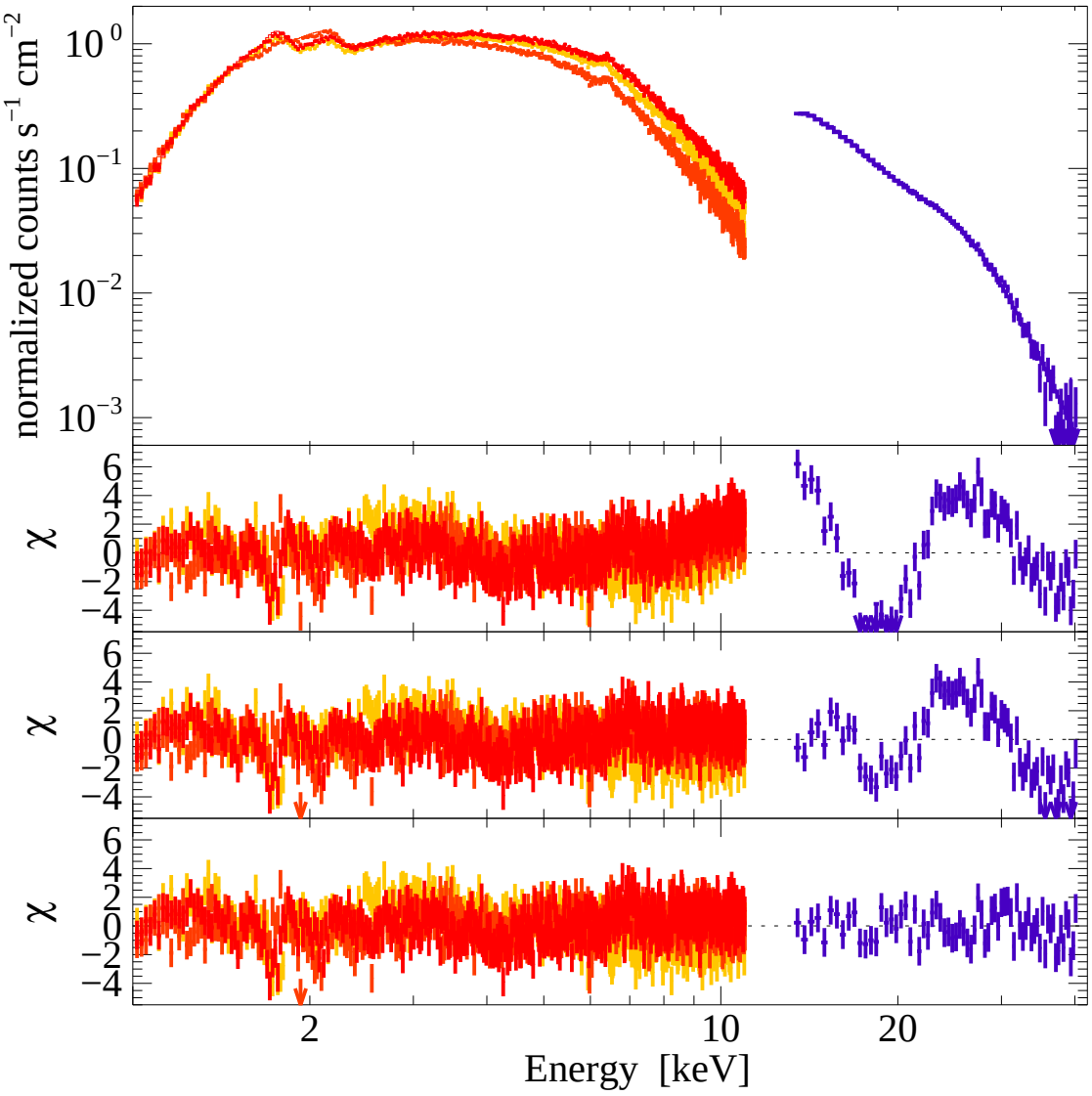

Figure 6.13: 2007: Top: XIS and PIN counts spectra and best fit model. Top residuals: Residuals without the inclusion of the gauabs component for the cyclotron line and without additional Gauss to model the 10keV feature. middle residuals: residuals without inclusion of gauabs component for the cyclotron line. Bottom residuals: Best fit residuals with all components

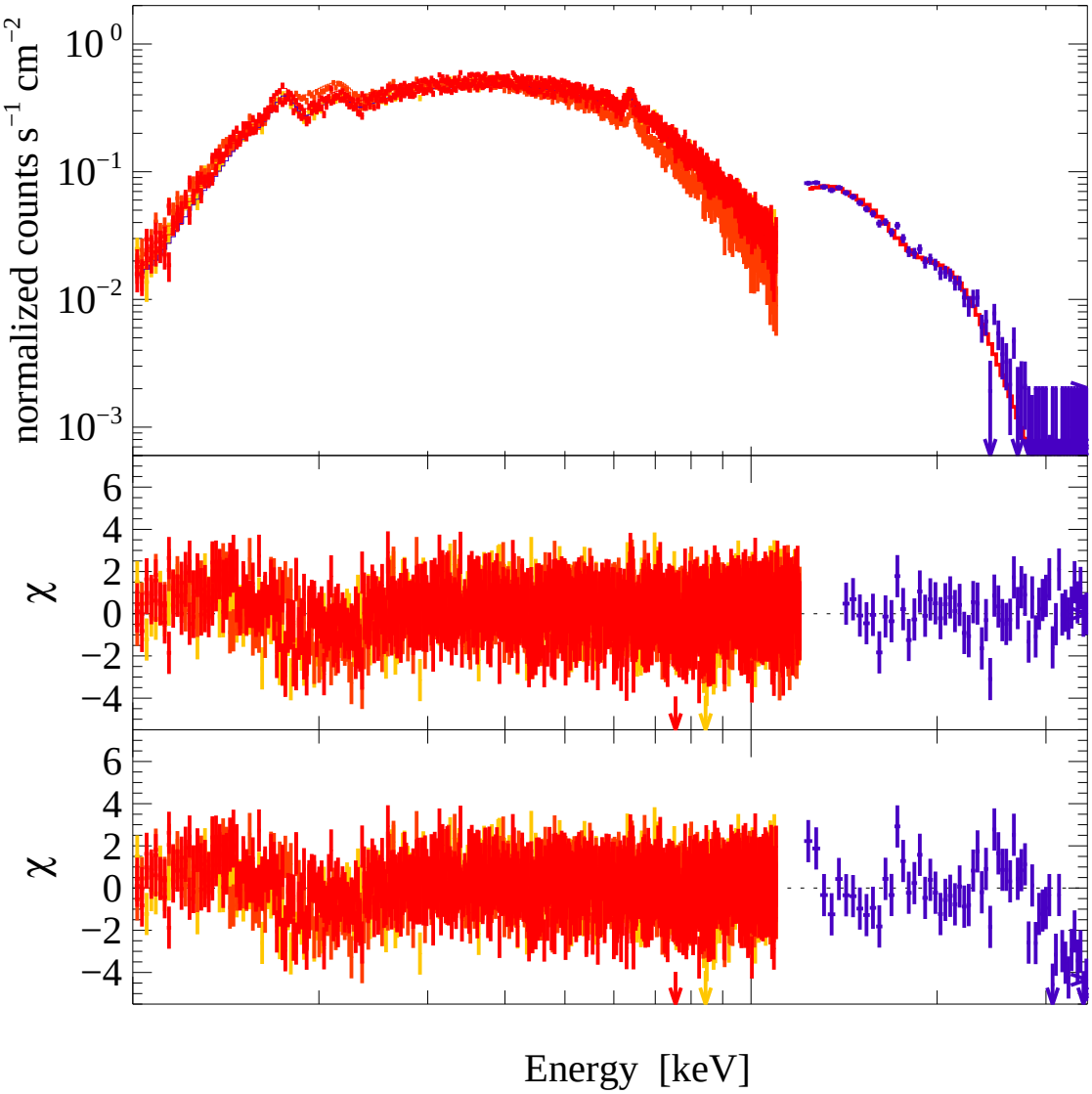

Figure 6.14: 2006: Top: XIS and PIN counts spectra and best fit model. Middle: best fit residuals when modeling the cyclotron line with the gauabs component. Bottom residuals: best fit residuals when modeled the cyclotron line with the cyclomc component.

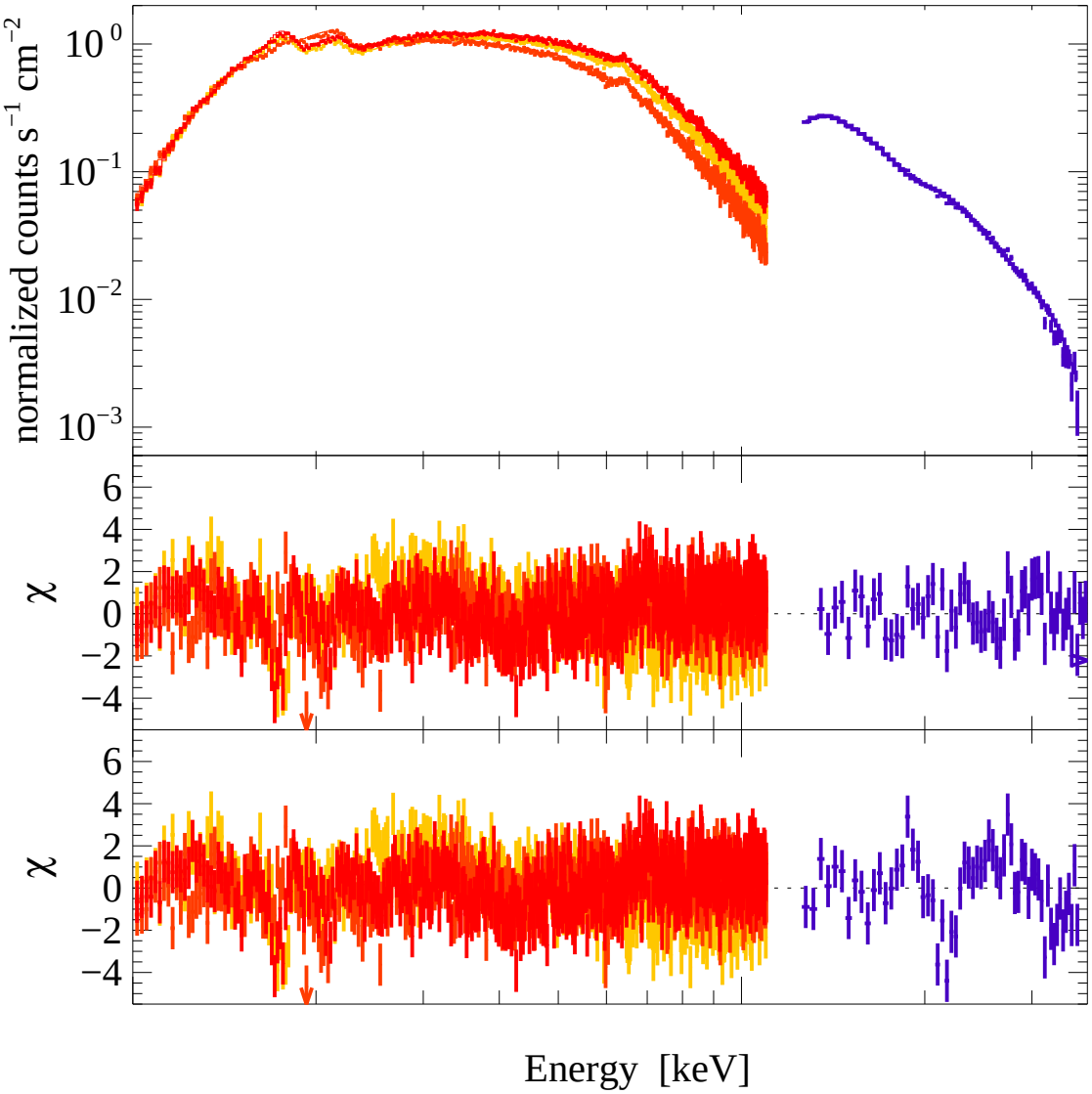

Figure 6.15: 2007: Top: XIS and PIN counts spectra and best fit model. Middle: best fit residuals when modeling the cyclotron line with the gauabs component. Bottom residuals: best fit residuals when modeled the cyclotron line with the cyclomc component.

and significantly stronger than in the 2006 observation. The model with all components and additions used for the spectra was of the form:

$$cons \times phabs \times gauabs \times highecut(power + gauss[Fe] + gauss[10keV])$$

Table 6.2: Parameter results from the best fit for the 2006 data highecut.

Parameter	without line or 10keV feature	without cyclotron line with 10keV feature	with line and 10keV feature
$N_H[10^{22}\mathrm{cm}^{-2}]$	$2.68^{+0.02}_{-0.02}$	$2.72^{+0.03}_{-0.03}$	$2.72^{+0.03}_{-0.02}$
E_{cyc} [keV]	-	-	$17.52^{+1.10}_{-0.68}$
σ_{cyc} [keV]	-	-	$3.0^{+0.0}_{-0.13}$
D_{cyc}	-	-	$0.61^{+0.24}_{-0.21}$
E_{Fold}[keV]	$11.70^{+0.27}_{-0.56}$	$13.9^{+1.36}_{-0.81}$	$8.71^{+1.49}_{-1.67}$
E_{cut}[keV]	$11.85^{+0.7}_{-0.3}$	$10.10^{+0.5}_{-0.8}$	$14.95^{+3.16}_{-3.3}$
Γ	$1.16^{+0.01}_{-0.01}$	$1.19^{+0.01}_{-0.01}$	$1.18^{+0.01}_{-0.01}$
E_{10keV}[keV]	-	$12.42^{0.44}_{-0.54}$	$11.13^{0.37}_{-0.27}$
σ_{10keV}[keV]	-	$1.47^{+0.2}_{-0.19}$	$1.04^{+0.22}_{-0.17}$
E_{Fe}[keV]	$6.40^{+0.01}_{-0.01}$	$6.40^{+0.01}_{-0.01}$	$6.40^{+0.01}_{-0.01}$
σ_{Fe}[keV]	0.05	0.05	0.05
$\chi^2/d.o.f.$	3010.41/2465	2861.78/2461	2813.8/2460
χ^2_{red}	1.22	1.16	1.14

The constant factor was set to 1 for the XIS0, but fitted for the other detectors, to take uncertainties in the relative flux normalization of the different instruments into account. The top panels of figure 6.12 and figure 6.13 show the counts spectra and their respective best fit models. The top of the three residuals do not include the gaussian component for the 10keV feature and the gauabs component for the cyclotron line. The residuals in the middle show the best fit without modeling the cyclotron line and the bottom residuals show the best fit with all components. It is obvious that all the components are needed to describe the spectra of 4U 1907+09.

The second fit was for both observations done with the same broad band continuum model and the first self-consistent model for the CRSF based on Monte Carlo simulations as described before (Schönherr et al., 2007). Preliminaty applications to the Suzaku observations show that a slab geometry is preferred over a cylinder geometry for the accretion column. As shown in figure 6.14 and 6.15 the current model predicts stronger emission wings than what is seen in the observation. The parameters of these fits are given in table 6.4.The model is only able to model the temperature of the scattering electrons down to 2.5keV and the redshift was frozen to $z = 0.3$.

Table 6.3: Parameter results from the best fit for the 2007 data highecut.

Parameter	without line or 10keV feature	without cyclotron line with 10keV feature	with line and 10keV feature
$N_H[10^{22}\mathrm{cm}^{-2}]$	$2.05^{+0.01}_{-0.02}$	$2.11^{+0.01}_{-0.01}$	$2.12^{+0.01}_{-0.01}$
E_{cyc} [keV]	-	-	$20.28^{+0.37}_{-0.45}$
σ_{cyc} [keV]	-	-	$3.0^{+0.0}_{-0.15}$
D_{cyc}	-	-	$0.71^{+0.13}_{-0.10}$
E_{Fold}[keV]	$10.99^{+0.18}_{-0.18}$	$13.68^{+0.43}_{-0.41}$	$6.21^{+0.39}_{-0.35}$
E_{cut}[keV]	$11.06^{+0.3}_{-0.2}$	$10.65^{+2.27}_{-1.04}$	$21.7^{+0.72}_{-0.53}$
Γ	$1.13^{+0.01}_{-0.01}$	$1.18^{+0.01}_{-0.01}$	$1.18^{+0.01}_{-0.01}$
E_{10keV}[keV]	-	$11.85^{+0.14}_{-0.14}$	$11.65^{0.35}_{-0.64}$
σ_{10keV}[keV]	-	$1.65^{+0.11}_{-0.18}$	$1.63^{+0.2}_{-0.32}$
E_{Fe}[keV]	$6.41^{+0.01}_{-0.01}$	$6.41^{+0.01}_{-0.01}$	$6.41^{+0.01}_{-0.01}$
σ_{Fe}[keV]	$0.05^{+0.01}_{-0.0}$	$0.072^{+0.03}_{-0.04}$	$0.074^{+0.03}_{-0.04}$
$\chi^2/d.o.f.$	3755.38/1702	2848.61/1699	2462.73/1696
χ^2_{red}	2.21	1.68	1.45

Table 6.4: Parameter results from the best fit for the data with highecut and cyclomc.

Parameter	fit with cyclomc 2006	fit with cyclomc 2007
$N_H[10^{22}\mathrm{cm}^{-2}]$	$2.73^{+0.03}_{-0.01}$	$2.11^{+0.02}_{-0.01}$
B [10^{12}G]	$2.07^{+0.07}_{-0.11}$	$2.13^{+0.03}_{-0.02}$
T_e [keV]	$3.02^{+5.14}_{-0.52}$	$2.5^{+0.25}$
Tau [10^{-4}]	$6.79^{+2.30}_{-3.91}$	$2.63^{+1.00}_{-0.33}$
mu	$0.11^{+0.08}_{-0.03}$	$0.11^{+0.04}_{-0.02}$
z	0.3 frozen	0.3 frozen
E_{cut}[keV]	$19.21^{+1.07}_{-1.14}$	$13.35^{1.54}_{+0.71}$
E_{Fold} [keV]	$2.51^{+0.38}_{-0.69}$	$12.58^{+0.83}_{-0.46}$
Γ	$1.18^{+0.01}_{-0.01}$	$1.18^{+0.01}_{-0.01}$
E_{10keV}[keV]	$10.52^{+0.25}_{-0.20}$	$10.99^{+0.50}_{-0.26}$
σ_{10keV}[keV]	$0.74^{+0.16}_{-0.11}$	$1.26^{+0.31}_{-0.16}$
E_{Fe}[keV]	$6.40^{+0.01}_{-0.01}$	$6.41^{+0.01}_{-0.01}$
σ_{Fe}[keV]	$0.00^{+0.03}$	$0.072^{+0.03}_{-0.04}$
$\chi^2/d.o.f.$	2777.71/2232	2525.18/1685
χ^2_{red}	1.24	1.50

6.6 Phase resolved results

The phase dependent pulses have an influence on the spectra as well. The observed and in section 6.5 shown spectra depend strongly on the geometry of the"accretion mound" (height of accretion column) and also on the viewing angle with respect to the high magnetic field. We expect the spectra to be changing from one part of the pulse phase to another. This does not only effect the broad band continuum but also the line parameters of the cyclotron line, which are variable over the pulse phase. For this reason we did phase resolved spectroscopy. We used six different parts of the phase as shown in figure 6.16 for the data taken in 2007. These phase bins are labeled with: off1, for the pulse minimum before the mainpeak; rmp, for the raise of the mainpeak; fmp, for the fall of the mainpeak; off2, for the pulse minimum after the mainpeak; rsp, for the raise of the secondary peak and finally fsp, for the fall of the secondary peak. We were not able to perform phase resolved spectroscopy for the observation taken in 2006. The observation time was too short and the dip, that can be seen in the lightcurve shown in figure 6.3, additionally reduced the net count rate per second.

The XIS spectra were also rebinned by a factor 5 and were modeled simultaneously with the PIN spectra in the energy range from 1–35keV. For the modeling of the continuum we used again an absorbed power-law modified by an exponential cutoff at higher energies. The cyclotron line and the 10keV feature were also included as described above for the phase averaged spectra. For the variable σ_{cyc} we had to set an upper limit to 3keV. In all six phase bins the column density N_H of the stellar wind is

Table 6.5: Parameter results from the best fit for the 2007 data, modeled with a powerlaw and an exponential cutoff at higher energies

Parameter	raise secpeak 0.65-0.85	fallsecpeak 0.85-1	off1 0-0.15
$N_H[10^{22}\mathrm{cm}^{-2}]$	$1.99^{+0.03}_{-0.03}$	$2.29^{+0.03}_{-0.03}$	$2.19^{+0.04}_{-0.03}$
E_{cyc} [keV]	$21.07^{+0.93}_{-1.20}$	$18.70^{+0.66}_{-0.70}$	$19.90^{+0.33}_{-0.82}$
σ_{cyc} [keV]	$3.0^{+0.0}_{-1.4}$	$3.00_{-0.57}$	$2.99^{+0.01}_{-0.46}$
D_{cyc}	$0.28^{+0.12}_{-0.06}$	$1.11^{+0.12}_{-0.23}$	$1.65^{+0.08}_{-0.20}$
$E_{\mathrm{F}old}$[keV]	$8.90^{+2.37}_{-1.24}$	$5.01^{+1.50}_{-0.83}$	$3.41^{+0.83}_{-0.49}$
E_{cut}[keV]	$23.42^{+0.98}_{-2.03}$	$19.31^{+1.45}_{-2.36}$	$20.86^{+0.64}_{-2.05}$
Γ	$1.06^{+0.02}_{-0.02}$	$1.50^{+0.02}_{-0.02}$	$1.40^{+0.02}_{-0.02}$
E_{10keV}	$11.53^{+0.01}_{-0.86}$	$10.04^{+0.12}_{-0.41}$	$9.85^{+0.26}_{-0.58}$
σ_{10keV}	$1.73^{+0.27}_{-0.49}$	$0.23^{+0.10}_{-0.08}$	$0.36^{+0.95}_{-0.26}$
E_{Fe}	$6.42^{+0.05}_{-0.04}$	$6.42^{+0.02}_{-0.02}$	$6.39^{+0.03}_{-0.04}$
σ_{Fe}	$0.16^{+0.08}_{-0.07}$	$0.0^{+0.06}$	$0.05^{+0.05}_{-0.05}$
$\chi^2/d.o.f.$	1921.46/1687	2157.87/1687	1884.68/1687
χ^2_{red}	1.14	1.28	1.12

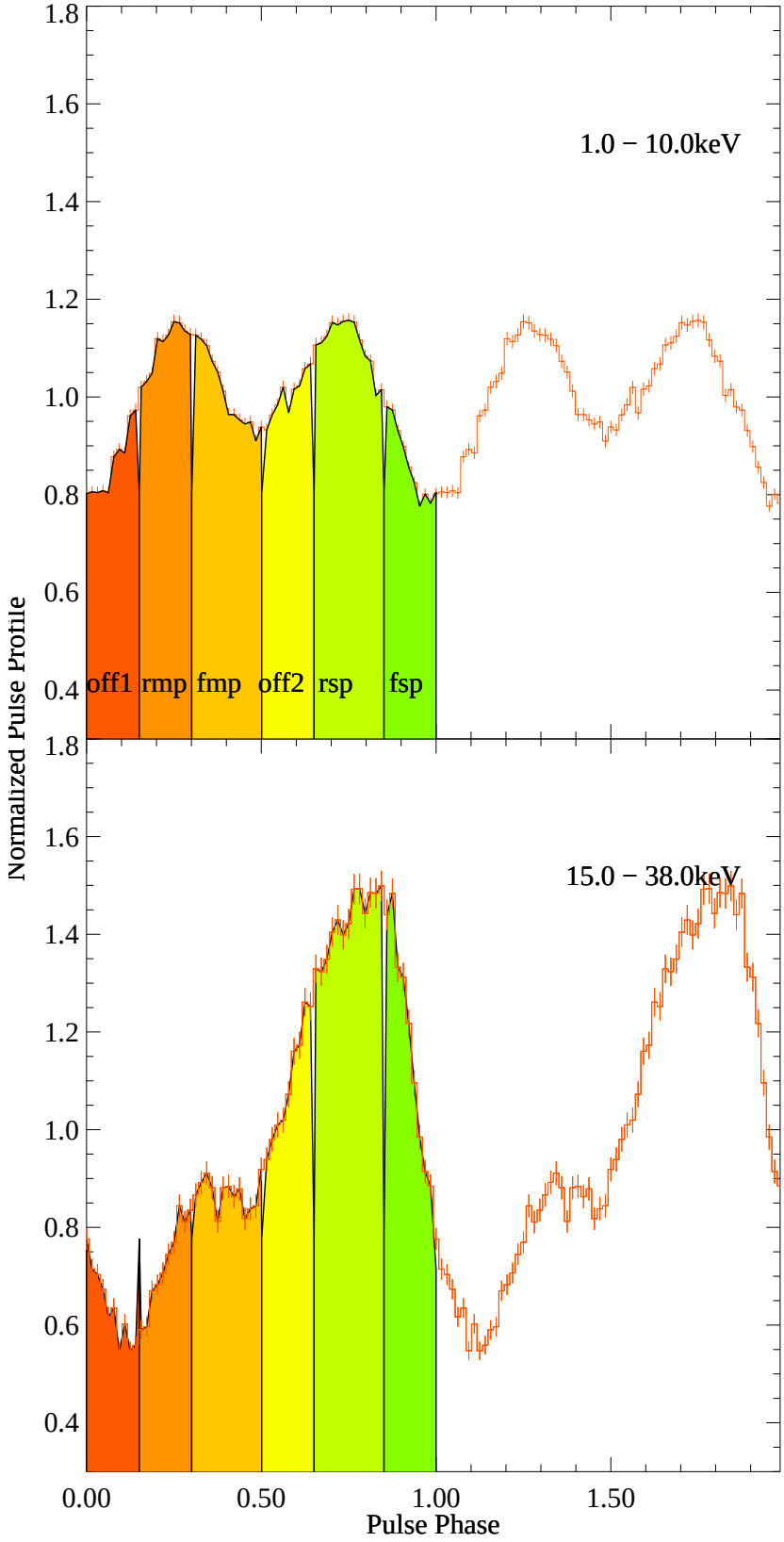

Figure 6.16: Pulsephase indicating phases for phase resolved spectroscopy. Six phase bins were used and are shown in different colors. The rise and fall of the main pulse

Table 6.6: Parameter results from the best fit for the 2007 data, modeled with a powerlaw and an exponential cutoff at higher energies

Parameter	raise mainpeak 0.15-0.3	fall mainpeak 0.3-0.5	off2 0.5-0.65
$N_H[10^{22}\mathrm{cm}^{-2}]$	$2.17^{+0.03}_{-0.03}$	$2.20^{+0.03}_{-0.03}$	$2.07^{+0.03}_{-0.03}$
E_{cyc} [keV]	$21.90^{+1.10}_{-0.92}$	$20.46^{+1.50}_{-1.24}$	$18.96^{+1.29}_{-0.33}$
σ_{cyc} [keV]	$3.00_{-0.93}$	$3.00_{-0.57}$	$2.4^{+0.60}_{-0.84}$
D_{cyc}	$1.02^{+0.24}_{-0.24}$	$0.46^{+0.13}_{-0.16}$	$0.47^{+0.15}_{-0.12}$
$E_{\mathrm{F}old}$[keV]	$2.74^{+0.74}_{-0.74}$	$6.03^{+1.03}_{-0.85}$	$10.38^{+2.11}_{-2.13}$
E_{cut}[keV]	$24.26^{+1.61}_{-1.63}$	$22.49^{+1.58}_{-1.29}$	$19.68^{+1.25}_{-3.36}$
Γ	$1.14^{+0.02}_{-0.02}$	$1.15^{+0.02}_{-0.02}$	$1.03^{+0.02}_{-0.02}$
E_{10keV}	$12.83^{+0.17}_{-0.38}$	$12.71^{+0.29}_{-0.25}$	$12.68^{+0.31}_{-2.68}$
σ_{10keV}	$1.40^{0.31}_{-0.20}$	$1.77^{+0.23}_{-0.24}$	$1.99^{+0.31}_{-0.71}$
E_{Fe}	$6.38^{+0.04}_{-0.04}$	$6.40^{+0.03}_{-0.03}$	$6.44^{+0.04}_{-0.03}$
σ_{Fe}	$0.03^{+0.08}_{-0.03}$	$0.04^{+0.06}_{-0.04}$	$0.09^{+0.05}_{-0.07}$
$\chi^2/d.o.f.$	1858.54/1687	1813.43/1687	1880.72/1689
χ^2_{red}	1.10	1.07	1.11

almost constant with only small variability. The parameters of the exponential cutoff vary strongly. The folding energy E_{fold} is smallest at the raise of the mainpeak with $2.74^{+0.74}_{-0.74}$ and is highest at the off2 bin with $10.38^{+2.11}_{-2.13}$. The cutoff energy E_{cut} also varies between $19.31^{+1.45}_{2.36}$ keV and $24.26^{+1.61}_{-1.63}$. Figure 6.19 shows these variations over the pulse phase, as can be seen that while the cutoff energy seems to be correlated to the pulse phase, the folding energy is not. Figure 6.17 shows the variation of the cyclotron line energy over the pulse phase. As expected the cyclotron line energy varies with the six chosen phase bins from a low of 18.7keV to 21.9keV and seems to be correlated to the pulse phase. The energy is highest at the peak but gets smaller in the phase bins next to that. The depth varies as well, but this variation is not sinusoidal. And there is no correlation that the energy becomes deeper when the energy becomes higher. The depth is greatest in the off1 bin and gets smaller for the next for bins, and then becomes higher again at the fall of the secondary peak. The iron line is rather constant over the pulse phase with small variations of 0.06 keV. The energy of the 10keV feature displays also variability but does not correlate with the energy of the cyclotron line. The feature is strongest when the energy is highest and vice versa.

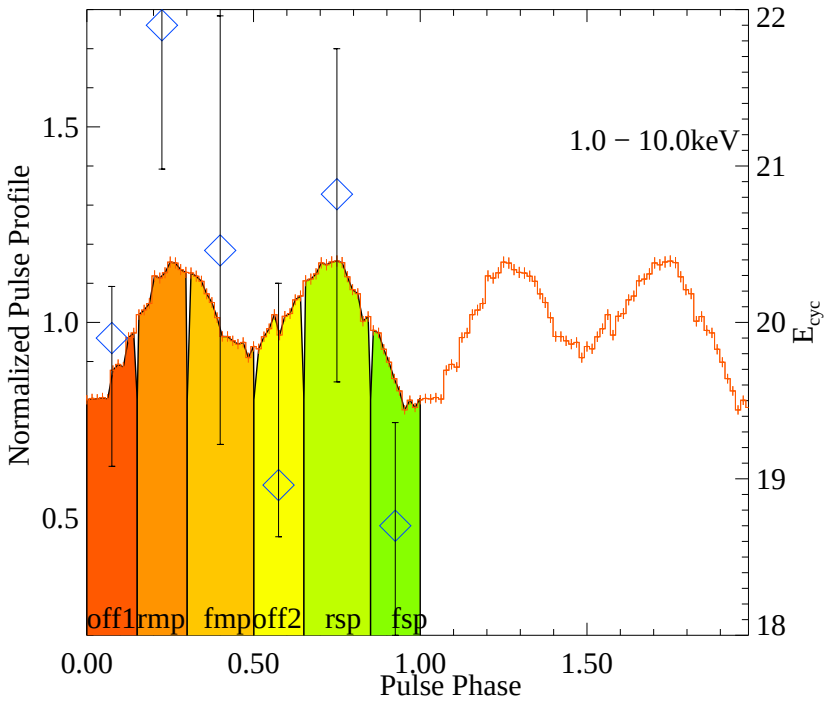

Figure 6.17: Variation of the cyclotron line energy over the pulse phase

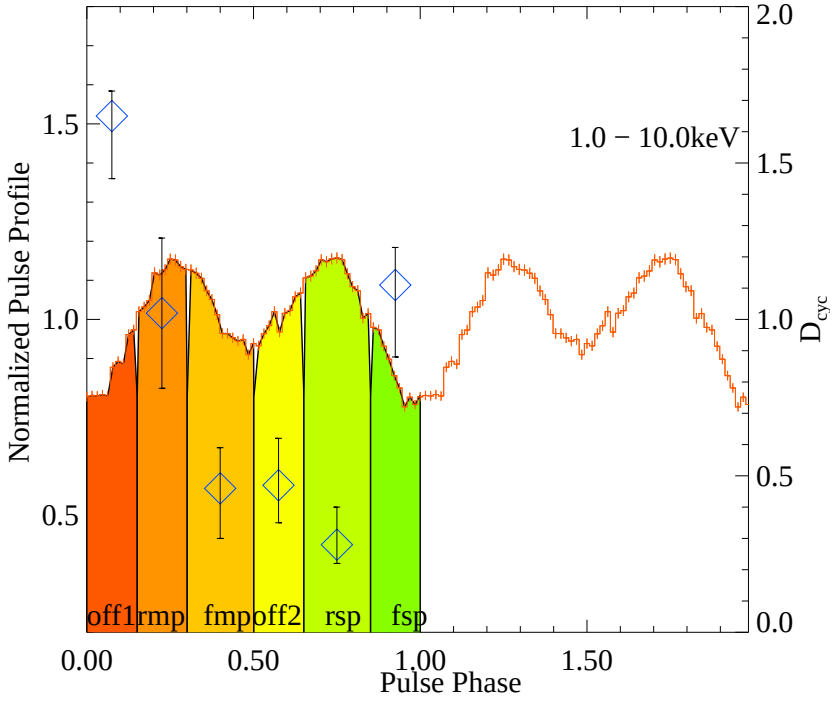

Figure 6.18: Variation of the cyclotron line depth over the pulse phase

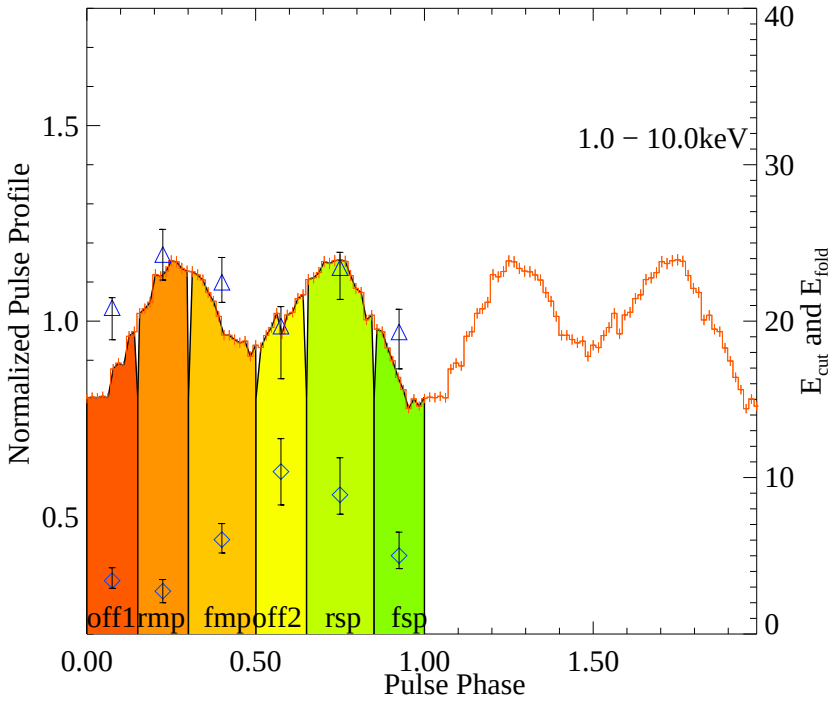

Figure 6.19: Variation of the folding energy and the cutoff energy over the pulse phase. The triangles correspond to the cutoff energy in keV and the diamond to the folding energy.

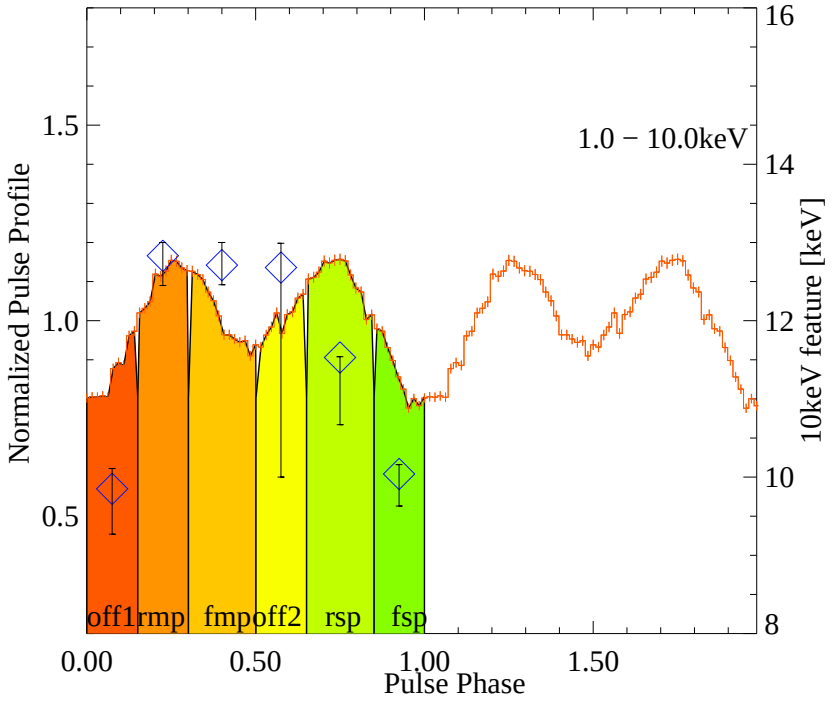

Figure 6.20: Variation of the 10keV feature energy over the pulse phase

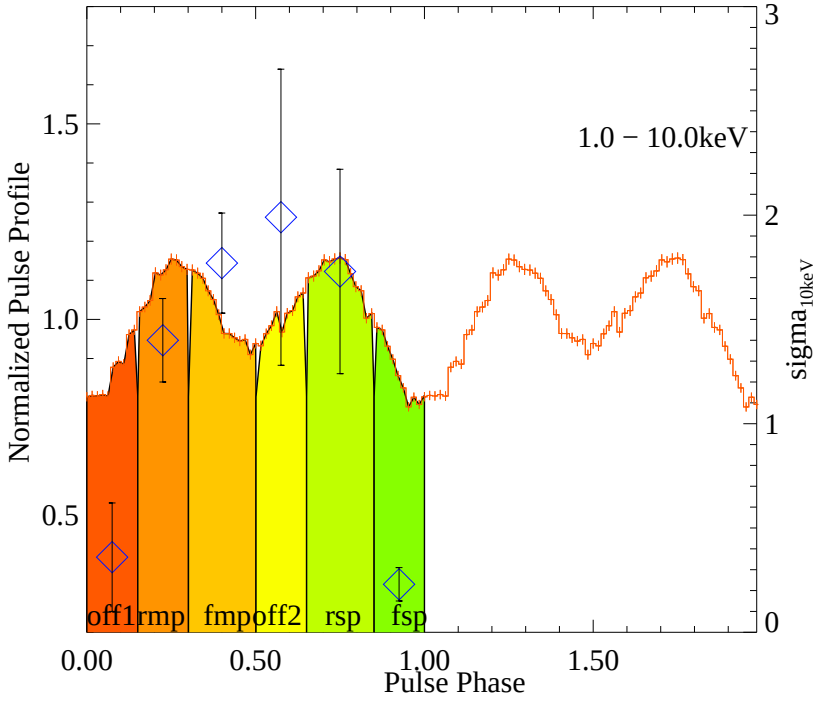

Figure 6.21: Variation of the 10keV feature sigma over the pulse phase

Chapter 7

Conclusion

Two observations of the source 4U 1907+09, taken with the satellite Suzaku, were analyzed. The first chapters give an introduction to the theory necessary to be able to describe the lightcurves, pulse periods and spectra. These chapters include an overview over the evolution of compact objects and X-ray binaries. In chapter 3 the different possibilities for accretion onto a compact object, Roche lobe overflow, Be-mechanism and wind accretion were explained. The following section concentrated on the accretion column and accretion geometry. The accretion column is the source of the spectrum and the cyclotron line and both are dependent of the high magnetic field of the neutron star. This part of the work also explained where these magnetic fields come from and how they evolve. Chapter 5 then describes the satellite Suzaku, its instruments and technical aspects. In the last part of the work the results from the analysis are given. First we summarized the results that other authors gained from different observations of 4U 1907+09 like period evolution and flaring and dipping behavior. After that a thorough description of the data analysis and reduction was given. Suzaku observed the source twice, the first time for $\approx$ 44,0 ksec on 2006 May 2–3 and the second time for $\approx$69,5 ksec on 2007 April 19–21. The lightcurves from the two different years couldn't be more different. The data from 2006 shows, the for the neutron star 4U 1907+09 typical dipping behavior while the data from 2007 shows equally typical flaring behavior with durations of 1–2 hours. Additionally the source was in 2007 brighter by a factor of 2 and both lightcurves show a clearly pulsed signal. For about 20 years 4U 1907+09 was found to be spinning down, from being 437.5 s in 1983 to 440.76 s in 1997 with an average of $\dot{P}_{\mathrm{Pulse}} = +0.225\,\mathrm{s\,yr^{-1}}$. Fritz et al. (2006) reported then a torque reversal and found the source to be spinning up. We derived, using the PIN with its good time resolution, updated pulse periods but were not able to confirm or dismiss a continued spin up. Further observations will be necessary to be able to see how the pulse period evolves from this point. The spectra of both observations were best described by an absorbed power-law modified by an exponential cutoff at higher energies. The cyclotron line at $\sim$ 19 keV is clearly visible and the often observed "10keV feature" was found to be compared to other sources uncommonly strong in the 2007 data and only a little weaker in 2006. 4U 1907+09 also shows a very weak iron line at 6.4 keV which was detected with unprecendet sensitivity. Phase resolved spectroscopy was only possible for the longer observation in 2007, where six phase bins were chosen. The phase resolved results revealed variability of almost all parameters over the pulse phase except for the

column density and the iron line. Not only the line parameters showed variations but also the components of the continuum, especially the folding energy, whose minimum was at 2.74 at the raise of the mainpeak and 10.38 at the off2 phase bin. The energy of the "10keV feature" was found not to be correlated with the energy of the cyclotron line. This feature remains a mystery as there is no explanation for it yet.

Bibliography

Abt H.A., 1983, ARA&A 21, 343

Anzer U., Börner G., 1980, A&A 83, 133

Araya R.A., Harding A.K., 1996, A&AS 120, C183+

Arnaud K.A., 1996, In: Jacoby G.H., Barnes J. (eds.) Astronomical Data Analysis Software and Systems V, Vol. 101. Astronomical Society of the Pacific Conference Series, p.17

Basko M.M., Sunyaev R.A., 1976, MNRAS 175, 395

Baykal A., Inam Ç., Ali Alpar M., et al., 2001, MNRAS 327, 1269

Baykal A., İnam S.Ç., Beklen E., 2006, MNRAS 369, 1760

Becker P.A., 1998, ApJ 498, 790

Becker P.A., Wolff M.T., 2005, ApJ 630, 465

Becker P.A., Wolff M.T., 2007, ApJ 654, 435

Bickenkov E.I., 2006, Journal of Applied Mechanics and Technical Physics 792–805

Bildsten L., Chakrabarty D., Chiu J., et al., 1997, ApJS 113, 367

Boldt E., 1987, In: Hewitt A., Burbidge G., Fang L.Z. (eds.) Observational Cosmology, Vol. 124. IAU Symposium, p.611

Bondi H., Hoyle F., 1944, MNRAS 104, 273

Burbidge E.M., Burbidge G.R., Fowler W.A., Hoyle F., 1957, Rev. Mod. Phys. 29, 547

Chandrasekhar S., 1931, ApJ 74, 81

Coburn W., Heindl W.A., Rothschild R.E., et al., 2002, ApJ 580, 394

Conti P.S., 1978, ARA&A 16, 371

Cook M.C., Page C.G., 1987, MNRAS 225, 381

Cottam J., Boyce K.R., Brown G.V., et al., 2005, In: Smith R. (ed.) X-ray Diagnostics of Astrophysical Plasmas: Theory, Experiment, and Observation, Vol. 774. American Institute of Physics Conference Series, p.379

Cox N.L.J., Kaper L., Foing B.H., Ehrenfreund P., 2005a, A&A 438, 187

Cox N.L.J., Kaper L., Mokiem M.R., 2005b, A&A 436, 661

Cusumano G., di Salvo T., Burderi L., et al., 1998, A&A 338, L79

Cusumano G., di Salvo T., Burderi L., et al., 2000, Advances in Space Research 25, 409

Davidson K., Ostriker J.P., 1973, ApJ 179, 585

Frank J., King A., Raine D., 1992, Accretion Power in Astrophysics, 2nd edn., Cambridge University Press, Cambridge, New York, Melbourne

Fritz S., Kreykenbohm I., Wilms J., et al., 2006, A&A 458, 885

Galloway D., 2008, In: American Institute of Physics Conference Series, Vol. 983. American Institute of Physics Conference Series, p.510

Ghosh P., Lamb F.K., 1978, Astrophys. J., Lett. 223, L83

Ghosh P., Lamb F.K., 1979, ApJ 232, 259

Giacconi R., Kellogg E., Gorenstein P., et al., 1971, ApJ 165, L27

Grimm H.J., Gilfanov M., Sunyaev R., 2003, Chinese Journal of Astronomy and Astrophysics Supplement 3, 257

Harding A.K., 1994, In: Holt S., Day C.S. (eds.) The Evolution of X-ray Binariese, Vol. 308. American Institute of Physics Conference Series, p.429

Harding A.K., Daugherty J.K., 1991, ApJ 374, 687

Harding A.K., Lai D., 2006, Reports of Progress in Physics 69, 2631

Heger A., Fryer C.L., Woosley S.E., et al., 2003, ApJ 591, 288

Heindl W.A., Rothschild R.E., Coburn W., et al., 2004, In: Kaaret P., Lamb F.K., Swank J.H. (eds.) X-ray Timing 2003: Rossi and Beyond, Vol. 714. American Institute of Physics Conference Series, p.323

Herold H., Ruder H., 1979, Mitteilungen der Astronomischen Gesellschaft Hamburg 45, 25

Iben I.J., 1991, ApJS 76, 55

in 't Zand J.J.M., Strohmayer T.E., Baykal A., 1997, Astrophys. J., Lett. 479, L47+

Inoue H., 2003, Advances in Space Research 32, 2089

in't Zand J.J.M., Baykal A., Strohmayer T.E., 1998, ApJ 496, 386

Ishisaki Y., Maeda Y., Fujimoto R., et al., 2007, PASJ 59, 113

Karttunen H., 1987, Fundamental astronomy, Springer, Berlin

Kawaharada M., Hong S., Murashima M.M., et al., 2004, In: Holland A.D. (ed.) High-Energy Detectors in Astronomy. Edited by Holland, Andrew D. Proceedings of the SPIE, Volume 5501, pp. 286-295 (2004)., Vol. 5501. Presented at the Society of Photo-Optical Instrumentation Engineers (SPIE) Conference, p.286

Koyama K., Tsunemi H., Dotani T., et al., 2007, PASJ 59, 23

Lai D., 2001, Reviews of Modern Physics 73, 629

Latal H.G., 1986, ApJ 309, 372

Leahy D.A., Darbro W., Elsner R.F., et al., 1983, ApJ 266, 160

Liu Q.Z., van Paradijs J., van den Heuvel E.P.J., 2005, A&A 442, 1135

Makishima K., Kawai N., Koyama K., et al., 1984, PASJ 36, 679

Makishima K., Mihara T., 1992, In: Tanaka Y., Koyama K. (eds.) Frontiers Science Series., p.23

Marshall N., Ricketts M.J., 1980, MNRAS 193, 7P

Marshall N., Watson M.G., Oda M., 1980a, IAU Circ. 3452, 1

Marshall N., Watson M.G., Oda M., 1980b, IAU Circ. 3452, 1

Mihara T., 1995, Ph.D. thesis, , Dept. of Physics, Univ. of Tokyo (M95), (1995)

Mihara T., Makishima K., Nagase F., 1995, In: Bulletin of the American Astronomical Society, Vol. 27. Bulletin of the American Astronomical Society, p.1434

Mitsuda K., Bautz M., Inoue H., et al., 2007, PASJ 59, 1

Mori H., Iizuka R., Shibata R., et al., 2005, PASJ 57, 245

Mukerjee K., Agrawal P.C., Paul B., et al., 2001, ApJ 548, 368

Nagase F., Corbet R.H.D., Day C.S.R., et al., 1992, ApJ 396, 147

Nakajima H., Yamaguchi H., Matsumoto H., et al., 2004, In: Hasinger G., Turner M.J.L. (eds.) UV and Gamma-Ray Space Telescope Systems. Edited by Hasinger, Günther; Turner, Martin J. L. Proceedings of the SPIE, Volume 5488, pp. 124-135 (2004)., Vol. 5488. Presented at the Society of Photo-Optical Instrumentation Engineers (SPIE) Conference, p.124

Oppenheimer J.R., Volkoff G.M., 1939, Phys. Rev. 55, 374

Orlandini M., Fiume D.D., 2001, X-ray Astronomy: Stellar Endpoints, AGN, and the Diffuse X-ray Background 599, 283

Perna R., Bozzo E., Stella L., 2006, ApJ 639, 363

Pinkau K., 1975, Sterne und Weltraum 14, 4

Reisenegger A., 2007, Astronomische Nachrichten 328, 1173

Sadeh D., Livio M., 1982, ApJ 258, 770

Salpeter E.E., 1964, ApJ 140, 796

Savonije G.J., 1978, A&A 62, 317

Schönherr G., Wilms J., Kretschmar P., et al., 2007, A&A 472, 353

Schreier E., Tananbaum H., Kellogg E., et al., 1972, In: Bulletin of the Amer-

ican Astronomical Society, Vol. 4. Bulletin of the American Astronomical Society, p.261

Schwartz D.A., Griffiths R.E., Bowyer S., et al., 1980, AJ 85, 549

Serlemitsos P.J., Soong Y., Chan K.W., et al., 2007, PASJ 59, 9

Spruit H.C., 2007, ArXiv e-prints 711

Suchy S., Pottschmidt K., Wilms J., et al., 2007, ArXiv e-prints 711

Tananbaum H., Gursky H., Kellogg E.M., et al., 1972, Astrophys. J., Lett. 174, L143+

Terada Y., Enoto T., Miyawaki R., et al., 2007, ArXiv e-prints 711

Trümper J., Pietsch W., Reppin C., et al., 1978, Astrophys. J., Lett. 219, L105

Unsöld A., Baschek B., 2005, Der neue Kosmos, Springer, Berlin

van Kerkwijk M.H., van Oijen J.G.J., van den Heuvel E.P.J., 1989, A&A 209, 173

Weisskopf M.C., Brinkman B., Canizares C., et al., 2002, PASP 114, 1

White N.E., Swank J.H., Holt S.S., 1983, ApJ 270, 711

Yakovlev D.G., Kaminker A.D., Gnedin O.Y., Haensel P., 2001, Phys. Rep. 354, 1

Yamaguchi H., Nakajima H., Koyama K., et al., 2006, In: Wilson A. (ed.) The X-ray Universe 2005, Vol. 604. ESA Special Publication, p.949

Zel'dovich Y.B., 1964, Soviet Physics Doklady 9, 195

APPENDIX

This appendix contains the XIS and PIN count spectra and best fit models for both observations rebinned in Xspec with the command: setplot rebin 40 40, in order to see possible systematics. This only effects the presentation of the data in the plots and means that the plot is rebinned with a minimum significance of 40, but no more than 40 bins are combined.

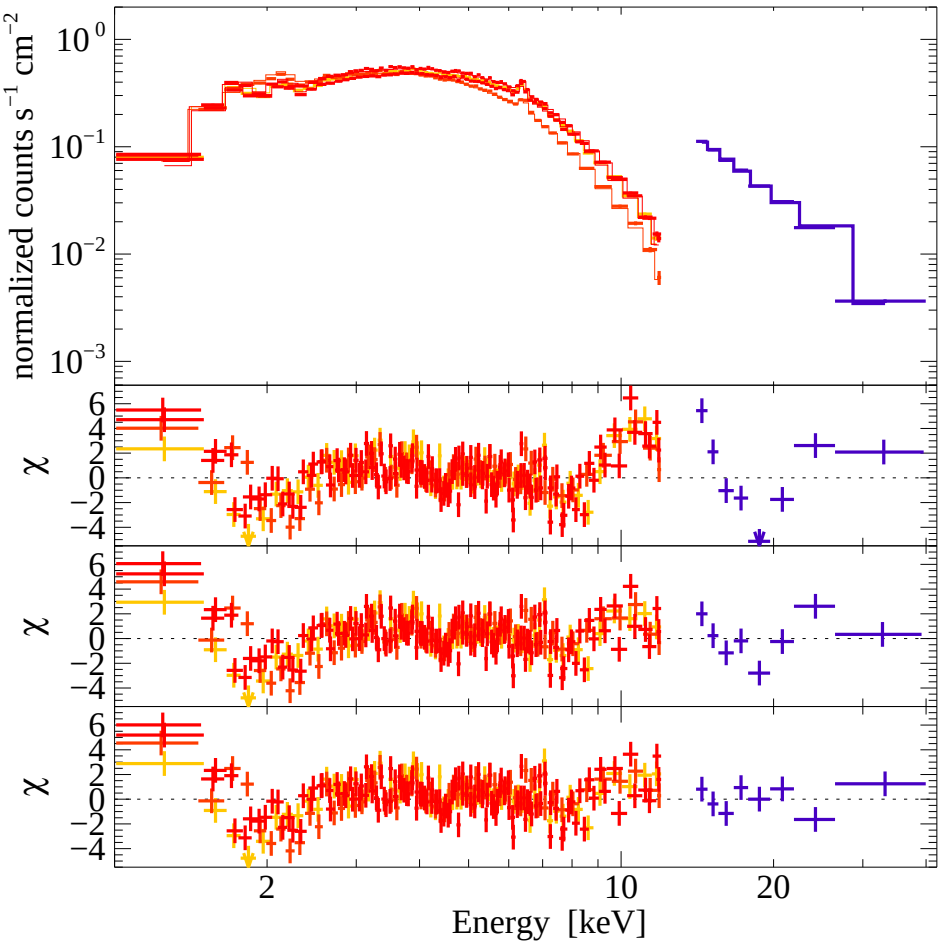

Figure 7.1: 2006: Top: XIS and PIN counts spectra and best fit model, rebinned. Top residuals: Residuals without the inclusion of the gauabs component for the cyclotron line and without additional Gauss to model the 10keV feature. middle residuals: residuals without inclusion of gauabs component for the cyclotron line. Bottom residuals: Best fit residuals with all components

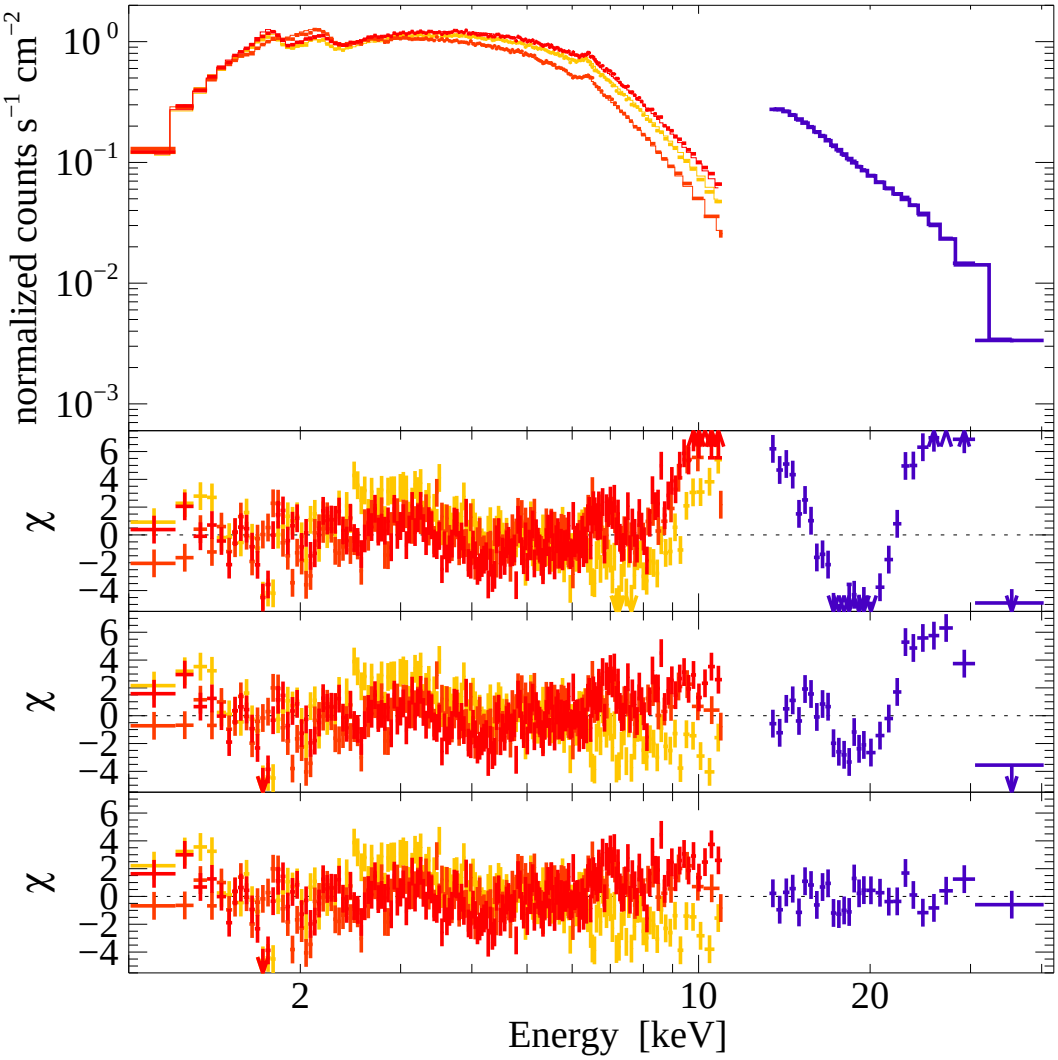

Figure 7.2: 2007: Top: XIS and PIN counts spectra and best fit model, rebinned. Top residuals: Residuals without the inclusion of the gauabs component for the cyclotron line and without additional Gauss to model the 10keV feature. middle residuals: residuals without inclusion of gauabs component for the cyclotron line. Bottom residuals: Best fit residuals with all components

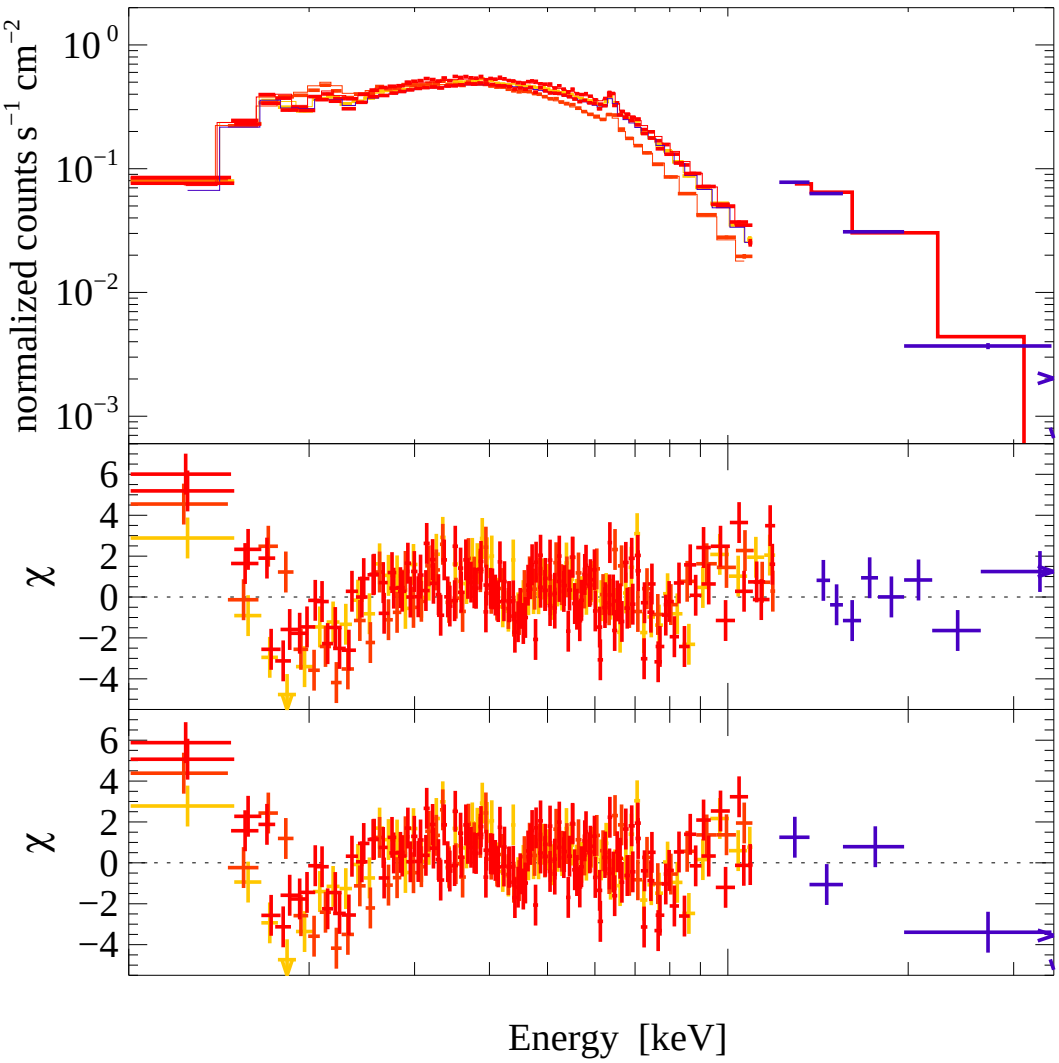

Figure 7.3: 2006: Top: XIS and PIN counts spectra and best fit model, rebinned. Middle: best fit residuals when modeling the cyclotron line with the gauabs component. Bottom residuals: best fit residuals when modeled the cyclotron line with the cyclomc component.

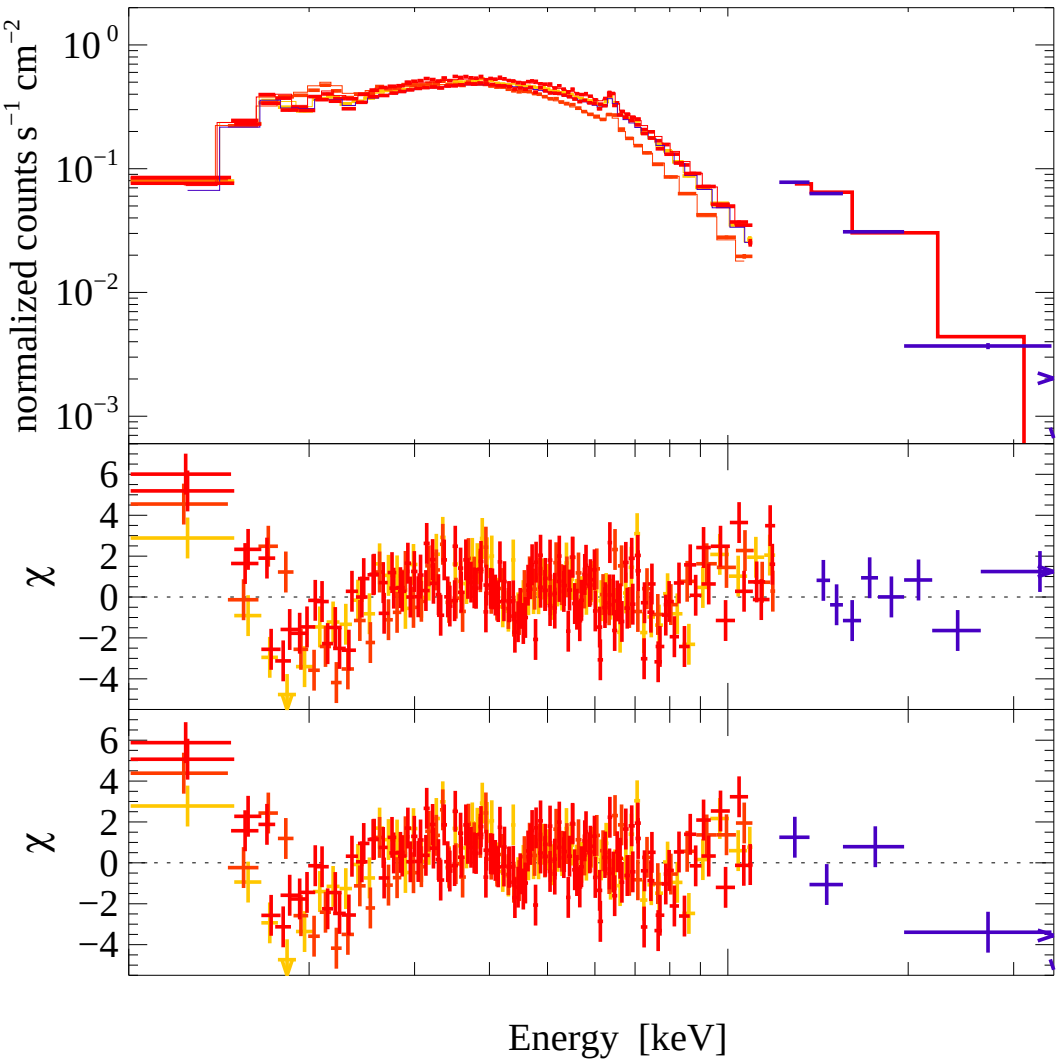

Figure 7.4: 2007: Top: XIS and PIN counts spectra and best fit model, rebinned. Middle: best fit residuals when modeling the cyclotron line with the gauabs component. Bottom residuals: best fit residuals when modeled the cyclotron line with the cyclomc component.